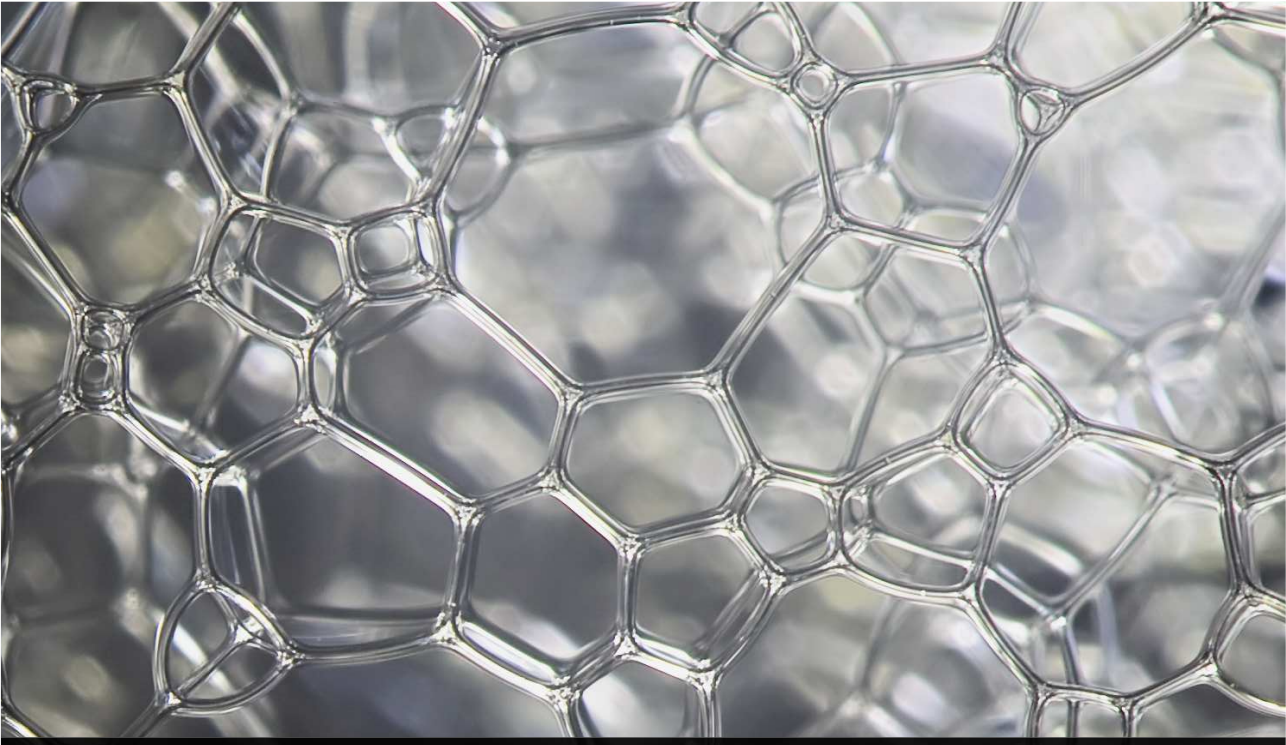
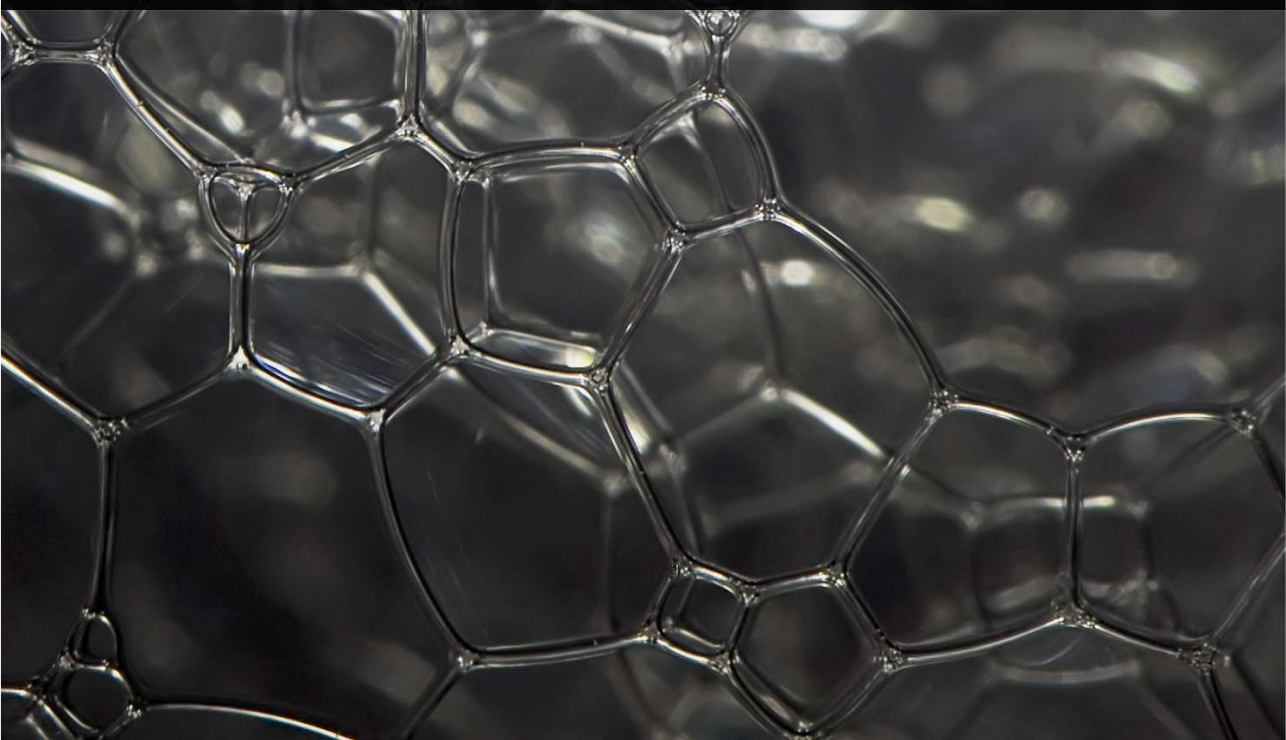


Part II

Nonlinear Acoustic Waves in Biological Media





Chapter 7

Time-Domain Nonlinear Acoustic Wave Modelling of Soft-Tissue Media

Abstract

A time-domain numerical code based on the constitutive relations of nonlinear acoustics is presented. To model frequency power law attenuation, such as observed in biological media, multiple relaxation processes are included and relaxation parameters are fitted to both exact frequency power law attenuation and empirically measured attenuation data of a variety of tissues. A computational technique based on artificial relaxation is included to correct the non-negligible numerical dispersion of the numerical method and to improve stability when shock waves are present. This technique avoids the use of high order finite difference schemes, leading to fast calculations. The accuracy of the method is discussed by comparison with analytical and k-space numerical solutions, and also to focused beam experimental data.

7.1 Introduction

The propagation of acoustics waves trough tissue for biomedical applications is usually linked to nonlinear propagation (Carstensen et al., 1980). Nonlinear regime is commonly achieved in therapy techniques in which the waves interact with the tissue to achieve some ultrasound bio-effect. On the other hand, most tissues shows very large acoustic attenuation coefficients at interest frequencies (Duck, 1990). Therefore, for most ultrasound imaging techniques the acoustic amplitude necessary to achieve a good signal/noise ratio is high enough to generate weakly nonlinear effects, while, in some applications, nonlinear effects are used as the basis of imaging and therapy techniques.

Thus, accurate prediction of finite amplitude acoustic waves traveling through biological media are essential in developing new therapy and imaging techniques for medical ultrasound applications (Carstensen et al., 1980; Muir et al., 1980). Numerous experimental studies show that attenuation $\alpha(f)$ of biological media exhibits a power law dependence on frequency $\alpha(f) = \alpha_0 f^\gamma$ over the frequency range used in medical applications (Hill et al., 2004; Duck, 1990). Considering an initial monochromatic plane wave traveling through nonlinear media, two opposite effects govern the final wave amplitude: on one hand, higher harmonics appear and their amplitude grows as a consequence of nonlinear progressive wave steepening; and on the other hand, the damping for each harmonic is different, following the above power law. Therefore, differences in the frequency power law model can lead to huge differences in attenuation of higher harmonics, and hence the inclusion of frequency dependence attenuation is critical for correctly predict nonlinear propagation.

7.1.1 Models of frequency power law media attenuation

Classical thermo-viscous sound attenuation exhibit a squared frequency dependence, $\gamma = 2$ (Pierce, 1989), however the empirically fitted power law for soft tissues typically ranges between $\gamma = (0.6, 2)$ (Goss et al., 1979; Duck, 1990; Hill et al., 2004). For most tissues the attenuation shows a dependence that can be modeled by γ close to the unity, where the specific value varies from different tissues. Moreover, for some individual examples the local value of γ exhibit lower values at low ultrasound frequencies and tends to 2 in the high frequency limit (Hill et al., 2004). Despite the study of the physical mechanism besides this complex frequency dependence is out of the scope of this work, there exist numerous phenomenological approaches for including the observed losses in the acoustic equations (Wismer et al., 1995; Kellya et al., 2009). On the other hand, is common in literature to describe the losses in soft tissues as multiple-relaxation processes (Nachman et al., 1990; Hill et al., 2004), from continuous distribution of relaxation processes (Jongen et al., 1986) to a discrete representation. Thus, relaxation parameters can be

optimized to fit the observed tissue attenuation, where has been shown that two processes are enough to model tissue attenuation with acceptable accuracy over frequency range covering about 4 octaves (Yang et al., 2005). Moreover, fractional partial differential operators can describe frequency power law attenuation (Caputo, 1967) when inserted into a wave equation. These operators can be included into wave modeling equations by means of time-causal convolutions (Szabo, 1994; Chen et al., 2003), fractional spatial derivatives (Chen et al., 2004) and its causal correction (Treeby et al., 2010), and combined time-space fractional derivatives (Caputo, 1967; Wismer, 2006). The latter operators can be biological motivated and derived from tissue micro-structure using fractal ladders based on networks of springs and dashpots (Kellya et al., 2009). However, these fractional loss operators can be also derived from a continuum of relaxation process (Nasholm et al., 2011), that suggest that the two approaches can be equivalent under certain conditions (Treeby et al., 2012).

7.1.2 Burgers equation

The above lossy operators can be included in a variety of nonlinear acoustic wave propagation models and, while analytical solutions are not available for finite amplitude waves in frequency power law media even in simplest configurations, a wide range of numerical methods has been developed. The numerical resolution of the nonlinear constitutive equations in tissue-like medium supposes a difficult problem due to the large size of the region of interest in relation to the size of the acoustic wavelength and the complexity of the model. Simplifying assumptions have been needed in the past for modeling nonlinear propagation in the past. Forward or one-way methods are the simplest way to model progressive nonlinear acoustic waves. The general representation of a causal media response was introduced in the Burgers equation (Blackstock, 1985) leading to the generalized Burgers equation. Thus, by choosing an adequate time function in the convolution kernel the attenuation and dispersion of an specific medium can be accurately modeled. The memory function can be modeled by a discrete sum of relaxation processes (Cleveland et al., 1996), while fractional time derivatives can also be included into the augmented Burgers equation (Ochmann et al., 1993).

7.1.3 KZK and one-way models

In order to describe finite amplitude sound beam diffraction effects in a paraxial approximation the well-known Khokhlov-Zabolotskaya-Kuznetsov equation (KZK) (Aanonsen et al., 1984; Lee et al., 1995) can be used. The KZK model can be extended for accounting for tissue attenuation by including relaxation (Cleveland et al., 1996; Yang et al., 2005) or fractional derivatives (Prieur et al., 2011). The KZK equation is commonly solved by a split operator techniques (Lee et al., 1995) that allows the frequency domain representation of the progressive wave. In this

way, the inclusion of tissue attenuation can be achieved efficiently in frequency domain (Khokhlova et al., 2006). Efficient and fast numerical solutions of the KZK model in power law media are also feasible under the assumption of Gaussian representation of the transverse field for each harmonic (Soneson et al., 2007). To overcome the validity of the parabolic approximation (i.e. when dealing with large aperture focused sound sources or modeling sound field near the acoustic source) many approaches has been proposed (Varslot et al., 2005). Also other phenomenological one-way approximations of finite amplitude sound beams has been developed (Christopher et al., 1991; Tavakkoli et al., 1998) and extended including tissue attenuation (Zemp et al., 2003). Furthermore, a numerical solution of the one-way version of the Westervelt equation (Yuldashev et al., 2011) has been also proposed.

7.1.4 Full-wave Westervelt type equations

Tissue inhomogeneity can be modeled in these one-way models (Jing et al., 2007), like transmission though tissue layers with refraction, but they do not take into account backscattering and multiple reflections. More realistic models, e.g. those accounting for scattering from internal tissue structures, are based on the Westervelt-type full-wave equations. Finite-Differences in Time-Domain methods (FDTD) can be applied to obtain explicit numerical schemes that account for nonlinear propagation and temperature rising in thermo-viscous media (Hallaj et al., 1999), where the inclusion of temperature-dependent sound speed changes can be also modeled (Hallaj et al., 2001). Tissue attenuation can be achieved in the Westervelt nonlinear wave equation by including multiple relaxation processes (Pinton et al., 2009) with optimized relaxation parameters. The Westervelt equation can be solved also by the Iterative Nonlinear Contrast Source (INCS) (Huijssen et al., 2010) where power law attenuation is modeled as a compliance relaxation function (Demi et al., 2011; Verweij et al., 2013). Other approach to include tissue losses in the Westervelt equation is to solve the model in k-space and directly include tissue looses in spatial frequency domain (Jing et al., 2012). This full-wave equation has been validated for strongly focused sources (Jing et al., 2011). However, due to the assumptions taken in the derivation of the Westervelt equation, the accuracy of this model is limited in practical situations as (*i*) the modeling of rigid boundaries where the thermo-viscous boundary layer effects are not-negligible, i.e. in general case where the particle velocity becomes rotational, (*ii*) situations where the second order Lagrangian density of acoustical energy not vanish, i.e. where plane progressive waves does not exist and the acoustic field becomes complex due to multiple scattering, reverberation or resonances, (*iii*) situations where the equilibrium-state particle velocity is not null, including the self generation of acoustic streaming. See Ref. Hamilton et al. (1998b) Chap. 3 for further discussion.

In this way, a physical model based on the constitutive relations of nonlinear

acoustics include a more complete description of the nonlinear acoustic phenomena over arbitrary boundary conditions, i.e. the time-space relations between the involved acoustic magnitudes remains exact.

7.1.5 Full-wave constitutive relations

The recent development of computational capacity has made possible to consider the full constitutive relations (i.e. without the assumptions discussed above). Thus, for small-amplitude acoustic waves, the linearized pressure-velocity formulation of constitutive relations in inhomogeneous media was solved by means of Finite-Differences in Time-Domain (FDTD) methods with frequency independent losses by Manry et al. (Manry et al., 1996), or using two-step MacCormack finite-differences scheme by Mast et al. (Mast et al., 1997). Also, relaxation processes can be included in finite difference methods in an efficient way in order to model tissue attenuation and dispersion (Yuan et al., 1999). Furthermore, k-space numerical methods have also been applied to solve the linearized first order equations in lossless inhomogeneous media (Mast et al., 2001). In order to account for soft tissue losses, the computational solution of the fractional Laplacian by k-space spectral methods have demonstrated to be extremely efficient due to the spatial frequency domain representation of the acoustic field (Treeby et al., 2010).

In the case of nonlinear constitutive relations models, the evolution of the acoustic magnitudes have been simulated in time-domain by means of finite differences schemes such as Dispersion Relation Preserving method (DRP) in ideal fluids and axisymmetric domains (Ginter et al., 2002). Thermo-viscous losses in finite-differences methods have been widely used, see Sparrow et al. (Sparrow et al., 1991). In order to introduce tissue attenuation in the governing equations time-dependent fractional derivatives can be included by convolutional operators. Thus, in Ref. Liebler et al. (2004) an efficient method has been presented, but although the memory requirements can be strongly reduced compared to direct convolutions the algorithm employs up to ten auxiliary fields and a memory buffer of three time steps. Furthermore, construction of specific causal memory functions that models soft tissue attenuation and dispersion in Navier-Stokes equations is also possible (Lobanova et al., 2014), but certain time history must be stored in memory and in this case the computational domain was restricted to one dimensional propagation.

In order to overcome those numerical limitations, recently k-space and pseudo-spectral numerical methods have been applied to constitutive relations in nonlinear regime to solve fractional Laplacian operators efficiently (Treeby et al., 2012). Furthermore, in the case of domains of hundreds of wavelengths, when the cumulative phase error due to numerical dispersion of standard finite-difference schemes can not be neglected, those spectral numerical methods have reported an improvement in accuracy of the numerical solution. This two factors, i.e. the negligible numerical dispersion and the efficient resolution of fractional Laplacian operators, have

led the spectral methods to be widely used in practical applications. However, their main limitation is that the implementation of natural space discontinuities due to tissue layers or rigid boundary conditions leads to errors in the reconstruction of the spectral information due to the poor convergence of Fourier series at jumps, i.e. the well-known Gibbs oscillations. Preventing this kind of errors is typically achieved by filtering the spatial spectrum (Jing et al., 2012), so the theoretical spatial minimum sampling of two point per wavelength becomes larger. In addition, these errors propagate globally and affect to the accuracy all over the domain, in contrast with locally propagating errors in finite differences methods. On the other hand, taking into account the spatial discontinuity due to symmetry boundary condition, axisymmetric domains becomes not feasible by standard k-space methods, and full 3D domains must be employed even for axisymmetric configurations. Those errors can be prevented by means of the recently developed Fourier Continuation (FC) method (Albin et al., 2012). However, the discontinuities formed due to shock propagation are still not solved by FC methods and other additional numerical treatment must be applied for correctly describe shock formation, e.g. intensive computations by high order accurate weighted essentially non-oscillatory schemes (FC/WENO) (Shahbazi et al., 2011). Unlikely, the computational times increases by using those intensive computational techniques and the multiresolution analysis to detect discontinuities in the domain.

The aim of the present chapter is to present a generalization of the constitutive relations of nonlinear acoustics including multiple relaxation processes in a non-convolutional formulation that allows the time-domain numerical solution by an explicit finite differences numerical scheme. Frequency power law attenuation based in relaxation have been applied in the same way than it has been applied to generalized Burgers equation (Cleveland et al., 1996), Khokhlov-Zabolotskaya-Kuznetsov (KZK) model (Cleveland et al., 1996; Yang et al., 2005) and Westervelt equation (Pinton et al., 2009). The relaxation parameters have been fitted to both exact frequency power law attenuation and empirically measured attenuation of a variety of tissues that does not fit an exact power law. Two processes have been enough to model tissue attenuation with acceptable accuracy over a frequency range covering about 4 octaves, as it was demonstrated by Yang et al. (Yang et al., 2005). A numerical technique based on artificial relaxation is included to control the non-negligible numerical dispersion of the FDTD method and improve stability when shock waves are present in the solution. The method includes backscattering and arbitrary propagation direction of finite amplitude beams, and can be specially suitable in axisymmetric configurations where the computational resources for full 3D k-space methods are prohibitive.

7.2 Generalized nonlinear acoustics model for multiple relaxation media

7.2.1 Full-wave modeling

The principles of mass and momentum conservation lead to the main constitutive relations for nonlinear acoustic waves, which for a fluid can be expressed as (Naugolnykh et al., 1998)

$$\frac{\partial \rho}{\partial t} = -\nabla \cdot (\rho \mathbf{v}) \tag{7.1}$$

and

$$\rho \left(\frac{\partial \mathbf{v}}{\partial t} + \mathbf{v} \cdot \nabla \mathbf{v} \right) = -\nabla p + \eta \nabla^2 \mathbf{v} + \left(\zeta + \frac{\eta}{3} \right) \nabla \left(\nabla \cdot \mathbf{v} \right), \tag{7.2}$$

where ρ is the total density field, $\mathbf{v}$ is the particle velocity vector, p is the pressure, and η and ζ are the coefficients of shear and the bulk viscosity respectively. The acoustic waves described by this model exhibit viscous losses with quadratic power law dependence on frequency. In order to include a power law frequency dependence on the attenuation, a multiple relaxation model will be added into the time domain equations.

The basic mechanism for energy loss in relaxing media is the appearance of a phase shift between the pressure and density fields. This behavior is commonly modeled as a time dependent relation at the fluid state equation, that for a fluid retaining the material nonlinear effects up to second order an be expressed as (Naugolnykh et al., 1998; Rudenko et al., 1977):

$$p = c_0^2 \rho' + \frac{c_0^2}{\rho_0} \frac{B}{2A} \rho'^2 + \int_{-\infty}^{t} G(t - t') \frac{\partial \rho'}{\partial t} dt, \tag{7.3}$$

where $\rho' = \rho - \rho_0$ is the density perturbation over the stationary density ρ_0, B/A is the nonlinear parameter, c_0 is the small amplitude sound speed, and $G(t)$ is the kernel associated with the relaxation mechanism. The first two terms of the right hand side of Eq. (7.3) describe the instantaneous response of the medium, where the convolutional third term accounts for the "memory time" of the relaxing media. Thus, by choosing an adequate time function for the kernel $G(t)$ the model can present an attenuation and dispersion response that fits the experimental data of the heterogeneous media. However, the direct resolution of the constitutive relations (7.1-7.3) in this integral form is a complex numerical task due to the convolutional operator. Thus, instead of describe $G(t)$ with a specific time domain waveform, the response of the heterogeneous medium can be alternatively described by a sum of N relaxation processes with exponential time dependence

as:

$$\int_{-\infty}^{t} G(t-t')\frac{\partial \rho'}{\partial t}dt = \sum_{n=1}^{N} G_n * \frac{\partial \rho'}{\partial t}, \tag{7.4}$$

with the n-th order relaxation kernel expressed as

$$G_n(t) = \eta_n c_0^2 \, \mathrm{e}^{\frac{-t}{\tau_n}} H(t), \tag{7.5}$$

where $H(t)$ is the Heaviside piecewise function $H(t<0)=0$, $H(t>0)=1$, τ_n is the characteristic relaxation time and η_n the relaxation parameter for the n-th order process. This last dimensionless parameter controls the amount of attenuation and dispersion for each process as $\eta_n = (c_n^2 - c_0^2)/c_0^2$, where c_n is the sound speed in the high frequency limit associated to n-th order relaxation process, also known as the speed of sound in the "frozen" state (Pierce, 1989). In order to describe relaxation without the need of including a convolutional operator, we shall define a state variable S_n for each process as

$$S_n = \frac{1}{\tau_n} G_n * \rho'. \tag{7.6}$$

Thus, using the convolutional property $\frac{\partial}{\partial t}\left(G(t) * \rho'(t)\right) = \frac{\partial G(t)}{\partial t} * \rho'(t) = G(t) * \frac{\partial \rho'(t)}{\partial t}$, the time derivative of the relaxation state variable obeys the following relation for the n-th order process:

$$\frac{\partial S_n}{\partial t} = \left(-\frac{1}{\tau_n}\frac{\eta_n c_0^2}{\tau_n} \mathrm{e}^{-\frac{t}{\tau_n}} H(t) + \frac{\eta_n c_0^2}{\tau_n} \mathrm{e}^{-\frac{t}{\tau_n}} \delta(t) \right) * \rho' \tag{7.7}$$

where $\delta(t)$ is the Dirac delta function. Using the Eq. (7.6) this relation becomes a simple ordinary differential equation for each process as

$$\frac{\partial S_n}{\partial t} = -\frac{1}{\tau_n} S_n + \frac{\eta_n c_0^2}{\tau_n} \rho'. \tag{7.8}$$

Using again convolutional properties, we can substitute Eq. (7.8) into (7.4), and the relaxing nonlinear state Eq. (7.3) becomes

$$p = c_0^2 \rho' + \frac{c_0^2}{\rho_0}\frac{B}{2A}\rho'^2 - \sum_{n=1}^{N} S_n + \sum_{n=1}^{N} \eta_n c_0^2 \rho'. \tag{7.9}$$

Moreover, if "frozen" sound speed for N mechanisms is defined as $c_\infty^2 = c_0^2\left(1 + \sum_{n=1}^{N} \eta_n\right)$, Eq. (7.9) leads to

$$p = c_\infty^2 \rho' + \frac{c_0^2}{\rho_0}\frac{B}{2A}\rho'^2 - \sum_{n=1}^{N} S_n. \tag{7.10}$$

Due to the smallness of the relaxation parameter, η_n, i.e. when weak dispersion is modeled, the sound speed in the high frequency limit reduces to (Naugolnykh et al., 1998):

$$c_\infty = c_0 \left(1 + \sum_{n=1}^{N} \frac{\eta_n}{2} \right). \tag{7.11}$$

Note Eq. (7.10) for a mono-relaxing media is equivalent to that can be found in literature (Rudenko et al., 1977)

$$p = c_\infty^2 \rho' + \frac{c_0^2}{\rho_0} \frac{B}{2A} \rho'^2 - \int_{-\infty}^{t} \frac{\eta c_0^2}{\tau} \mathrm{e}^{-\left(\frac{t-t'}{\tau}\right)} \rho'(t'). \tag{7.12}$$

Thus, the constitutive relations to solve by means of the numerical method in the nonlinear regime are the continuity Eq. (7.1), the motion Eq. (7.2) and the second order fluid state relaxing Eq. (7.10), where the state variable S_n obeys the relation (7.8) for the n-th order relaxation process. Although the aim of this work is to model biological media, the generalized formulation presented here can be used to describe the attenuation and hence the dispersion observed in other relaxing media, as the relaxation processes of oxygen and nitrogen molecules in air or the relaxation associated with boric acid and magnesium sulfate in seawater (Pierce, 1989).

7.2.2 Small amplitude modeling

If small amplitude perturbations are considered, an equivalent derivation of this model can be expressed for multiple relaxation media (Yuan et al., 1999). Thus, for an homogeneous inviscid relaxing fluid the linearized continuity and motion Eq. (7.1-7.2) reduces to

$$\frac{\partial \rho}{\partial t} = -\rho_0 \nabla \cdot \mathbf{v} \tag{7.13}$$

and

$$\rho_0 \frac{\partial \mathbf{v}}{\partial t} = -\nabla p, \tag{7.14}$$

and linearizing the fluid state Eq. (7.10) we obtain:

$$\rho' = \frac{1}{c_\infty^2} \left(p + \sum_{n=1}^{N} S_n \right). \tag{7.15}$$

These equations can be solved directly in this form, however, if expressed in pressure-velocity formulation the density field is no longer necessary and computational effort can be reduced. Thereby, assuming a linear "instantaneous"

compressibility $\kappa_\infty = \rho_0 c_\infty^2$, and substituting Eq. (7.15) into Eq. (7.13) yields

$$\frac{\partial p}{\partial t} + \sum_{n=1}^{N} \frac{\partial S_n}{\partial t} = -\kappa_\infty \nabla \cdot \mathbf{v}. \tag{7.16}$$

Then, taking the time derivative of the state variable Eq. (7.8) we get

$$\frac{\partial p}{\partial t} - \sum_{n=1}^{N} \frac{1}{\tau_n} S_n + \rho' \sum_{n=1}^{N} \frac{\eta_n c_0^2}{\tau_n} = -\kappa_\infty \nabla \cdot \mathbf{v}. \tag{7.17}$$

Finally, substituting again the linearized state Eq. (7.15) and arranging terms the linearized continuity equation leads to

$$\frac{\partial p}{\partial t} + p \sum_{n=1}^{N} \frac{\eta_n c_0^2}{\tau_n c_\infty^2} + \sum_{n=1}^{N} \left(\frac{\eta_n c_0^2}{\tau_n c_\infty^2} - \frac{1}{\tau_n} \right) S_n = -\kappa_\infty \nabla \cdot \mathbf{v}. \tag{7.18}$$

On the other hand, the state evolution equation can be expressed as a function of the acoustic pressure as

$$\frac{\partial S_n}{\partial t} = -\frac{1}{\tau_n} S_n + \frac{\eta_n c_0^2}{\tau_n c_\infty^2} \left(p - \sum_{n=1}^{N} S_n \right). \tag{7.19}$$

Thus, the linearized governing Eq. (7.14, 7.18) for a relaxing media are expressed in a pressure-velocity formulation and can be solved together with the coupled state evolution equation (7.19) by means of standard finite differences numerical techniques (Yuan et al., 1999). In this way, lossless linear acoustics equations can be obtained by setting $\eta_n = 0$ or in the limit when the relaxation times $\tau_n \to \infty$. The relaxation behavior described by this linearized model is achieved too by the formulation described by (Yuan et al., 1999), where the relaxation coefficients η_n and the relaxation variable S_n are defined in a different, but analogous way.

7.3 Numerical solution by finite differences in time domain

In this section the numerical techniques for solving the complete set of equations (continuity Eq. (7.1), momentum Eq. (7.2), state Eq. (7.10) and the relaxation Eq. (7.8)) are presented. The numerical method is based on a second order FDTD method where multiple relaxation processes are included in order to: first, modeling physical attenuation and dispersion in the interest frequencies and second,

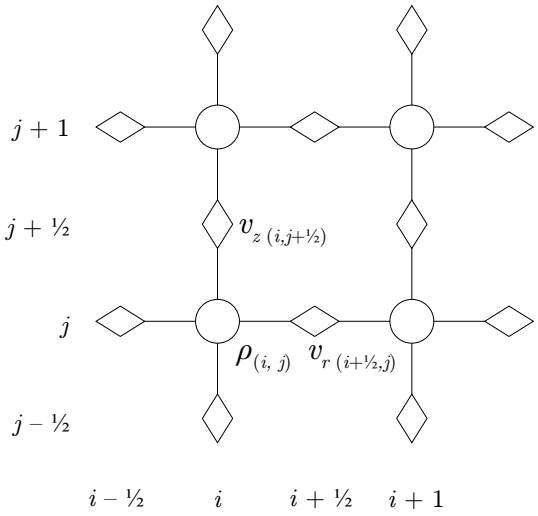


Figure 7.1: Spatial discretization as in standard acoustics FDTD method. The pressure ($p^m_{i,j}$) and the n-th order relaxation process state fields ($S^m_{n,i,j}$) are evaluated at same discrete location as the density ($\rho^m_{i,j}$). Particle velocity fields are discretized staggered in both space and time respect to the density, pressure and the n-th order state fields.

correct the numerical dispersion and include artificial attenuation to guarantee convergence in nonlinear regime. Moreover the inclusion of relaxation processes in the presented formulation require only one extra field per relaxation process and no memory buffer is needed.

7.3.1 Discretization

Cylindrical axisymmetric $\mathbf{x} = (r, z)$ coordinate system is considered in this work, however, the method can be derived in other coordinate system. As in the standard acoustic FDTD method (Botteldooren, 1996), the particle velocity fields are discretized staggered in time and space respect to the density and pressure fields. As shown in Fig. 7.1 uniform grid is considered, where $r = i\Delta r$, $z = j\Delta z$, $t = m\Delta t$, with Δr and Δz as the radial and axial spatial steps, and Δt is the temporal step.

Centered finite differences operators are applied over the partial derivatives of the governing equations. Thus, spatial interpolation is needed over the off-center grid variables in order to fulfill the conservation principles over each discrete cell of the domain (LeVeque, 1992). The r component of Eq. (7.2) is expressed in a

cylindrical axisymmetric system as

$$\begin{aligned}\frac{\partial v_r}{\partial t} =& -\frac{1}{\rho}\frac{\partial p}{\partial r} - v_r\frac{\partial v_r}{\partial r} - v_z\frac{\partial v_r}{\partial z} \\ &+ \frac{\eta}{\rho}\left(\frac{\partial^2 v_r}{\partial r^2} + \frac{1}{r}\frac{\partial v_r}{\partial r} + \frac{\partial^2 v_r}{\partial z^2} - \frac{v_r}{r^2}\right) \\ &+ \frac{1}{\rho}\left(\zeta + \frac{1}{3}\eta\right)\left(\frac{\partial^2 v_r}{\partial r^2} + \frac{1}{r}\frac{\partial v_r}{\partial r} + \frac{\partial^2 v_z}{\partial r \partial z} - \frac{v_r}{r^2}\right).\end{aligned} \tag{7.20}$$

Each term of the above expression is approximated by centered finite differences evaluated at $r = (i + \frac{1}{2}) \cdot \Delta r$, $z = (j + \frac{1}{2}) \cdot \Delta z$, $t = (m + \frac{1}{2}) \cdot \Delta t$. This equation can be solved obtaining an update equation for $v_{r_{i+\frac{1}{2},j}}^{m+\frac{1}{2}}$. In the same way, the z component of the motion equation (7.2) is expressed as

$$\begin{aligned}\frac{\partial v_z}{\partial t} =& -\frac{1}{\rho}\frac{\partial p}{\partial z} - v_r\frac{\partial v_z}{\partial r} - v_z\frac{\partial v_z}{\partial z} \\ &+ \frac{\eta}{\rho}\left(\frac{\partial^2 v_z}{\partial r^2} + \frac{1}{r}\frac{\partial v_z}{\partial r} + \frac{\partial^2 v_z}{\partial z^2}\right) \\ &+ \frac{1}{\rho}\left(\zeta + \frac{1}{3}\eta\right)\left(\frac{\partial^2 v_r}{\partial z \partial r} + \frac{1}{r}\frac{\partial v_r}{\partial z} + \frac{\partial^2 v_z}{\partial z^2}\right).\end{aligned} \tag{7.21}$$

This equation is approximated by centered finite differences and evaluated at $r = i \cdot \Delta r$, $z = (j + \frac{1}{2}) \cdot \Delta z$, $t = m \cdot \Delta t$. An update equation is obtained solving this equation for $v_{z_{i,j+\frac{1}{2}}}^{m+\frac{1}{2}}$. The equation (7.1) in cylindrical axisymmetric coordinate system is expressed as

$$\frac{\partial \rho}{\partial t} = -\rho\left(\frac{\partial v_r}{\partial r} + \frac{v_r}{r} + \frac{\partial v_z}{\partial z}\right) - v_r\frac{\partial \rho}{\partial r} - v_z\frac{\partial \rho}{\partial z}. \tag{7.22}$$

Following the same procedure, each term of the above expression is approximated by centered finite differences and evaluated at $r = i \cdot \Delta r$, $z = j \cdot \Delta z$, $t = (m + \frac{1}{2}) \cdot \Delta t$, and the update equation is obtained solving this expression for $\rho_{i,j}^{m+1}$.

A leap-frog time marching is applied to solve Eq. (7.20-7.22) for each time step until the desired simulation time is reached. Finally, Eq. (7.8) is locally solved for $m + 1$ by and explicit fourth-order Runge-Kutta method and then Eq. (7.10) is evaluated.

7.3.2 Boundary conditions

The staggered grid is terminated on velocity nodes, so the boundary conditions are applied on these external nodes, allowing to prevent the singularity of the cylindrical coordinate system: due to the staggered grid, the only variable discretized at

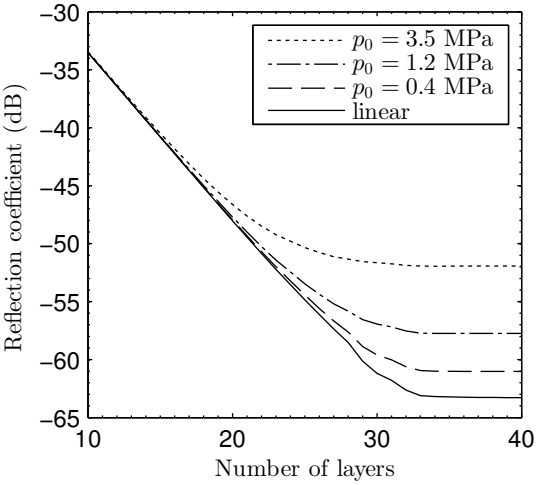


Figure 7.2: Reflection coefficient of the perfectly matched layer (PML) versus number of layers for different wave amplitudes.

$r = 0$ is v_r, and axisymmetric condition $v_r|_{r=0} = 0$ is applied there. Furthermore, to solve spatial differential operators at boundaries some "ghost" nodes must be created with the conditions: $v_r(-r) = -v_r(r)$, $v_z(-r) = v_z(r)$, $\rho(-r) = \rho(r)$ and $p(-r) = p(r)$.

Perfectly matched layers (PML) (Liu et al., 1997) were placed in the limits of the domain ($\pm z$ and $+r$) to avoid spurious reflections from the limits of the integration domain. Inside the PML domains linearized acoustic equations were solved using the complex coordinate screeching formulation (Liu, 1999). For a layer of 30 elements and a broadband incident wave with 1 MHz central frequency and non-normal incidence angle, these absorbent boundary conditions have reported a reflection coefficient of $R = -55.2$ dB.

However, the performance of the PML is amplitude dependent as long the nonlinear terms are uncoupled to the PML domains. The amplitude dependence of the reflection coefficient is shown in Fig. 7.2, where a PML of 25 elements thickness have reported reflection coefficients $R < -50$ dB for waves in linear regime and highly nonlinear waves including shocks.

7.3.3 Minimizing numerical dispersion

The stability for the lossless linear FDTD algorithm follows the Courant-Friedrich-Levy (CFL) condition, that for uniform grid ($\Delta r = \Delta z = \Delta h$) the maximum duration of the time step is limited by $\Delta t \leq \Delta h / c_0 \sqrt{D}$ where D is the number of dimensions (i.e. $D = 2$ in cylindrical axisymmetric coordinate system). That

condition essentially states that for a single time step information can not propagate in the numerical grid a distance longer that one cell. However, if relaxation is included numerical instabilities have been observed when $\tau_f/2\pi < \Delta t$. Due to this empirical relation, the maximum values for relaxation frequencies are limited too by the chosen spatial discretization by the simple relation $f_n < \sqrt{2}N_\lambda f_0$, where $f_n = 2\pi/\tau_n$ is the maximum relaxation frequency for all processes, N_λ is the number of spatial samples per wavelength and f_0 the frequency of the propagating wave.

On the other hand, nonlinear effects induce the progressively growing of harmonics of the fundamental frequency of the initial wave. The diffusive viscous terms in Eq. (7.2), attenuates the small-amplitude high-spatial frequencies, damping the "node to node" numerical oscillations and ensuring numerical stability in weakly nonlinear regime. Thus, for a smooth solution the numerical algorithm shows consistency when $\Delta h \to 0$, so if stability is achieved by the CFL condition, the convergence is guaranteed. However, in strongly nonlinear regime, i.e. when sharp waveforms or even shocks are present in the solution, extra numerical techniques must be employed to guarantee convergence. Artificial viscosity can be added when shock waves are present in the solution where a common implementation follows a fourth order spatial filtering (Sparrow et al., 1991; Ginter et al., 2002). Thus, the artificial attenuation retrieved by this spatial operator is fourth power of frequency: the low frequency components of the solution remains quasi-undamped, while the higher spatial frequencies are strongly attenuated. In this way, the solution is smoothed and shock thickness depends on the artificial viscosity coefficient.

However, the main drawback for finite difference methods is numerical dispersion, where the analytic dispersion relation can be expressed in 1D as

$$\sin^2 \frac{k\Delta h}{2} = \frac{1}{S^2} \sin^2 \frac{\omega \Delta t}{2}, \tag{7.23}$$

with the Courant number $S = c_0\Delta t/\Delta h$. In this way, numerical dispersion reduces phase speed for high frequency components so traveling sharp solutions develop tail oscillations: the low wavenumbers travels fast and left behind high spatial frequencies. In nonlinear regime, is well-known that the combined effects of nonlinearity and strong dispersion can lead rich phenomena, e.g. beatings in the generated harmonics, pulsations on the vertex of a sawtooth wave or soliton formation in strong dispersive media (Rudenko et al., 1977). In this way, the numerical dispersion by discreteness of the FDTD methods couple to the physical nonlinearity can lead to a great variety of non-physical or even unstable solutions.

In order to overcome those two limitations, i.e. the generation of harmonics over the discrete limit and the numerical dispersion, we propose the use of artificial relaxation. Physical relaxation processes introduces *anomalous* dispersion, i.e. the phase speed increases in the high frequency regime, opposite to the numerical (lattice) dispersion described above. Thus, by introducing a collection of

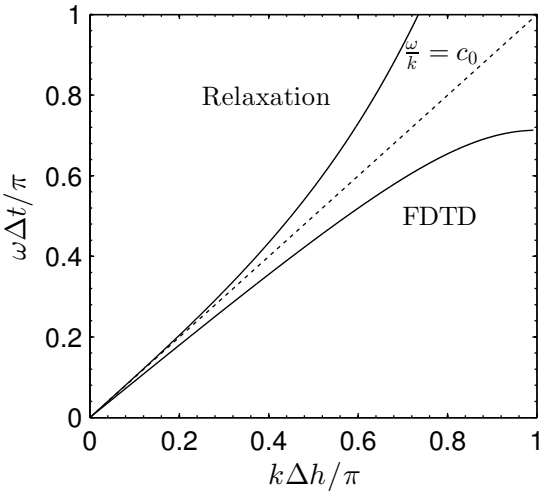


Figure 7.3: Normalized dispersion relation for of a FDTD lattice of Courant number $S = 0.9$ and *anomalous* dispersion relation for a mono relaxing acoustic media. The straight line $c_0 = \omega/k$ represents the reference nondispersive case.

relaxation processes and choosing its adequate relaxation parameters the high frequency numerical dispersion can be compensated. As a consequence, introduction of those relaxation processes in the high frequency lead to the inevitable inclusion of artificial attenuation. However, this numerical attenuation is then exploited to limit the growing of higher harmonics in a similar way than artificial viscosity (Sparrow et al., 1991). It is worth noting here that, due to the attenuation using artificial relaxation is, at maximum, only second power of frequency, the low frequency range of the solution is therefore also attenuated. Thus, the proposed method is restricted to lossy media.

The adequate relaxation parameters that corrects the numerical dispersion have been found by multi-objective optimization techniques, where two cost function are proposed: one for dispersion and other for attenuation. In the first case, the error between the goal (ideal) dispersion relation and the retrieved numerical dispersion corrected by multiple artificial relaxation and is evaluated in the high frequency regime. Finally, the second cost function is the error between the desired (ideal) attenuation and the artificial attenuation evaluated in the low frequency regime.

7.4 Validation

7.4.1 Single relaxation process

A canonical case of a physical single relaxation process is presented. In order to correct numerical dispersion the parameters of two extra artificial relaxation processes have been found using the multi-objective genetic algorithms provided by the optimization toolbox in MATLAB R2014a v8.03. Linear propagation was considered and simulation parameters were set to typical values for water: $c_0 = 1500$ m/s, $\rho_0 = 1000$ kg/m^3, $B/A = 5$, $\eta = 8.90 \cdot 10^{-4}$ Pa·s. A single physical relaxation process was included, with a characteristic relaxation time of $\tau_1 = 1/2\pi f_0$ and $f_0 = 2$ MHz, and relaxation modulus of $\eta_1 = 0.0134$ that leads to a frozen sound speed of $c_\infty = 1510$ m/s. In this case, the numerical parameters were set to $\Delta r = \Delta z = 1.87 \cdot 10^{-7}$ m and $\Delta t = 8.65 \cdot 10^{-11}$ s. A plane wave traveling in $+z$ direction was considered.

Thus, the theoretical attenuation for the relaxation processes and including viscosity can be expressed as

$$\alpha(\omega) = \frac{\omega^2}{2\rho_0 c_0^3}\left(\zeta + \frac{4}{3}\eta\right) + \sum_{n=1}^{N} \frac{\eta_n}{2c_0\tau_n}\frac{\omega^2\tau_n^2}{1+\omega^2\tau_n^2}, \tag{7.24}$$

and the theoretical phase velocity can be predicted as (Pierce, 1989)

$$c_p(\omega) = c_0\left(1 + \sum_{n=1}^{N} \frac{\eta_n}{2}\frac{\omega^2\tau_n^2}{1+\omega^2\tau_n^2}\right). \tag{7.25}$$

In order to compute the attenuation and dispersion of the numerical method, simulated pressure was recorded at two locations z_0 and z_1, and attenuation and phase velocity were estimated from the spectral components over the bandwidth of the input signal. The numerical attenuation was calculated as

$$\alpha(\omega)_{fd} = \frac{\ln\left(|P(\omega, z_1)/P(\omega, z_0)|\right)}{(z_1 - z_0)}, \tag{7.26}$$

where $P(\omega)$ is the Fourier transform of the measured pressure waveforms at points z_0 and z_1. On the other hand, the phase velocity was computed as

$$c_p(\omega)_{fd} = \frac{\omega \cdot (z_1 - z_0)}{\arg\left(P(\omega, z_1)/P(\omega, z_0)\right)}, \tag{7.27}$$

where correct phase unwrapping is needed.

In this way, Fig. 7.4 shows the retrieved Pareto front of the optimization, where 3 different areas can be distinguished. The first area, marked as (A) in Fig. 7.4, represents individuals those numerical dispersion is minimal but attenuation is not optimal. On the other hand, the individuals around area (B) represent a set of relaxation parameters that provides the best agreement between numerical and physical attenuation. A good compromise between both situations can be obtained in the central area of the Pareto front (C), where retrieved attenuation and dispersion in the low frequency band shows good agreement with the physical, and the numerical dispersion has been corrected over a wide frequency range. However, as can be seen in the inset of Fig. 7.4, the dispersion relation retrieved by all the cases corrects the FDTD lossless numerical dispersion relation. The phase speed of those tree individuals is shown in Fig. 7.5 b), where it can be seen that in the frequency range selected for the optimization the numerical phase speed is corrected for all the individuals, where the best fit is obtained for individuals in the Pareto front area A. On the other hand, the inclusion of artificial relaxation leads to an increasing of the attenuation in the high frequency range, as is shown in Fig. 7.5 a). In this way, as the phase speed error is reduced the effect of artificial attenuation increases. Although this increasing can be seen as a non-desired counterpart, the appearance of this attenuation is useful in order to control the harmonic growing in nonlinear regime in the same way as artificial viscosity

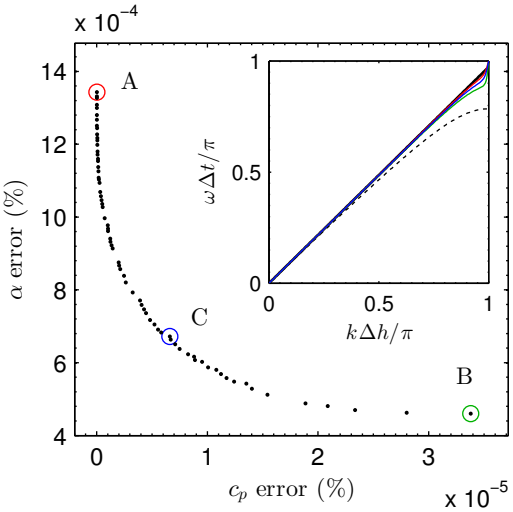


Figure 7.4: Pareto front retrieved by the multi-objective genetic optimization. Red marker (A) is the solution those relaxation parameters minimizes the numerical dispersion. The best fit in the attenuation are the parameters that provided the solution marked by green circle (B). A compromise between attenuation and dispersion is achieved at the individuals in the center of the Pareto front as the sample marked by blue circle (C). The inset shows the normalized dispersion relation retrieved by the individuals A-C. Dashed black line shows the numerical dispersion relation of the FDTD method for a Courant number of 0.94 without artificial relaxation.

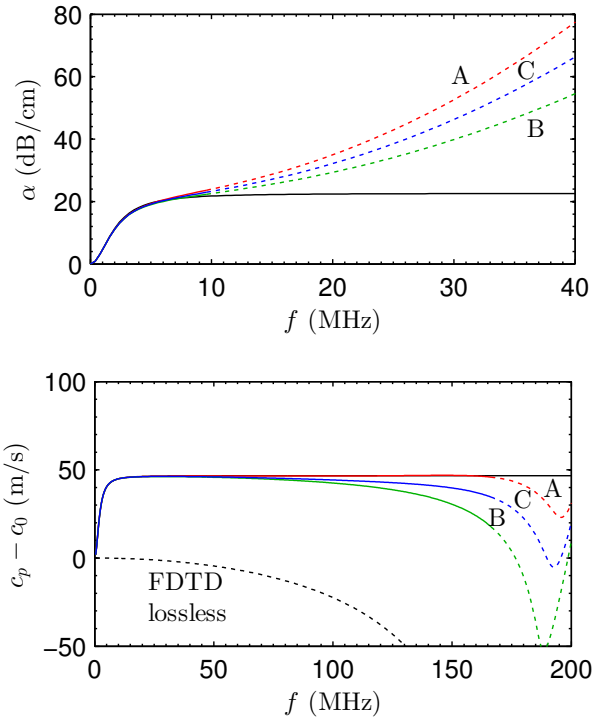


Figure 7.5: Retrieved attenuation (Up) and dispersion (Down) by the inclusion of artificial relaxation for the individuals A (red), B (green) and C (blue) of Fig. 7.4. Continuous lines represent the frequency range included by the optimization and dashed lines the not useful frequency range. As a consequence of correcting dispersion appears attenuation in the high frequency range that will be used as artificial attenuation for nonlinear stability.

spatial operators (Sparrow et al., 1991).

7.4.2 Nonlinear steady solution for single relaxation process

In order to validate the method in the nonlinear regime a full-wave simulation was developed in a mono-relaxing media using above parameters. Thus, the analytical (inverted) solution for the steady solution with $p = -p_0$ for $\tau = -\infty$, $p = p_0$ for $\tau = \infty$ and $p = 0$ for $\tau = 0$, for the retarded time $\tau = t - z/c_0$ reads (Hamilton et al., 1998b)

$$\tau = \tau_n \ln \frac{(1 + p/p_0)^{D-1}}{(1 - p/p_0)^{D+1}} \tag{7.28}$$

where $D = \eta_n \rho_0 c_0^2 / 2\beta p_0$ measures the ratio of relaxation effects to nonlinear effects.

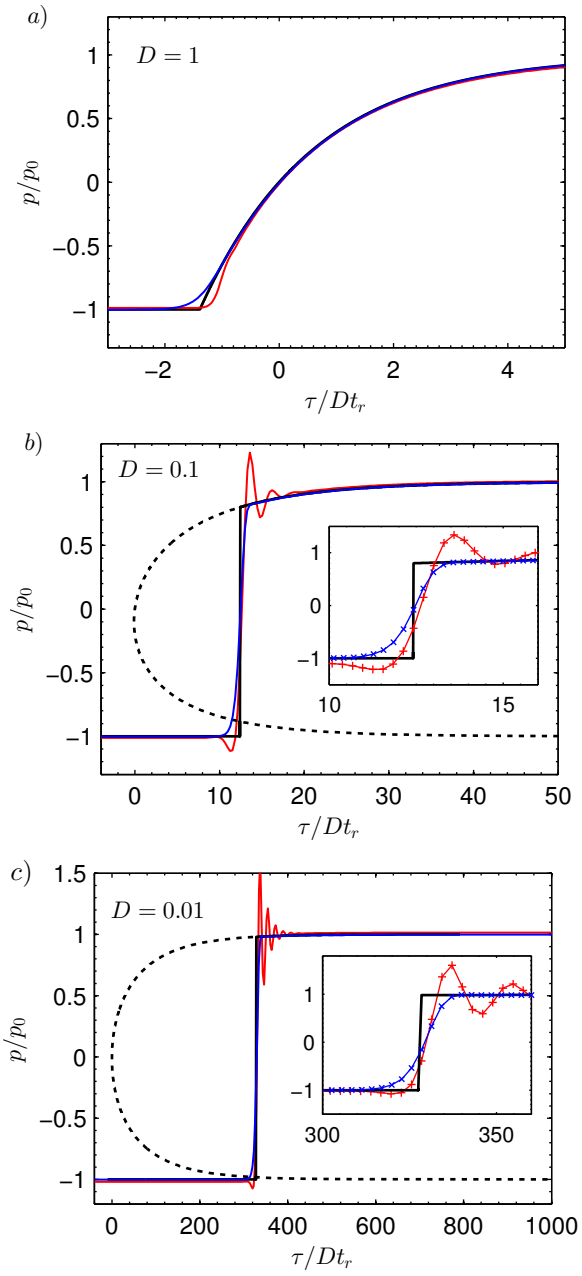


Figure 7.6: a) Analytical (gray line), numerical using artificial relaxation with corrected dispersion (blue line) and artificial viscosity (red) (Sparrow et al., 1991) for the nonlinear steady state solution for D=1. b) Nonlinear steady state solution for D=0.1. Inset shows detailed shock numerical solution for artificial relaxation (blue) and artificial viscosity (red). c) Nonlinear steady state solution for D=0.01.

For $D > 1$, where no shock is present, the solution retrieved by FDTD algorithm shows good agreement with analytical and no artificial relaxation is needed. However, for $D < 1$ a discontinuity is present in the solution and convergence is only possible with the inclusion of extra numerical techniques.

Thus, Fig. 7.6 (a-c) shows the analytical and numerical solutions including artificial relaxation and artificial viscosity, where excellent agreement is achieved in all cases. In the case of artificial viscosity, higher harmonics are strongly attenuated and by reducing grid step convergence can be achieved. However, as long the phase speed of the higher spatial frequencies present in the shock is modified due to numerical dispersion, oscillations appears in the tail of the discontinuity, leading to the appearance of non-physical solutions. On the other hand, the artificial attenuation by relaxation also limits the harmonic growing so a smooth version of the shock appears. Moreover, artificial relaxation also corrects phase velocity so all the spatial frequencies travels at same speed and no oscillatory tail appears. The case of $D = 0.01$ is shown in Fig. 7.6 c), where nonlinear effects strongly dominates over attenuation. In this case, tail oscillations provided by artificial viscosity increases in amplitude. In contrast, by including artificial relaxation a smoothed version of the shock is captured and accuracy is maintained.

7.5 Results

7.5.1 Frequency power law attenuation

Using methodology described above, the optimal relaxation parameters were obtained in order to fit the multiple-relaxation numerical attenuation to frequency power law attenuation in the form

$$\alpha(\omega) = \alpha_0 \omega^{\gamma}, \tag{7.29}$$

where γ is the power law exponent and α_0 the power law coefficient in Np $(\mathrm{rad/s})^{\gamma}\mathrm{m}^{-1}$. Moreover, the numerical dispersion was corrected by means of artificial relaxation in order to fit the corresponding frequency power law dispersion, where its analytical form satisfying causality can be expressed as (Waters et al., 2005)

$$\frac{1}{c_p\left(\omega\right)} = \frac{1}{c(\omega_0)} + \alpha_0 \tan\left(\frac{\pi\gamma}{2}\right)\left(|\omega|^{\gamma-1} - |\omega_0|^{\gamma-1}\right). \tag{7.30}$$

This expression is valid for $0 < \gamma < 3$ with $\gamma \neq 1$, and an alternate equation can be found (Waters et al., 2005) in the limit for $\gamma = 1$. Here, simulation parameters were $c_0 = 1500$ m/s, $\rho_0 = 1000$ kg/m^3, $B/A = 5$, $\eta = 8.90 \cdot 10^{-4}$ Pa·s, $f_0 = 1$ MHz, $\Delta r = \Delta z = 1.3 \cdot 10^{-5}$ m, $\Delta t = 5.4 \cdot 10^{-9}$ s; that leads to 26 elements per wavelength and a CFL number of 0.9. Only two independent relaxation processes were employed in this section to obtain the target frequency power laws.

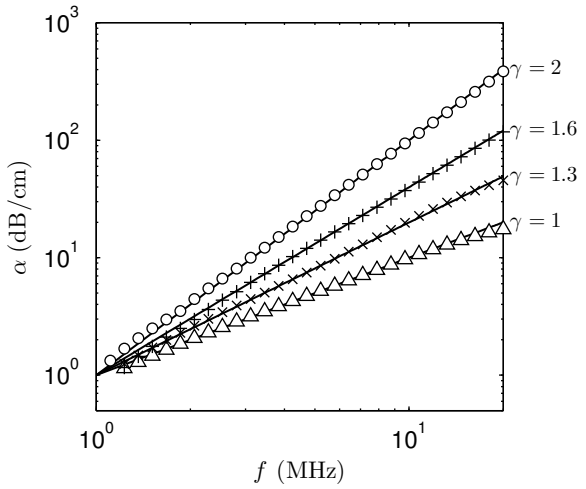


Figure 7.7: Attenuation retrieved by the numerical algorithm (markers) and target frequency power law attenuation (gray lines). By using the optimization algorithm the relaxation times and modulus were optimized for minimize the relative error between the target power laws of $\gamma = [1, 1.3, 1.6, 2]$ and the attenuation retrieved.

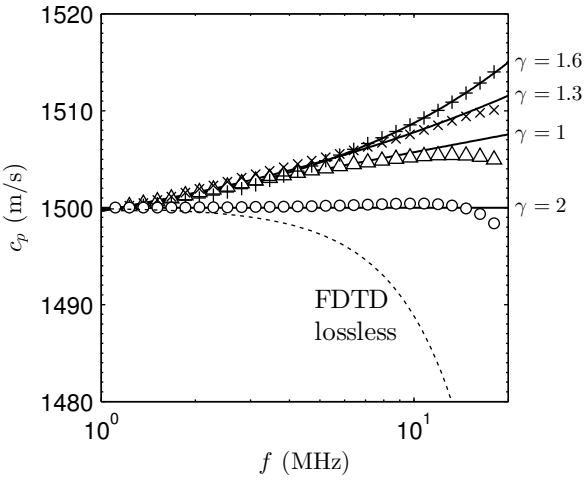


Figure 7.8: Phase speed retrieved by the numerical algorithm (markers) and target frequency power law attenuation (gray lines) for $\gamma = [1, 1.3, 1.6, 2]$.

Following the above procedure, the relaxation times τ_n and relaxation modulus η_n were optimized for different frequency power laws covering the range of that observed in tissues $\gamma = [1, 1.3, 1.6, 2]$. The attenuation coefficient α_0 was chosen for each power law to present an attenuation $\alpha = 1$ dB/cm/MHz$^\gamma$. The fitting was developed over the typical frequency range for medical ultrasound applications,

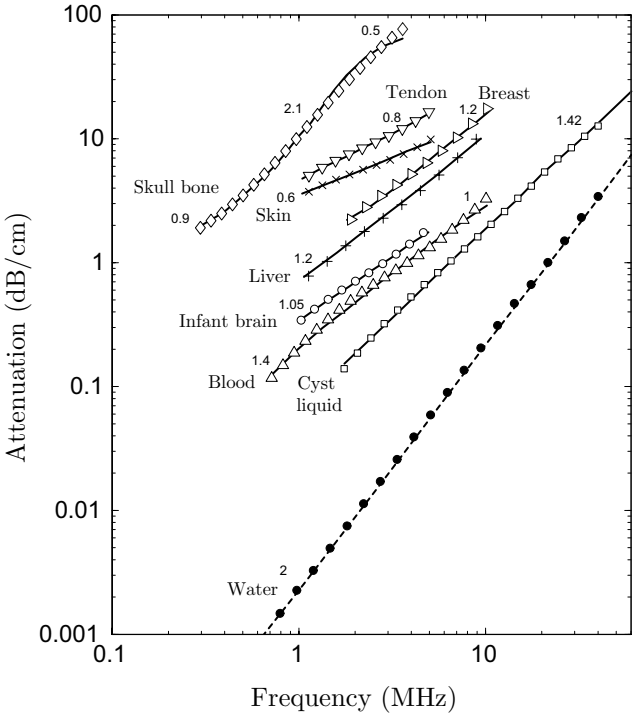


Figure 7.9: Experimental attenuation data for some tissues adapted from (Hill et al., 2004) (lines), and obtained by the numerical method (markers) by fitting the parameters of 2 relaxing processes. The numbers above the curves show the coefficient of the frequency power law γ for each frequency region (i.e. the slope of the curve).

i. e. 1 to 20 MHz for both attenuation and phase speed. The results for the attenuation and phase speed curves are plotted in Fig. 7.7 and Fig. 7.8, where the theoretical and the numerical predictions agree over the frequency range used for the fitting.

7.5.2 Fitting attenuation for tissue experimental data

Although a frequency power law dependence can describe the ultrasound attenuation over a finite frequency range, the attenuation data of some particular examples shows variation of the exponent over the entire frequency range (Hill et al., 2004). Thus, Fig. 7.9 shows experimental attenuation data curves for some tissues where the local slope of the power law changes over the measured frequency range. This behavior can be modeled by a sum of relaxation processes by optimizing the relaxation parameters as described above. Thus, the results show that most tissues

Table 7.1: Error of the optimized attenuation response relative to the experimental data for N relaxation processes.

Tissue	Power law (local slope)	$N = 1$ $\varepsilon(\%)$	$N = 2$ $\varepsilon(\%)$	$N = 3$ $\varepsilon(\%)$	$N = 4$ $\varepsilon(\%)$
Skin	$f^{0.6}$	6.67	0.167	0.136	0.120
Liver	$f^{1.2}$	7.62	0.517	0.404	0.165
Blood	$f^{1.4}$, f^{1}	8.34	0.349	0.330	0.310
Breast	$f^{0.9}$, $f^{1.2}$	5.20	0.216	0.209	0.205
Skull bone	$f^{0.9}$, $f^{2.1}$, $f^{0.5}$	10.60	10.54	8.628	5.189

with locally variable γ can be fitted by only a pair of relaxation processes, as the same way that for constant-slope frequency power law attenuation (Cleveland et al., 1996).

In this way, Table 7.1 shows the error of the numerical attenuation relative to the experimental data. The percent relative error was computed as

$$\varepsilon = \frac{100}{f_2 - f_1} \int_{f_1}^{f_2} \frac{|\alpha_e(f) - \alpha(f)|}{\alpha_e(f)} \, \mathrm{d}f, \tag{7.31}$$

where $\alpha_e(f)$ is the experimental attenuation data, f_1 and f_2 define the frequency range of the measurement.

As expected, the goodness of fit grows as the number of relaxation processes included increases. However, only two processes are enough to obtain relative errors below 1% for tissues with $\gamma < 2$. In the case of tissues where a local value of $\gamma > 2$ has been observed, the fitting procedure fails, like in the skull bone in the 2 MHz range (Hill et al., 2004). The maximum slope achieved by single relaxation and thermo-viscous losses is $\gamma = 2$ for any frequency, so a tissue showing that slope cannot be accurately modeled in this frequency region with the method proposed in this work. Another point of view of is from dispersion: Eq. (7.30 states that frequency power law medium with $2 < \gamma < 3$ presents standard dispersion (Waters et al., 2005), opposite to *anomalous* dispersion for media falling in the range $0 < \gamma < 2$. Therefore, the dispersion relation of media with $2 < \gamma < 3$ cannot be modeled by a sum of relaxation processes as long relaxation includes *anomalous* dispersion.

Using Kramers-Kronig relationships (O'Donnell et al., 1981), the variations of sound speed Δc can be predicted by the frequency dependent attenuation. Table 7.2 shows the variation of sound speed observed in the numerical solution over the fitted frequency range. The magnitude of these variations are of the order of magnitude of those measured experimentally in this frequency range, and the frequency dependence observed for the variation is roughly linear as observed in real

Table 7.2: Variation of sound speed (Δc) observed numerically for the modeled tissues by means of two relaxation processes and analytical using the Kramers-Kronig relations.

Tissue	Numerical Δc (m/s)	Analytical Δc (m/s)
Skull bone	80.737	70.720
Skin	10.148	2.460
Breast	2.323	2.455
Liver	3.118	2.339
Blood	0.865	0.907

tissue (Hill et al., 2004). As expected from the relations between dispersion and absorption (O'Donnell et al., 1981), the magnitude of the variation in sound speed increases as the total variation of the absorption increases for a given frequency range.

7.5.3 Nonlinear one-dimensional propagation in tissue-like media

Non-dispersive media

In order to study the convergence of the numerical calculations to an analytical solution of the model in the nonlinear regime, a medium with frequency squared dependence attenuation is implemented using the adequate relaxation times and relaxation modulus as explained above. The solution for the frequency squared absorption is compared with the analytical solution for a plane wave traveling through a thermo-viscous fluid proposed by Mendousse (Pierce, 1989):

$$\frac{p}{p_0} = \frac{\frac{4}{\Gamma}\sum_{n=1}^{\infty}(-1)^{n+1} I_n\left(\frac{\Gamma}{2}\right) n\mathrm{e}^{-n^2\sigma/\Gamma}\sin\left(n\omega t'\right)}{I_0\left(\frac{\Gamma}{2}\right) + 2\sum_{n=1}^{\infty}(-1)^{n} I_n\left(\frac{\Gamma}{2}\right) n\mathrm{e}^{-n^2\sigma/\Gamma}\cos\left(n\omega t'\right)} \tag{7.32}$$

where Γ is the Gol'dberg number, defined for power law media as $\Gamma = x_a/x_s$, with absorption length $x_a = 1/\alpha_0\omega^{\gamma}$, shock formation distance $x_s = 1/\beta\varepsilon k$ and normalized distance $\sigma = x/x_s$; with the parameter of nonlinearity $\beta = 1 + B/2A$ and the acoustic Mach number $\varepsilon = v/c_0$, with v is the source particle velocity and k the wavenumber.

Figure 7.11 (top) present the simulated waveforms at $\sigma = 1$ and $\sigma = 3$. The wave steepening due to nonlinear processes in the absence of dispersion are well resolved by the numerical method presented here. In order to study the accuracy of the algorithm, the amplitude of the first ten harmonics has been extracted for numerical and analytic solutions and plotted versus σ in Fig. 7.11 (bottom). The

observed relative error of the computational method decreases due to grid coarsening by a square law (i.e. the numerical scheme is second order accuracy). The magnitude of the error mainly depends on the number of elements per wavelength but, due to not ideal dispersion, also on the traveled propagated distance. Including the correction of dispersion by artificial relaxation, for a path length of 100 λ, a grid of 26 elements per wavelength was needed to obtain a relative error below 1 % for the third harmonic. Obviously, the relative error of the first and second harmonics will be always lower, i.e. the fundamental component error was 0.072 %.

In addition, the solution was compared also to the obtained by a k-space method applied to the constitutive relations by using the k-wave algorithm (Treeby et al., 2012). This method was selected due to the low numerical dispersion and the possibility of including frequency power law attenuation. The result of both computational methods and Eq. (7.32) agree over all the spectral components analyzed, showing convergence to the analytic solution.

Dispersive media

In the case of frequency power law attenuation media with $\gamma \approx 1$ no general analytic solution exist in nonlinear regime for monochromatic progressive waves. Thus, in order to study convergence in this regime, the proposed FDTD solution was compared with the solution obtained by k-space methods (Treeby et al., 2012). By using same physical and grid parameters in both methods, the solutions agrees for different power laws. Thus, Fig. 7.12 (top) shows the good agreement for the waveforms measured at $\sigma = 1$ and $\sigma = 3$ obtained for $\gamma = 1.6$, where the characteristic asymmetry of media with *anomalous* dispersion (e.g. relaxing, boundary layer effects) (Hamilton et al., 1998b) is observed: the shock front after the rarefaction phase is followed by a rounded positive compression profile. The spatial distribution for each harmonic is shown in Fig. 7.13 (bottom), where it is observed that the proposed FDTD solution with optimized attenuation and dispersion converges to the obtained by pseudo-spectral methods up to ten harmonics. As in the case of frequency squared media, grid refinement numerical tests have reported a second order accuracy of the FDTD method in nonlinear regime.

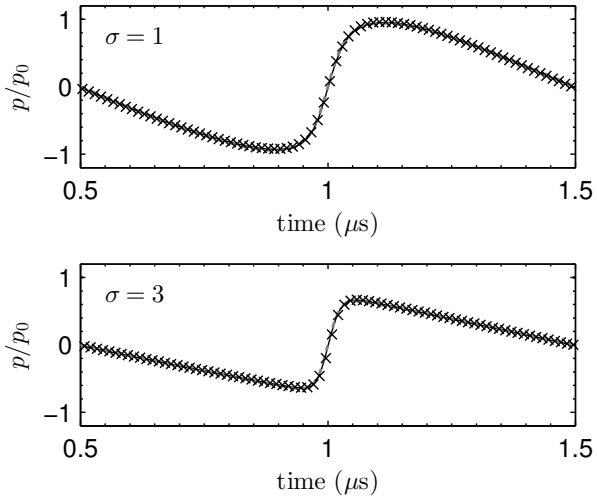


Figure 7.10: Waveforms for $\sigma = 1$ and $\sigma = 3$ in a media with frequency squared power law. Mendousse analytical solution (blue line), k-space numerical solution (gray line) and FDTD numerical solution (markers).

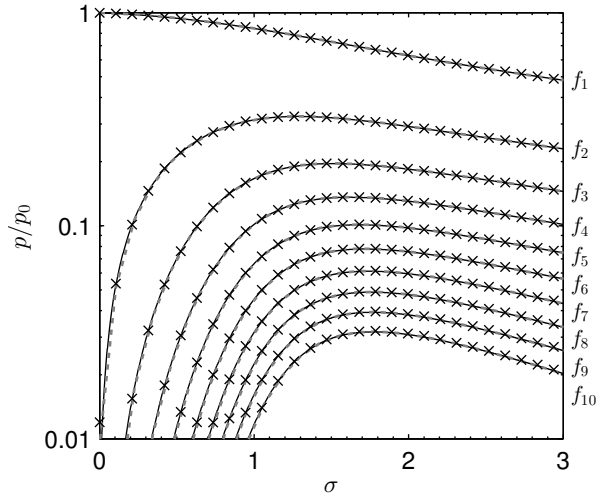


Figure 7.11: Spatial distribution of the first ten harmonics for $\gamma = 2$. Mendousse analytical solution (blue line), k-space numerical solution (gray line) and FDTD numerical solution (markers).

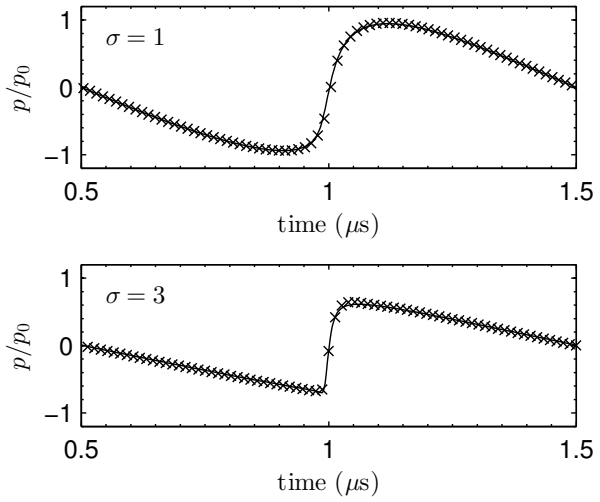


Figure 7.12: Waveforms for $\sigma = 1$ and $\sigma = 3$ in a media with frequency power law ($\gamma = 1.6$). k-space numerical solution (gray line) and FDTD numerical solution (markers).

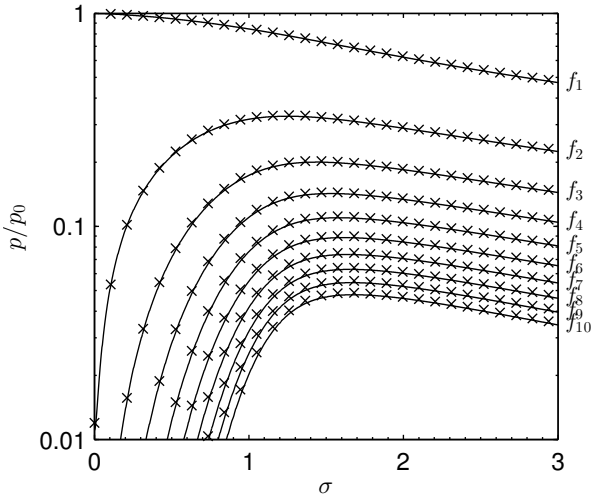


Figure 7.13: Spatial distribution of the first ten harmonics for $\gamma = 1.6$. k-space numerical solution (gray line) and FDTD numerical solution (markers).

7.5.4 Nonlinear propagation in tissue-like media including diffraction

Experimental validation

An experiment was designed to test the validity of the algorithm for intense beams in frequency power law attenuation media. The source was formed by a plane single element piezoceramic crystal (PZ 26, Ferroperm Piezoceramics, Denmark) mounted in a custom designed steel housing and a Polymethyl methacrylate (PMMA) focusing lens with aperture $A = 50$ mm and radius of curvature $R = 50$ mm. The source was driven with a sinusoidal pulse burst of frequency $f_0 = 1.112$ MHz and $n = 50$ cycles using a function generator (14 bits, 100 MS/s, model PXI5412, National Instruments) and a linear RF amplifier (ENI 1040L, 400W, 55dB, ENI, Rochester, NY). The pressure waveforms were acquired with a HNR 500 μm needle PVDF hydrophone (Onda Corp, CA), and a digitizer (64 MS/s, model PXI5620, National Instruments) were used. A three-axis micropositioning system (OWIS GmbH, Germany) was used to move the hydrophone in three orthogonal directions with an accuracy of 10 μm and a National Instruments PXI-Technology controller NI8176 was used to control all the devices. The amplitude frequency response of the hydrophone was compensated in post-processing but not in phase due to the absence of phase calibration for this equipment. A scheme of the measurement setup is shown in Fig. 7.14.

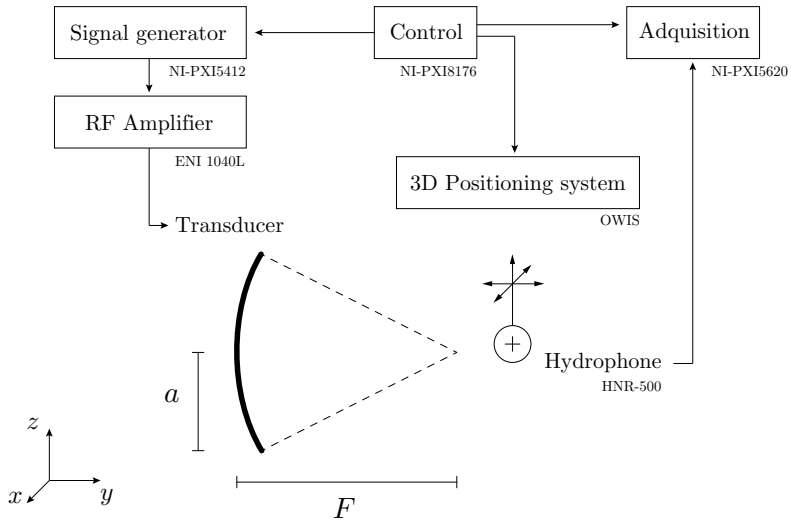


Figure 7.14: Scheme of the measurement system

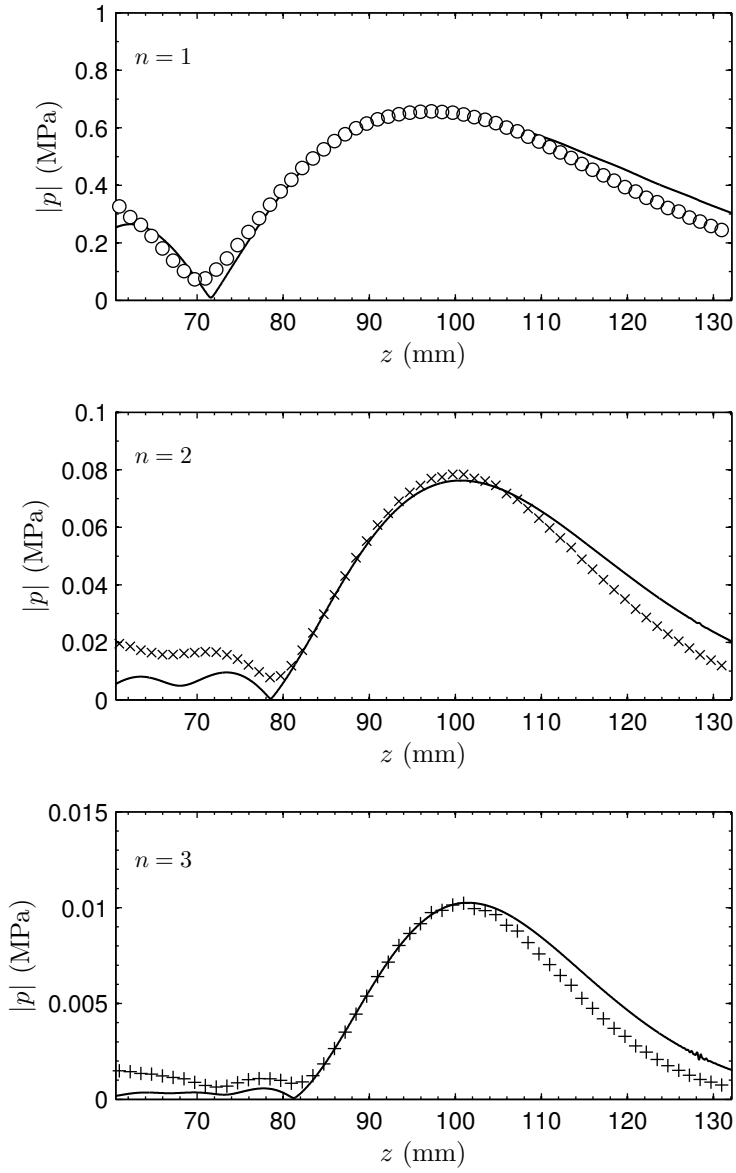


Figure 7.15: Spatial distribution of the fundamental (o), second ($\times$) and third ($+$) harmonics obtained by the numerical (continuous line) and experimental methods (markers) for a focused transducer immersed in castor oil.

The source was completely immersed in a castor oil tank ($350 \times 350 \times 350$ mm). We select this frequency power law attenuation media due to the low variability of its acoustic properties along existent literature (Liebler et al., 2004; Treeby et al., 2009). Using a sound speed inside the bulk of the lens $c_l = 2711$ m/s, and a sound speed of the castor oil of $c_0 = 1480$ m/s (at 26º C room temperature), the effective lens geometrical focal is estimated as $F = R/(1 - c_0/c_l) = 110.1$ mm, leading to a linear lossless gain of $G = 13.4$.

On the other hand, a nonlinear simulation including diffraction and frequency power law attenuation with same parameters was carried out in a workstation (20 cores Intel Xeon E5-2680 CPU, 2.8GHz with 256 GB RAM). The boundary conditions were implemented for a spherical focused ultrasound source. The castor oil parameters at 26º C room temperature (Treeby et al., 2009), were $c_0 = 1480$ m/s, $\rho_0 = 961$ kg/m^3, $\alpha = 0.4$ dB/cm/MHz$^\gamma$, $\gamma = 1.69$, $B/A = 12.0$. The grid parameters were $\Delta r = \Delta z = 29.6$ μm and $\Delta t = 13.6$ ns, leading to a CFL number $S = 0.95$ and $N_\lambda = 50$ elements per wavelength at fundamental frequency, note that this grid leads to $N_\lambda = 16$ for third harmonic.

The balance between nonlinear effects and power law attenuation can be estimated by using the Gol'dberg ratio, $\Gamma = x_a/x_s$ where x_s is the shock formation distance and x_a the media attenuation characteristic length. Thus, the amplitude of the source were selected to obtain a Gol'dberg ratio of $\Gamma = 0.25$ in order to let the frequency power law attenuation effects slightly dominate over nonlinear effects. On the other hand, the ratio between diffraction effects and nonlinear effects can be described by the so called Khokhlov number $N = x_d/x_s$, where $x_d = ka^2/2$ is the diffraction length and a source radius. For the proposed test a Khokhlov number of $N = 0.49$ was selected to let the nonlinear effect slightly dominate over diffraction effects. The selected excitation pressure amplitude was $p_0 = 87.7$ kPa.

The results are summarized in Fig. 7.15, where axial pressure distribution for the fundamental, second and third harmonic are presented. A good agreement is found between simulations and the experimental test. Only far to the focal point the amplitude there exist differences between computations and experiments, that can be caused by nonuniform vibration of the source (Canney et al., 2008), boundary effects of the PMMA lens, or miss-alignment of the source axis and micropositioning system orthogonal directions along the 100 mm axial measurement.

The maximum amplitudes of the first harmonic were $p_{e1} = 0.6539$ MPa for the experiment and $p_{n1} = 0.6576$ for the numeric. The second harmonic peak pressure was $p_{e2} = 78.368$ kPa and $p_{n2} = 76.272$ kPa, and the third harmonic peak pressure $p_{e3} = 10.146$ and $p_{n3} = 10.252$ kPa for the experimental and numeric respectively. The relative errors between numerical and experimental results are 0.56 % for the fundamental frequency, 2.67 % for the second harmonic and 1.04 % for the third. No error estimation was done for the peak pressure due to the absence of a phase calibration of the hydrophone.

Highly focused beam

In order to test the algorithm in the very high nonlinear regime with realistic tissue parameters a focused bowl of geometrical focal $F = 50$ mm and aperture $A = 50$ mm, driven at $f_0 = 1$ MHz was numerically tested. These parameters leads to a source gain $G = 26.5$ and a f-number= 1, showing that source is beyond the paraxial limit. The media consist in two layers. The first, where the source was located, was water at 20^o with parameters $c_1 = 1482$ m/s, $\rho_1 = 1000$ kg/m^3, $B/A_1 = 5$, $\alpha_1 = 2.17 \times 10^{-3}$ dB/cm MHz$^\gamma$, $\gamma_1 = 2$. At a distance $z_l = 0.7/F = 35$ mm, a layer of human liver tissue was placed, therefore the focal spot is located inside tissue at a depth of 15 mm. Liver tissue parameters (Hill et al., 2004) were $c_2 = 1597$, $\rho_2 = 1050$ kg/m^3, $B/A_2 = 7.9$, $\alpha_2 = .75$ dB/cm MHz$^\gamma$, $\gamma_2 = 1.5$. In this case, the numerical grid parameters were $\Delta r = \Delta z = 29.6$ μm and $\Delta t = 11.9$ ns, leading to a CFL number $S = 0.9$ and $N_\lambda = 50$ elements per wavelength at fundamental frequency ($N_\lambda = 16$ for third harmonic).

Figure 7.16 shows the spatial peak pressure profiles for different excitation amplitudes. Thus, in Fig. 7.16 (top) the pressure of the source was $p_0 = 0.18$ MPa, while in the bottom figure was increased to $p_0 = 0.94$ MPa. Thus, for the selected parameters, Fig. 7.16 (top) present results for $\Gamma = 0.16$ and $N = 0.55$, so the attenuation effects dominates over nonlinear effects and nonlinearity dominates over diffraction effects. In this way, low asymmetry is observed between the positive compression peak, p^+, and the minimum rarefaction pressure distribution, p^-. The measured waveform at $z = F$, shown in the inset of Fig. 7.16 (top), is weakly distorted. However, there exist differences between its normalized peak amplitude $p^+/p_0 = 25.7$ and $p^-/p_0 = 21.05$, and the source characteristic linear gain, $G = 26.5$. There are caused, in one hand by the attenuation effects, where the value of the lossy linear gain observed was $G_\alpha = p^+/p_0 = p^-/p_0 = 23.1$ measured at z=F, i.e. the amplitude at the focal was reduced to 87.2% of the lossless amplitude. On the other hand, the differences due to the asymmetry between compression and rarefaction cycles are caused by the combined effect of nonlinearity and focusing.

If source amplitude is increased to $p_0 = 0.94$ MPa, as shown in Fig. 7.16 (bottom), the ratio between attenuation and nonlinear effects is increased to $\Gamma = 0.79$. In this regime, nonlinear effects are almost of the same order of attenuation effects. On the other hand, increasing source amplitude while keeping same transducer parameters implies also the Khoklov number changes to $N = 0.11$, so the nonlinear effects clearly dominates over diffraction. In this regime, highly asymmetric pressure distribution is observed, where the values at focal point are $p^+ = 49.05$ MPa and $p^- = -14.91$ MPa.

Other typical nonlinear phenomena characteristic of high intensity focused sources can also be observed: formation of sharp shock front and its corresponding harmonic generation, or, as Fig. (7.17) shows, narrowing of the beam for p^+ and broadening for p^- pressure distributions. In addition, nonlinear focal shift,

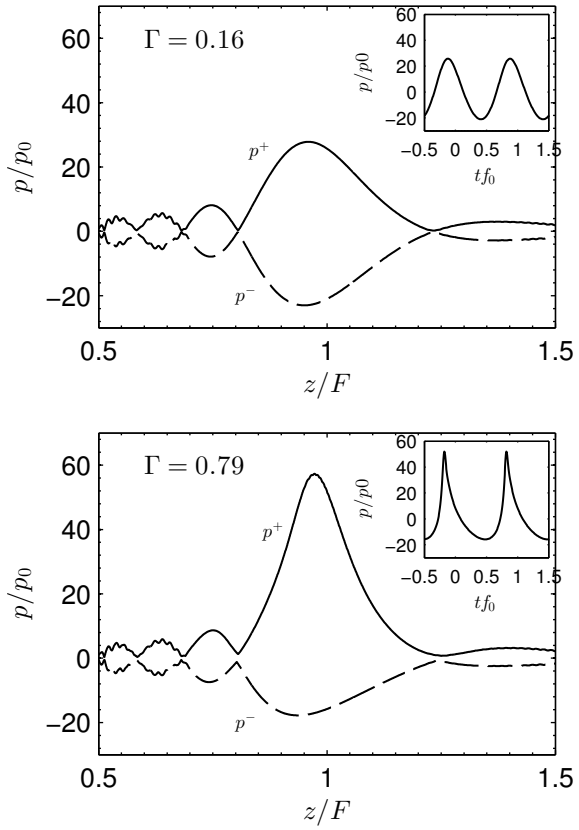


Figure 7.16: Axial spatial distribution of the peak compression (p^+) and minimum rarefaction (p^-) pressure for a focused transducer thought a liver tissue layer propagation. (Top) weakly nonlinear propagation ($\Gamma = 0.16$) and (bottom) strong nonlinear effects ($\Gamma = 0.79$). The insets show the waveforms recorded at the geometrical focal.

i.e. displacement of the peak pressure relative to the position of the liner peak pressure can be also predicted for tissue propagation. In the case of $\Gamma = 0.79$ the nonlinear focal shift was $\Delta F^+ = +1.05$ mm and $\Delta F^- = -1.03$ mm for the p^+ and p^- pressure distribution respectively.

7.6 Summary

A model for nonlinear acoustic waves in relaxing media is presented in a time-domain formulation which does not require convolutional operators. A numerical solution by means of finite-differences in time-domain have been obtained, showing that the theoretical attenuation and dispersion due to relaxation processes can be

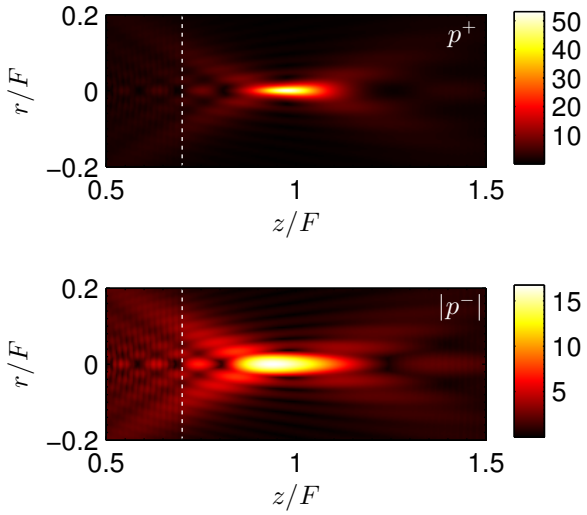


Figure 7.17: Spatial distribution of the peak compression (p^+) and minimum rarefaction (p^-) pressure for a focused transducer thought a liver tissue layer propagation (boundary marked with dashed line) for $\Gamma = 0.79$. Colorbars are in p/p_0 units.

achieved by the numerical method with accuracy. These result can be used to model typical relaxation process (e. g. the processes observed in air, associated to the molecules of oxygen and nitrogen, or in seawater, associated to the relaxation of boric acid and magnesium sulfate).

Moreover, a method for modeling a frequency power law on attenuation by means of multiple relaxation has been described. The proposed method can describe local variations of the exponent of the frequency power law, so an arbitrary attenuation curve in the range $0 < \gamma < 2$ can be modeled by means of the proper optimization of the relaxation coefficients. This feature of the presented method is an advantage when compared with most fractional derivatives methods, where the attenuation follows an exact but unique frequency power law over the entire frequency range. A broad range of human tissues have been modeled and the goodness of the fit using from two to four relaxation processes has been discussed.

Furthermore, a computational technique that exploits the *anomalous* dispersion of the relaxation processes is employed to mitigate the numerical dispersion of the finite-differences scheme. Thus, while phase speed is corrected by including artificial relaxation processes, its corresponding artificial attenuation is used to improve stability in the nonlinear regime. In this way, a smooth version of shock waves have been obtained and compared with analytic solutions. Furthermore, the validity of the algorithm including diffraction have been tested with experimental

measurements of a focused beam in castor oil.

Due to the model is developed from the constitutive relation for nonlinear acoustics, most wave phenomena is captured. As a difference from the one-way models the proposed model implicitly includes multiple wave direction, and, due to the Lagrangian density of acoustic energy is implicitly included in the computation, multiple scattering and strong resonance effects are accurately described. Moreover, unlike KZK and other parabolic approximations, the proposed model captures the diffraction exactly, so for simulation of acoustic beams the field is not approximated only to the beam axis, but also in the near field and far to the beam axis and thus high focusing devices can be simulated.

The code has shown to be particularly appropriate if the problem to simulate presents axisymmetry, because the constitutive relations for nonlinear acoustics are solved in a computational 2D domain, while standard k-space methods need to employ full 3D domains due to the poor convergence of the Fourier series at discontinuities ($r = 0$). This is the case, for example, of the focused transducer simulated in section 7.5.4, where a full 3D solution will require a huge computational resources and time. Finally, the particle velocity vector is solved implicitly by the code and can be used to estimate other relevant magnitudes as the full nonlinear intensity vector, the nonlinear radiation force field in the absorbing media or the acoustic streaming in frequency power law attenuation fluids.

References

Aanonsen, Sigurd Ivar, Tor Barkve, Jacqueline Naze Tjo, et al. (1984). "Distortion and harmonic generation in the nearfield of a finite amplitude sound beam". In: *J. Acoust. Soc. Am.* 75.3, pp. 749–768.

Albin, Nathan, Oscar P. Bruno, Theresa Y. Cheung, and Robin O. Cleveland (2012). "Fourier continuation methods for high-fidelity simulation of nonlinear acoustic beams". In: *J. Acoust. Soc. Am.* 132.4, pp. 2371–2387.

Blackstock, David T (1985). "Generalized Burgers equation for plane waves". In: *J. Acoust. Soc. Am.* 77.6, pp. 2050–2053.

Botteldooren, D. (1996). "Numerical model for moderately nonlinear sound propagation in three-dimensional structures". In: *J. Acoust. Soc. Am.* 100.3, pp. 1357–1367.

Canney, Michael S, Michael R Bailey, Lawrence A Crum, Vera A Khokhlova, and Oleg A Sapozhnikov (2008). "Acoustic characterization of high intensity focused ultrasound fields: A combined measurement and modeling approach". In: *The Journal of the Acoustical Society of America* 124.4, pp. 2406–2420.

Caputo, M. (1967). "Linear models of dissipation whose Q is almost frequency independent II". In: *Geophys. J. R. Astron. Soc.* 13, pp. 529–539.

Carstensen, EL, WK Law, ND McKay, and TG Muir (1980). "Demonstration of nonlinear acoustical effects at biomedical frequencies and intensities". In: *Ultrasound Med. Biol.* 6.4, pp. 359–368.

Chen, W and S Holm (2003). "Modified Szabos wave equation models for lossy media obeying frequency power law". In: *J. Acoust. Soc. Am.* 114.5, pp. 2570–2574.

Chen, W and S Holm (2004). "Fractional Laplacian time-space models for linear and nonlinear lossy media exhibiting arbitrary frequency power-law dependency". In: *J. Acoust. Soc. Am.* 115.4, pp. 1424–1430.

Christopher, P Ted and Kevin J Parker (1991). "New approaches to nonlinear diffractive field propagation". In: *J. Acoust. Soc. Am.* 90.1, pp. 488–499.

Cleveland, Robin O, Mark F Hamilton, and David T Blackstock (1996). "Time-domain modeling of finite-amplitude sound in relaxing fluids". In: *J. Acoust. Soc. Am.* 99.6, pp. 3312–3318.

Demi, L, KWA Van Dongen, and MD Verweij (2011). "A contrast source method for nonlinear acoustic wave fields in media with spatially inhomogeneous attenuation". In: *J. Acoust. Soc. Am.* 129.3, pp. 1221–1230.

Duck, Francis A. (1990). *Physical Properties of Tissue: A Comprehensive Reference Book.* San Diego, CA 92101, USA: Academic Press Inc. San Diego, p. 346.

Ginter, Siegfried, Marko Liebler, Eckard Steiger, Thomas Dreyer, and Rainer E. Riedlinger (2002). "Full-wave modeling of therapeutic ultrasound: nonlinear ultrasound propagation in ideal fluids." In: *J. Acoust. Soc. Am.* 111.5, pp. 2049–2059.

Goss, S. A., L. A. Frizzell, and F. Dunn (1979). "Ultrasonic absorption and attenuation in mammalian tissues". In: *Ultrasound Med. Biol.* 5 (2), pp. 181–186.

Hallaj, Ibrahim M and Robin O Cleveland (1999). "FDTD simulation of finite-amplitude pressure and temperature fields for biomedical ultrasound". In: *J. Acoust. Soc. Am.* 105.5, pp. L7–L12.

Hallaj, Ibrahim M, Robin O Cleveland, and Kullervo Hynynen (2001). "Simulations of the thermo-acoustic lens effect during focused ultrasound surgery". In: *The Journal of the Acoustical Society of America* 109.5, pp. 2245–2253.

Hamilton, M.F. and D.T. Blackstock (1998b). *Nonlinear Acoustics.* Academic Press.

Hill, C.R., J. C. Bamber, and G.R. ter Haar (2004). *Physical Principles of Medical Ultrasonics, 2nd ed.* John Wiley & Sons Ltd, Chichester, England.

Huijssen, Jacobus and Martin D Verweij (2010). "An iterative method for the computation of nonlinear, wide-angle, pulsed acoustic fields of medical diagnostic transducers". In: *J. Acoust. Soc. Am.* 127.1, pp. 33–44.

Jing, Yuan and Robin O Cleveland (2007). "Modeling the propagation of nonlinear three-dimensional acoustic beams in inhomogeneous media". In: *J. Acoust. Soc. Am.* 122.3, pp. 1352–1364.

Jing, Yun, Du Shen, and Greg T Clement (2011). "Verification of the Westervelt equation for focused transducers". In: *Ultrasonics, Ferroelectrics and Frequency Control, IEEE Transactions on* 58.5, pp. 1097–1101.

Jing, Yun, Tianren Wang, and Greg T Clement (2012). "A k-space method for moderately nonlinear wave propagation". In: *Ultrasonics, Ferroelectrics and Frequency Control, IEEE Transactions on* 59.8, pp. 1664–1673.

Jongen, HAH, JM Thijssen, M Van Den Aarssen, and WA Verhoef (1986). "A general model for the absorption of ultrasound by biological tissues and experimental verification". In: *The Journal of the Acoustical Society of America* 79.2, pp. 535–540.

Kellya, James F. and Robert J. McGough (2009). "Fractal ladder models and power law wave equations". In: *J. Acoust. Soc. Am.* 126.4, pp. 2072–2081.

Khokhlova, VA, AE Ponomarev, MA Averkiou, and LA Crum (2006). "Nonlinear pulsed ultrasound beams radiated by rectangular focused diagnostic transducers". In: *Acoustical Physics* 52.4, pp. 481–489.

Lee, Yang-Sub and Mark F Hamilton (1995). "Time-domain modeling of pulsed finite-amplitude sound beams". In: *J. Acoust. Soc. Am.* 97.2, pp. 906–917.

LeVeque, R.J. (1992). *Numerical Methods for Conservation Laws.* Ed. by Lectures in Mathematics. ETH Zurich. Birkhauser Verlag.

Liebler, Marko, Siegfried Ginter, Thomas Dreyer, and Rainer E. Riedlinger (2004). "Full wave modeling of therapeutic ultrasound: efficient time-domain implementation of the frequency power-law attenuation." In: *J. Acoust. Soc. Am.* 116.5, pp. 2742–2750.

Liu, Q. H. (1999). "Perfectly matched layers for elastic waves in cylindrical and spherical coordinates". In: *J. Acoust. Soc. Am.* 105.4, pp. 2075–2084.

Liu, Qing-Huo and Jianping Tao (1997). "The perfectly matched layer for acoustic waves in absorptive media". In: *J. Acoust. Soc. Am.* 102.4, pp. 2072–2082.

Lobanova, E. G., S. V. Lobanov, and V. A. Khokhlova (2014). "Counterpropagation of waves with shock fronts in a nonlinear tissue-like medium". In: *Acoustical Physics* 60.4, pp. 387–397.

Manry, Charles W and Shira L Broschat (1996). "FDTD simulations for ultrasound propagation in a 2-D breast model". In: *Ultrasonic imaging* 18.1, pp. 25–34.

Mast, T Douglas, Laura M Hinkelman, Michael J Orr, Victor W Sparrow, and Robert C Waag (1997). "Simulation of ultrasonic pulse propagation through the abdominal wall". In: *J. Acoust. Soc. Am.* 102.2, pp. 1177–1190.

Mast, T Douglas, Laurent P Souriau, D-LD Liu, Makoto Tabei, Adrian I Nachman, and Robert C Waag (2001). "A k-space method for large-scale models of wave propagation in tissue". In: *Ultrasonics, Ferroelectrics and Frequency Control, IEEE Transactions on* 48.2, pp. 341–354.

Muir, TG and EL Carstensen (1980). "Prediction of nonlinear acoustic effects at biomedical frequencies and intensities". In: *Ultrasound Med. Biol.* 6.4, pp. 345–357.

Nachman, Adrian I, James F Smith III, and Robert C Waag (1990). "An equation for acoustic propagation in inhomogeneous media with relaxation losses". In: *J. Acoust. Soc. Am.* 88, p. 1584.

Nasholm, Sven Peter and Sverre Holm (2011). "Linking multiple relaxation, power-law attenuation, and fractional wave equations". In: *J. Acoust. Soc. Am.* 130.5, pp. 3038–3045.

Naugolnykh, K. and L. Ostrovsky (1998). *Nonlinear Wave Processes in Acoustics*. Cambridge Texts in Applied Mathematics. Cambridge University Press.

Ochmann, Martin and Sergey Makarov (1993). "Representation of the absorption of nonlinear waves by fractional derivatives". In: *The Journal of the Acoustical Society of America* 94.6, pp. 3392–3399.

O'Donnell, M., E. T. Jaynes, and J. G. Miller (1981). "Kramers–Kronig relationship between ultrasonic attenuation and phase velocity". In: *J. Acoust. Soc. Am.* 69.3, pp. 696–701.

Pierce, A.D. (1989). *Acoustics: An Introduction to Its Physical Principles and Applications*. Acoustical Society of America.

Pinton, Gianmarco F, Jeremy Dahl, Stephen Rosenzweig, and Gregg E Trahey (2009). "A heterogeneous nonlinear attenuating full-wave model of ultrasound". In: *Ultrasonics, Ferroelectrics and Frequency Control, IEEE Transactions on* 56.3, pp. 474–488.

Prieur, Fabrice and Sverre Holm (2011). "Nonlinear acoustic wave equations with fractional loss operators". In: *J. Acoust. Soc. Am.* 130.3, pp. 1125–1132.

Rudenko, O.V. and S.I. Soluian (1977). *Theoretical foundations of nonlinear acoustics*. Studies in Soviet science. New York, NY 10011, USA: Consultants Bureau, p. 274.

Shahbazi, Khosro, Nathan Albin, Oscar P. Bruno, and Jan S. Hesthaven (2011). "Multi-domain Fourier-continuation/WENO hybrid solver for conservation laws". In: *J. Comput. Phys.* 230.24, pp. 8779 –8796.

Soneson, Joshua E and Matthew R Myers (2007). "Gaussian representation of high-intensity focused ultrasound beams". In: *The Journal of the Acoustical Society of America* 122.5, pp. 2526–2531.

Sparrow, Victor W and Richard Raspet (1991). "A numerical method for general finite amplitude wave propagation in two dimensions and its application to spark pulses". In: *J. Acoust. Soc. Am.* 90.5, pp. 2683–2691.

Szabo, Thomas L (1994). "Time domain wave equations for lossy media obeying a frequency power law". In: *J. Acoust. Soc. Am.* 96.1, pp. 491–500.

Tavakkoli, Jahangir, Dominique Cathignol, Rémi Souchon, and Oleg A Sapozhnikov (1998). "Modeling of pulsed finite-amplitude focused sound beams in time domain". In: *The Journal of the Acoustical Society of America* 104.4, pp. 2061–2072.

Treeby, Bradley E, Benjamin T Cox, Edward Z Zhang, Sarah K Patch, and Paul C Beard (2009). "Measurement of broadband temperature-dependent ultrasonic attenuation and dispersion using photoacoustics". In: *Ultrasonics, Ferroelectrics, and Frequency Control, IEEE Transactions on* 56.8, pp. 1666–1676.

Treeby, Bradley E and BT Cox (2010). "Modeling power law absorption and dispersion for acoustic propagation using the fractional Laplacian". In: *J. Acoust. Soc. Am.* 127.5, pp. 2741–2748.

Treeby, Bradley E, Jiri Jaros, Alistair P Rendell, and BT Cox (2012). "Modeling nonlinear ultrasound propagation in heterogeneous media with power law absorption using a k-space pseudospectral method". In: *J. Acoust. Soc. Am.* 131.6, pp. 4324–4336.

Varslot, Trond and Gunnar Taraldsen (2005). "Computer simulation of forward wave propagation in soft tissue". In: *Ultrasonics, Ferroelectrics and Frequency Control, IEEE Transactions on* 52.9, pp. 1473–1482.

Verweij, Martin D, Libertario Demi, and Koen WA van Dongen (2013). "Computation of nonlinear ultrasound fields using a linearized contrast source method". In: *J. Acoust. Soc. Am.* 134.2, pp. 1442–1453.

Waters, Kendall R, Joel Mobley, and James G Miller (2005). "Causality-imposed (Kramers-Kronig) relationships between attenuation and dispersion". In: *Ultrasonics, Ferroelectrics and Frequency Control, IEEE Transactions on* 52.5, pp. 822–823.

Wismer, M. G. (2006). "Finite element analysis of broadband acoustic pulses through inhomogeneous media with power law attenuation". In: *J. Acoust. Soc. Am.* 120, pp. 3493–3502.

Wismer, Margaret G and Reinhold Ludwig (1995). "An explicit numerical time domain formulation to simulate pulsed pressure waves in viscous fluids exhibiting arbitrary frequency power law attenuation". In: *Ultrasonics, Ferroelectrics and Frequency Control, IEEE Transactions on* 42.6, pp. 1040–1049.

Yang, Xinmai and Robin O Cleveland (2005). "Time domain simulation of nonlinear acoustic beams generated by rectangular pistons with application to harmonic imaging". In: *J. Acoust. Soc. Am.* 117.1, pp. 113–123.

Yuan, Xiaojuen, D. Borup, J. Wiskin, M. Berggren, and S. A. Johnson (1999). "Simulation of acoustic wave propagation in dispersive media with relaxation losses by using FDTD method with PML absorbing boundary condition". In: *IEEE Transactions on Ultrasonics, Ferroelectrics, and Frequency Control* 46.1, pp. 14–23.

Yuldashev, PV and VA Khokhlova (2011). "Simulation of three-dimensional nonlinear fields of ultrasound therapeutic arrays". In: *Acoustical physics* 57.3, pp. 334–343.

Zemp, Roger J, Jahangir Tavakkoli, and Richard SC Cobbold (2003). "Modeling of nonlinear ultrasound propagation in tissue from array transducers". In: *J. Acoust. Soc. Am.* 113.1, pp. 139–152.

Publications

The contents of this chapter have been presented in the following publications:

Journal papers

- **Jiménez, N.**; Camarena, F.; Redondo, J.; Sánchez-Morcillo, V.; Hou Y. and Konofagou E. E. "Time-domain simulation of ultrasound propagation in tissue-like medium based on the resolution of the nonlinear acoustic constitutive relations". *The Journal of Acoustical Society of America*, *In preparation.*

Conference proceedings

- **Jiménez, N.**, F. Camarena, V. Sanchez-Morcillo, J. Redondo and E.E. Konofagou. "Time-domain simulation of constitutive relations for nonlinear acoustics including relaxation for frequency power law attenuation media modelling". *ISNA 2015,*

International Symposium of Nonlinear Acoustics. June 29th - July 3rd 2015, Lyon, France (2015).

- **Jiménez, N.**; Redondo, J.; Sánchez-Morcillo, V. and Camarena, F. "Nonlinear ultrasound simulations including complex frequency dependent attenuation". *43rd Annual UIA Symposium*, Madrid, Spain. 23 - 25 April. *Physics Procedia*, Volume 63, 2015, Pages 108-113, (2014)
- **Jiménez, N.**; Redondo, J.; Sanchez-Morcillo, V. and Camarena, F. "Ondas acústicas de amplitud finita en medios con relajación: aplicación a la modelización de tejidos biológicos". *44º Tecniacústica'13*, Valladolid, October, 1632-1637 (2013)

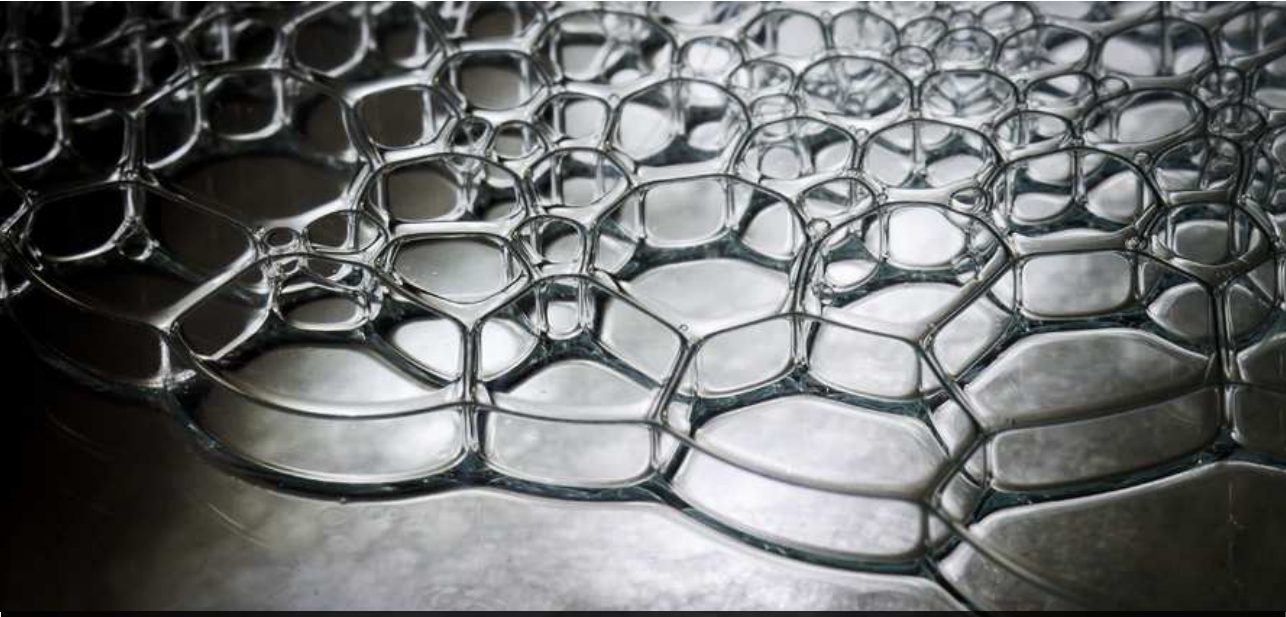
And the numerical method method have been applied for obtaining the following results

Journal papers

- **Jiménez, N.**; Redondo, J.; Sanchez-Morcillo, V. and Camarena, F. "Numerical Study of Nonlinear, Transcranial Focused Ultrasound Wave Propagation for Blood-Brain Barrier Opening". *IEEE Ultrasonics, Ferroelectrics and Frequency Control Society*, *In preparation.*
- **Jiménez, N.**; Marquet, F.; Camarena, F.; Konofagou, E. E.; Redondo, J.; Roig, B. and Picó, R. "Estudio de la propagación no lineal de haces de ultrasonidos focalizados a través del cráneo para la apertura de la barrera hematoencefálica". *Revista de Acústica*, 43, 5-11 (2012)

Conference proceedings

- Ordoñez-Cebrián, P; **Jiménez, N.**; Espinosa, V.; Puig-Pons, V. and Soliveres-González, E. "Efficiency of parametric ultrasound generation in relaxing media for very shallow-water echo sounders". *43rd Annual UIA Symposium.* Madrid, Spain. 23-25 April, (2014)
- Iglesias, P. C.; **Jiménez, N.**; Konofagou, E.; Camarena, F. and Redondo, J. "Transcranial Propagation with an Ultrasonic Mono-Element Focused Transducer". *43rd Annual UIA Symposium*, Madrid, Spain. 23-25 April. *Physics Procedia* Volume 63, 2015, Pages 103-107, (2014)
- Iglesias, P. C.; **Jimenez, N.**; Redondo, J.; Konofagou, E. E. and Camarena, F. "Parametric study of transcranial focused ultrasound propagation for blood–brain barrier opening". *European Symposium on Ultrasonic Characterization of Bone*. Granada, 7-10 May, (2013)
- **Jiménez, N.**; Roig, B.; Redondo, J.; Pico, R.; Marquet, F.; Konofagou, E. E. and Camarena, F. "Numerical study of nonlinear, transcranial focused ultrasound wave propagation for blood-brain barrier (BBB) opening". *ISTU 2011: International Society for Therapeutic Ultrasound Symposium*, New York, EEUU, (2011)



Chapter 8

Nonlinear Plane Waves in Frequency Power Law Attenuation Media

Abstract

In this chapter we revise fundamental aspects of nonlinear acoustic plane wave propagation through frequency power law attenuation media, with special focusing in the implications for finite amplitude ultrasound in biological media. The basic relationships between nonlinearity, absorption and dispersion are explored in detail, among with its implications for soft-tissue modeling in biomedical ultrasound applications. A derivation of simple expressions for quantify the role of the exponent of the power law in the balance between nonlinearity, dispersion and attenuation is presented. Detailed numerical calculations of the harmonic generation are also provided, where the efficiency in the harmonic generation and its relation with the weak frequency power law dispersion is studied.

8.1 Introduction

When modeling longitudinal acoustic wave propagation in biological soft-tissue media it is critical to account for the correct attenuation and phase speed. When dealing with linear monochromatic propagation, the values of media attenuation and phase speed for a given frequency can be explicitly included in the model equations from those obtained from experimental tests. A common practice is to adopt a sound speed value from the experimentally measured phase speed as $c_0 = c_p(\omega_0)$, and to match a value for the fluid viscosity, μ, that match the attenuation value at the desired frequency. However, if finite amplitude propagation is considered, the attenuation and phase velocity of each spectral component must be explicitly included in the model. In the case of biological media, where frequency power law attenuation is experimentally observed, there it is impossible to model these losses with only viscosity as long viscous losses present a frequency squared dependent attenuation and no dispersion. Thus, the inclusion of a causal-time domain operator that models frequency power law attenuation is necessary to accurately model the losses of each spectral component. Moreover, the inclusion of a frequency power law leads to the inevitable inclusion of dispersion that must be accurately modeled. Thus, for a frequency dependent attenuation in the form

$$\alpha(\omega) = \alpha_0 \omega^{\gamma}, \tag{8.1}$$

and by applying the Kramers-Kronig relationships (O'Donnell et al., 1981), the frequency dependent phase speed can be obtained as (Waters et al., 2005):

$$\frac{1}{c_p\left(\omega\right)} = \frac{1}{c_0} + \alpha_0 \tan\left(\frac{\pi\gamma}{2}\right)\left(|\omega|^{\gamma-1} - |\omega_0|^{\gamma-1}\right). \tag{8.2}$$

This expression is valid in the range $0 < \gamma < 3$ with $\gamma \neq 1$ and includes causality. In the limit $\gamma \to 1$ Eq. 8.2 reduces to

$$\left.\frac{1}{c_p\left(\omega\right)}\right|_{\gamma=1} = \frac{1}{c_0} - \frac{2}{\pi}\alpha_0 \log\left|\frac{\omega}{\omega_0}\right|. \tag{8.3}$$

On the other hand, the complex wave number $\tilde{k}$ can be written as

$$\tilde{k}\left(\omega\right) = \frac{\omega}{c_p\left(\omega\right)} - i\alpha\left(\omega\right), \tag{8.4}$$

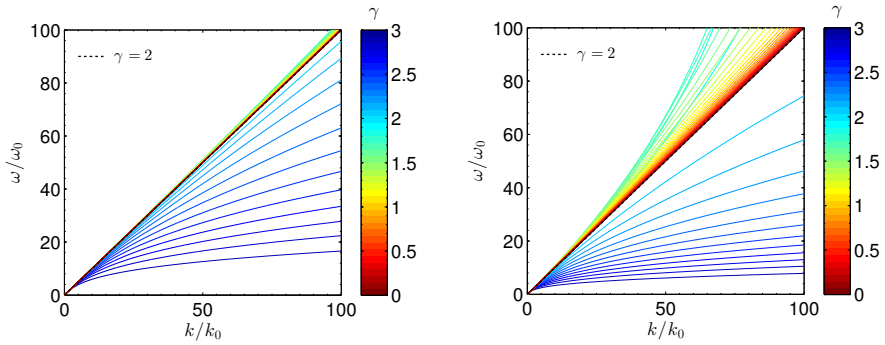


Figure 8.1: Dispersion relations for different frequency power laws for (a) $\alpha_0 = 10$ dB/cm and (b) $\alpha_0 = 1$ dB/cm measured at 1 MHz.

where $\mathrm{Im}(\tilde{k})$ is defined by the frequency power law attenuation and $\mathrm{Re}(\tilde{k})$ defines the phase speed. Combining Eq. 8.2, 8.1 and 8.4 the dispersion relations for a frequency power law media read

$$\tilde{k}\left(\omega\right) = \frac{\omega}{c_0} + \alpha_0 \omega \tan\left(\frac{\pi\gamma}{2}\right)\left(\left|\omega\right|^{\gamma-1} - \left|\omega_0\right|^{\gamma-1}\right) - i\alpha_0\omega^{\gamma} \tag{8.5}$$

for $0 < \gamma < 1$ and $1 < \gamma < 3$, and

$$\tilde{k}\left(\omega\right)\Big|_{\gamma=1} = \frac{\omega}{c_0} - \frac{2\alpha_0\omega}{\pi}\log\left|\frac{\omega}{\omega_0}\right| - i\alpha_0\omega \tag{8.6}$$

for $\gamma = 1$.

Thus, as shown in Fig. 8.1, the dispersion modeled by a frequency power law shows three different behavior depending on the power law exponent. First, for frequency independent losses, $\gamma = 0$, the media exhibit no dispersion as long $c_p = c_0$. This behavior is equivalent to the other simple physical attenuation models, e.g. the damped pendulum. On the other hand, this dispersionless regime is achieved also for $\gamma = 2$, as it is observed in acoustics for bulk thermo-viscous losses in pure water. Second, for $0 < \gamma < 2$ the real part of the wavenumber reduces in magnitude as long the frequency increases, so phase speed is increased in the higher frequency range, leading to the so called "anomalous dispersion" (Hill et al., 2004) (e.g. as observed also in water capillary waves). Finally, for media obeying frequency power law attenuation with $2 < \gamma < 3$ the phase speed decreases with increasing frequency, so "normal" dispersion is achieved as observed in other common physical systems as water surface gravity waves.

The frequency power law attenuation obtained for a soft-tissue media with an attenuation of 1 dB/cm and for 10 dB/cm measured at 1 MHz is shown in

Fig. 8.2. In the same way, Fig. 8.3 shows the frequency dependent phase speed from Eq. (8.2, 8.3), where for a frequency range from 0.1 to 10 MHz variations of about ±9 m/s are obtained in the case of 1 dB/cm at 1 MHz, and ≈ ±90 m/s for the case of 10 dB/cm for a linear power law. Thus, the magnitude of the dispersion of the system increases linearly with the attenuation magnitude. This behavior is in agreement with dispersion measurements in weakly (Szabo, 1995; Waters et al., 2000) and strongly (Fry et al., 1978) lossy media obeying frequency power law attenuation, and shows the importance of modeling correctly not only the attenuation but the dispersion when dealing with high damped media as biological tissues.

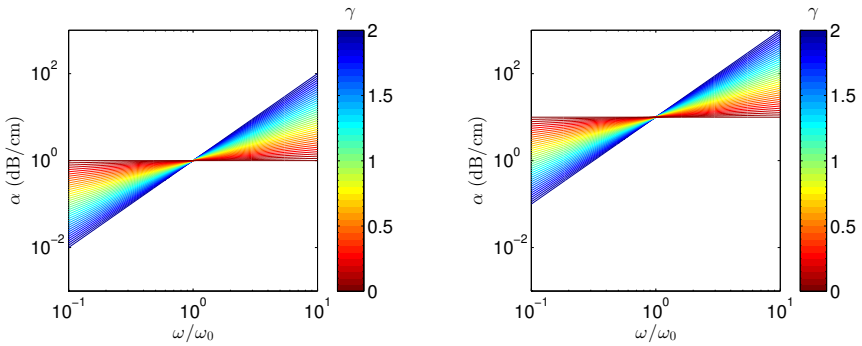


Figure 8.2: Frequency dependent attenuation obtained for different frequency power laws for (a) $\alpha_0 = 10$ dB/cm and (b) $\alpha_0 = 1$ dB/cm measured at 1 MHz.

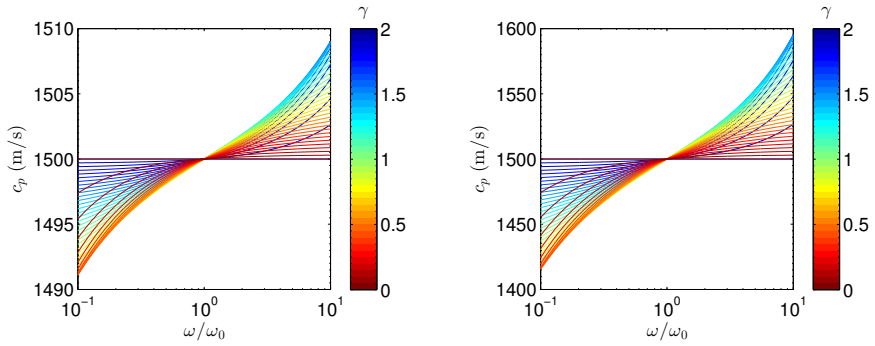


Figure 8.3: Phase velocity obtained for different frequency power laws for (a) $\alpha_0 = 20$ dB/cm and (b) $\alpha_0 = 2$ measured at 1 MHz.

8.2 Nonlinear coherence length

As introduced in Chapter 2, the coherence length magnitude is very helpfully in quantifying the nonlinear acoustic effects in dispersive media. Thus, the efficiency of energy transfer from fundamental to second harmonic component is dependent on the phase matching condition:

$$k\left(2\omega\right) = 2k\left(\omega\right). \tag{8.7}$$

In general, for dispersive media this condition is not fulfilled, so the second harmonic characteristic linear growth develops the well known beating effect (Rudenko et al., 1977), where the beating spatial frequency for the second harmonic is

$$\Delta k_2\left(\omega\right) = \left|2k\left(\omega\right) - k\left(2\omega\right)\right| \tag{8.8}$$

and the coherence length for the second harmonic is defined as

$$x_c\left(\omega\right) = \frac{\pi}{\Delta k_2\left(\omega\right)}. \tag{8.9}$$

In the case study, i.e. in frequency power law attenuation media, using Eqs. (8.5, 8.6), Eq. (8.8) reduces to

$$\Delta k_2\left(\omega\right) = \left(2^\gamma - 2\right)\alpha_0\omega^\gamma \tan\left(\frac{\pi\gamma}{2}\right) \tag{8.10}$$

for $0 < \gamma < 3$ with $\gamma \neq 1$, and

$$\Delta k_2\left(\omega\right)\big|_{\gamma=1} = -\frac{4\log\left(2\right)\alpha_0\omega^\gamma}{\pi} \tag{8.11}$$

for $\gamma = 1$. Then, combining Eq. (8.9) and Eq. (8.10), the characteristic nonlinear coherence length (for second harmonic) can be calculated as

$$x_c\left(\omega\right) = \frac{\pi\cot\left(\frac{\pi\gamma}{2}\right)}{\left(2^\gamma - 2\right)\alpha_0\omega^\gamma} \tag{8.12}$$

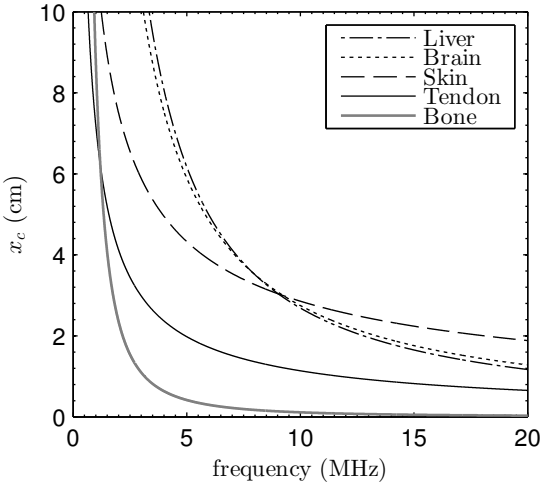


Figure 8.4: Coherence length as a function of frequency for a variety of tissues, where it has been assumed the following power laws: α_{Liver} =0.7 dB/cm/MHz$^{1.2}$, α_{Brain} =0.87 dB/cm/MHz$^{1.1}$, α_{Skin} =3.6 dB/cm/MHz$^{0.6}$, α_{Tendon} =4.77 dB/cm/MHz$^{0.8}$, α_{Bone} =10.5 dB/cm/MHz$^{1.89}$. Typical values extracted from Ref. Hill et al. (2004).

for $0 < \gamma < 3$ and $\gamma \neq 1$, and

$$x_c(\omega)|_{\gamma=1} = \frac{\pi^2}{4\log(2)\,\alpha_0\omega} \tag{8.13}$$

for $\gamma = 1$. It is worth noting here that the coherence length, x_c, is inversely proportional to attenuation magnitude. In this way, in frequency power law attenuation media with strong attenuation values and $\gamma \approx 1$, e.g. in bones, tendons(Fry et al., 1978) where strong dispersion is observed, and also for $\gamma \approx 3$, the efficiency of nonlinear harmonic generation is expected to be modified due to phase mismatching. The frequency dependence for different power laws of real tissues is shown in Fig. 8.4. Here, we show that the magnitude of coherence length is on the order of the size of the internal structures of the human body for ultrasound applications, i.e. $x \lessapprox 10$ cm. Thus, dispersion effects, in addition to attenuation and nonlinear effects can also be important in the nonlinear full solution. However, in order to evaluate the relevance of each effect in the full-wave propagation (attenuation, dispersion and nonlinearity), we shall define the ratio of attenuation to dispersion effects.

Thus, the amplitude of each harmonic will be damped due to the increase in attenuation, following the corresponding power law. Thus, we shall define the second harmonic characteristic attenuation distance for the frequency power law

attenuation media as

$$x_a = \frac{1}{\alpha_0 \omega^\gamma}. \tag{8.14}$$

In this way, using Eq. (8.12, 8.14) we define the quantity N_c as the ratio of attenuation and dispersion effects for power law media as

$$N_c = \frac{x_c}{x_a} = \left| \frac{\pi \cot\left(\frac{\gamma\pi}{2}\right)}{2^\gamma - 2} \right|. \tag{8.15}$$

In the limit of $\gamma \to 1$ Eq. (8.15) reduces to

$$N_c = \frac{\pi^2}{4 \log 2}. \tag{8.16}$$

One important remark is the ratio of attenuation to dispersion effects in a frequency power law media is frequency independent: both, the amount of attenuation and second harmonic phase mismatching magnitude are proportional to the quantity $\alpha_0 \omega^\gamma$. Furthermore, an increase in the attenuation coefficient, α_0, will increase in equal magnitude dispersion and attenuation effects. In this way, as Eq. (8.15) shows, the balance between attenuation and dispersion only depends on the exponent of the frequency power law media.

Figure 8.5 shows the ratio N_c for different power laws. For frequency power laws of $0 < \gamma < 2$, i.e. those that model biological media, the ratio fall in the range $3.43 \lessapprox N_c < \infty$. In this way, $N_c \to \infty$ for dispersionless media, i.e. for even exponent power $\gamma = 0$ and $\gamma = 2$. The higher dispersive regime is obtained for nearly linear frequency dependent absorption, where a local minimum is numerically found at

$$\gamma \approx 1.2053. \tag{8.17}$$

In the range $0.5 < \gamma < 1.5$, the ratio of attenuation to dispersion effects, N_c, present variations of +44% from the minimum value ($N_c = 3.43$).

On the other hand, as Fig. 8.5 shows, for materials with $2 < \gamma < 3$ the dispersive effects can be much more important than attenuation effects. In addition, using Eq. (8.15), we obtain $N_c|_{\gamma=3} = 0$, indicating that dispersive effects strongly

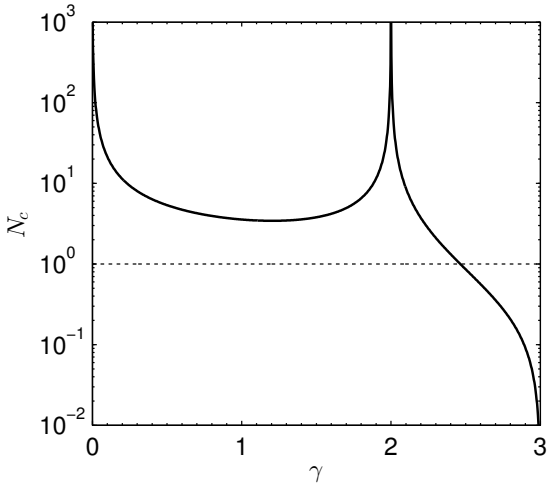


Figure 8.5: Ratio of attenuation versus dispersion, N_c, versus power law exponent γ.

dominates over attenuation effects. However, there exists few materials that falls in this range (Szabo, 1995). For the case of soft tissue media, where $1 < \gamma < 2$, the results arising from this section indicates that attenuation dominates over dispersion effects, but the phase mismatching between forced and propagating second harmonic wave is not negligible for nearly linear frequency dependent attenuation media. However, due to the absorption distance excess in about of one order magnitude the coherence distance, it is not possible to observe a complete beating. Instead, the effect of the weak dispersion in frequency power law media with $1 < \gamma < 2$ is a decreasing in the efficiency of energy transfer from the fundamental to higher harmonics. This aspect will be explored numerically in the next section.

8.3 Competition between nonlinearity and power law attenuation and dispersion

For a monochromatic plane wave in the absence of dissipation, either viscous or relaxation losses, the shock formation distance can be expressed as

$$x_s = \frac{1}{\beta \varepsilon k}, \tag{8.18}$$

with $\varepsilon = v_0/c_0$ as the acoustic Mach number, v_0 the source amplitude, and $\beta = 1 + B/2A$ the parameter of nonlinearity that accounts for material (B/A) and mass advection nonlinearity (unity factor).

In order to measure the relative relevance of nonlinear and attenuation effects, we shall define the so called Gol'dberg number for frequency power law attenuation media as the ratio of characteristic absorption length, x_a, and shock distance, x_s:

$$\Gamma_\gamma = \frac{x_a}{x_s} = \frac{\beta p_0}{c_0^3 \rho_0 \alpha_0 \omega^{(\gamma-1)}}. \tag{8.19}$$

Thus, in the same sense of the classical definition of the Gol'dberg number for thermo-viscous fluids, for $\Gamma_\gamma \gg 1$ the shock distance is too short compared to the characteristic attenuation length and the nonlinear effects dominates over attenuation. In this way, for the range $0 < \gamma < 2$ where the dispersion remains weak, the nonlinear harmonic cascade can be developed and shock waves can be observed. In the limit $\Gamma_\gamma \to \infty$ model equations reduces to lossless nonlinear acoustic and analytical solutions can be obtained for a variety of boundary conditions (e.g. in the case of monochromatic plane wave propagation the well known Fubini-Blackstock-Fay solution describes the harmonic evolution). On the other hand, in the regime $\Gamma_\gamma \ll 1$ dissipation effects dominates over nonlinear effects. Although energy transfer from fundamental to higher harmonics could be observed, absorption prevents the development of shock waves. In the limit of $\Gamma_\gamma \to 0$, linear-damped propagation is achieved and no harmonic is generated.

However, in many practical cases $\Gamma_\gamma \approx 1$ and an analytical treatment of the problem is not available (with the exception of $\gamma = 2$ where the so called Mendousse, Eq. 7.32, solution could be obtained). Due to plane-harmonic nonlinear wave propagation in a mono-relaxing media is still unsolved, the prospective is fair in order to find an exact analytical solution for multiple relaxation media or for a continuum of relaxation processes. In addition, no analytical solution is available for fractional derivatives nonlinear wave equations (Szabo, 1994) for the case of monochromatic plane wave. Thus, in this section we will explore numerical solutions of Eqs. (7.1, 7.2, 7.10, 7.8) by using the methods described in Chapter 7 in order to study the harmonic generation in frequency power law attenuation media.

In addition, one important remark arising from Eq. (8.19) for tissues with exact $\gamma = 1$ is that the ratio between nonlinearities and attenuation effects does not depend on frequency. In this way, Eq. (8.19) predicts that given media parameters, (β, c_0, ρ_0 and α_0), a wave with fixed initial amplitude will develop exact nonlinear processes with independence of the wave frequency. In this way, the amplitude can be selected and fixed in order to produce shock waves as

$$p_0 > c_0^3 \rho_0 \alpha_0 / \beta. \tag{8.20}$$

If the frequency is increased the shock formation distance is moved towards the source, but according to Eq. (8.19) the Gol'dberg ratio remains constant and therefore the harmonic balance remains the same but stretched in space.

As explained above, for $\Gamma_\gamma \approx 1$ the nonlinear and attenuation effects may play a role of similar importance in the full solution. Thus, there exist a competition between nonlinearity and attenuation effects that, at first order, leads the final amplitude for each harmonic. In one hand, harmonic generation is governed by nonlinearity, where second and higher harmonics are generated by cascade processes due to material nonlinearity and mass convection processes. On the other hand, each generated harmonic will be attenuated during propagation by its specific attenuation coefficient, provided by the frequency power law evaluated at each harmonic frequency.

Consider here media with equal attenuation at fundamental frequency, but different power law. In these media, it is obvious that for higher values of the power law exponent, γ, the attenuation of higher harmonics will be in any case higher than the attenuation for media with lower power law. Thus, in principle, the exponent has a great influence in the harmonic balance of the traveling nonlinear wave due to differences in attenuation, and these differences will be higher for higher harmonics.

However, as long frequency power law attenuation introduces dispersion, see Eq. (8.2), the phase matching conditions are in general no longer fulfilled. Therefore, dispersion modifies the efficiency on harmonic generation, together with the interplay between power law attenuation and nonlinear harmonic growing. Thus, from Eqs. (8.10, 8.11), phase matching conditions, i.e. $\Delta k_2 = 0$, are fulfilled for even powers, e.g. $\gamma = 0, 2, \ldots$. In these cases, propagation is nondispersive: the nonlinear efficiency is maximum and therefore the energy transference from fundamental to higher harmonics is maximized. On the other hand, for $\gamma \approx 1$, dispersive propagation is predicted and the nonlinear efficiency will be modified. Due to these effects cannot be isolated, we study the modification of the nonlinear efficiency numerically.

8.4 Plane wave simulations in power law media

As shown Chapter 7, the propagation of nonlinear acoustic waves in frequency power law attenuation can be modeled by the use of multiple relaxation processes. Thus, the set of Eq. (7.1, 7.2, 7.10 and 7.8) can be expressed for a plane wave travelling in x direction as

$$\frac{\partial \rho}{\partial t} = -\frac{\partial (\rho v_x)}{\partial x}, \tag{8.21}$$

$$\frac{\partial v_x}{\partial t} = -\frac{1}{\rho}\frac{\partial p}{\partial x} - \frac{1}{2}\frac{\partial v_x^2}{\partial x} + \frac{1}{\rho}\left(\frac{4}{3}\eta + \zeta\right)\frac{\partial^2 v_x}{\partial x^2}, \tag{8.22}$$

$$p = c_\infty^2 \rho' + \frac{c_0^2}{\rho_0}\frac{B}{2A}\rho'^2 - \sum_{n=1}^{N} S_n, \tag{8.23}$$

$$\frac{\partial S_n}{\partial t} = -\frac{1}{\tau_n} S_n + \frac{\eta_n c_0^2}{\tau_n}\rho', \tag{8.24}$$

where v_x is the x component of particle velocity vector.

In order to study the changes induced by power law attenuation and dispersion into the nonlinear efficiency, we consider media with equal attenuation coefficient at fundamental frequency, ω_0, as shown in Fig. 8.2. Thus, by varying power law exponent from realistic values for biological media, $\gamma = [0.5, 2]$, dispersion is introduced while the attenuation of the fundamental wave remains constant. As Eq. (8.15) shows, the balance between attenuation and dispersion for power law media (N_c) only depends on the power law exponent. In this way, by increasing the attenuation magnitude both dispersion and attenuation effects will by modified in same amplitude. On the other hand, by modifying the attenuation magnitude the Gol'dberg number for power law media is also modified following Eq. (8.19). In summary, for media with equal attenuation coefficient at fundamental frequency, the balance between nonlinearity and attenuation effects, Γ_γ is governed by the attenuation coefficient, while the balance between attenuation and dispersion effects, N_c, is governed by the exponent of the power law.

Numerical results for the spatial distribution of fundamental wave are shown in Fig. 8.6, while the spatial distribution for second and third are plotted in Fig. 8.7. The amplitude and fundamental wave of the excitation was maintained constant, thus, by changing attenuation magnitude the ratio between attenuation and nonlinearity is modified and therefore the ratio between dispersion and nonlinearity also is modified.

Here, the analytical nonlinear solution for lossless media (Bessel-Fubini's solution) is plotted in dotted line. Thus, for low attenuation media, i.e. when $\Gamma_\gamma \to \infty$, nonlinear effects dominate over attenuation and dispersion and therefore the numerical solution for frequency power law media converges to the lossless Bessel-Fubini's solution, see Fig. 8.6 and Fig. 8.7 for $\Gamma_\gamma = 57.9$. In these cases, the fundamental wave decay is mainly due to energy transference to higher harmonics, that grow with propagation. Here, harmonic amplitude is independent on the exponent of the power law, showing that both dispersion and attenuation effects are much less smaller compared with nonlinear effects during propagation and can be neglected for $\Gamma_\gamma \to \infty$.

In contrast, as Figs. 8.6, 8.7 show for $\Gamma_\gamma = 0.74$, for high damped media and weak nonlinearity, attenuation effects are comparable to nonlinear harmonic pumping. The fundamental wave not only decays for energy transfer but also due to high attenuation.

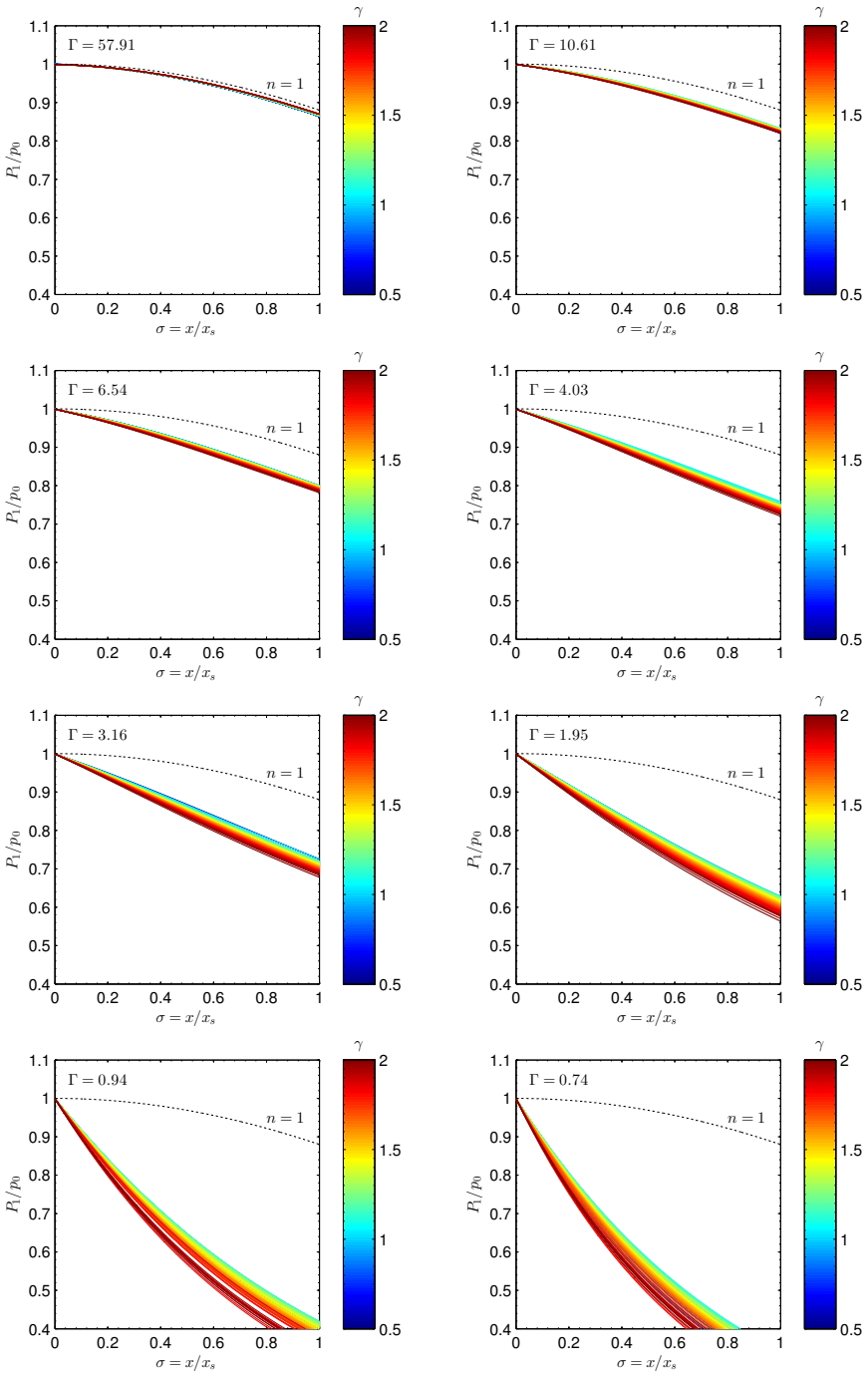


Figure 8.6: First harmonic normalized-amplitude spatial distribution for different frequency power laws. For each subplot, the ratio of nonlinear to power law attenuation effects, Γ_γ, is increased

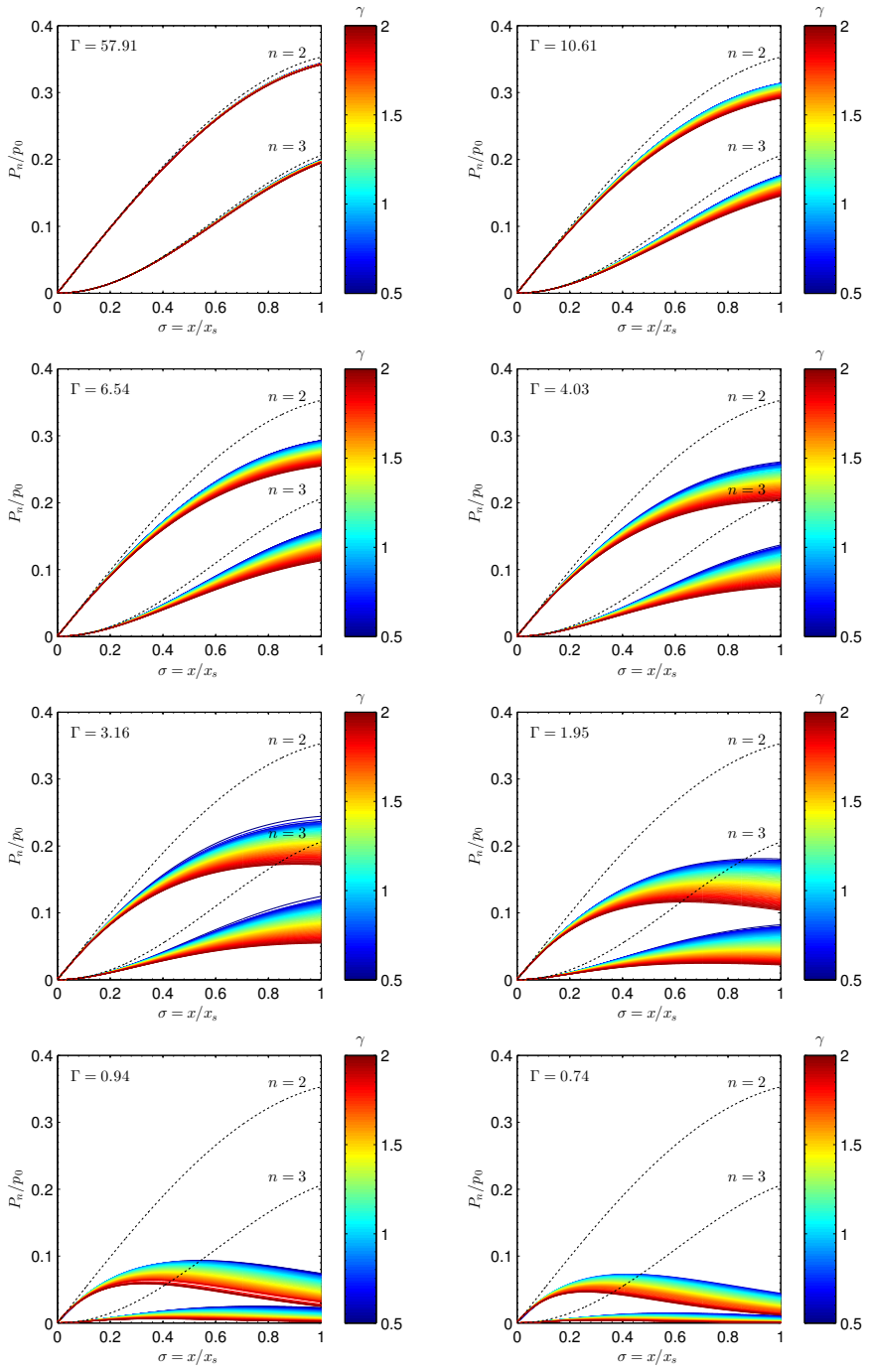


Figure 8.7: Second and third harmonic normalized-amplitude distribution for different frequency power laws. For each subplot, the ratio of nonlinear to power law attenuation effects, Γ_γ, is increased

Thus, at distance $\sigma \approx 0.5$ fundamental wave have loss approximately half of its initial amplitude and therefore nonlinear energy transfer processes to second-and-higher harmonics also diminishes. On the other hand, second and third harmonics are mainly generated near the source, where fundamental wave is still have enough amplitude. However, attenuation of higher harmonics is in any case higher than for fundamental wave and therefore they are quickly damped by the power law lossy media. Due to the harmonic generation is strongly decreased far away from the source due to fundamental wave energy loss, second and higher harmonics are restricted near the source and its maxima value is produced for $\sigma < 1$, in contrast with lossless media where the maxima of the harmonics is produced $\sigma \approx \pi/2$.

It is worth noting here that the harmonic evolution is strongly dependent on the exponent of the power law. Thus, due to differences in attenuation coefficient for each harmonic (see Fig 8.2 for $\omega/\omega_0 = 2$), second-and-higher harmonic amplitude is damped by different magnitude, where obviously higher attenuation and therefore lower harmonic amplitude is observed for the cases of $\gamma \to 2$.

However, although the fundamental wave attenuation magnitude is the same, with independence of the power law exponent, the amplitude of the fundamental wave strongly varies. We recall here to Eq. (8.15), that shows the ratio between dispersion and attenuation. By varying the power law exponent dispersion is modified. Thus, the harmonic efficiency is only maximized for even powers of γ, where for $\gamma \approx 1$ dispersion effects are not negligible. This is the reason because more energy remains in the fundamental wave for $\gamma \approx 1$, dispersion is modifying the phase matching conditions and therefore the energy transfer from fundamental to second-and-higher harmonics is decreased.

8.5 Nonlinear efficiency

As explained above, the nonlinear efficiency can be strongly dependent not only on the magnitude of the attenuation, but also on the dispersion due to frequency power law attenuation. These effects have been shown previously for tissue like media in the absence of dispersion (Haran et al., 1983) and including power law dispersion (Kashcheeva et al., 2000; Wallace et al., 2001) for selected media. A closer view of these phenomena can be studied by showing the harmonic amplitude at a given distance, that for reference we choose $\sigma = 1$. Thus, Fig. 8.8 shows the amplitude of the fundamental wave for different power law media and its dependence on the power law. As commented above, if the balance between nonlinear and attenuation effects is constant, the maximum amplitude of the fundamental component is observed for power laws where dispersion is maximized, i.e. for $\gamma \approx 1.2$. Furthermore, there exist differences between different Gol'dberg numbers: the balance between nonlinearity and dispersion is also coupled to the attenuation, so for high Gol'dberg numbers dispersion effects also dominate over nonlinear effects, leading to a decreasing in the nonlinear efficiency and therefore

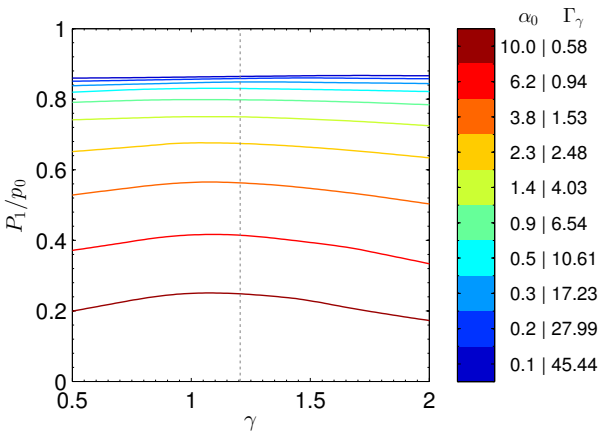


Figure 8.8: Amplitude of the fist harmonic for different Gol'dberg number (Γ_γ) in function of the exponent of the frequency power law (γ), measured at shock formation distance, $\sigma = 1$. The attenuation of the media is selected for achieve a constant value at first harmonic frequency, so for this plot the amount of media attenuation is independent of the power law.

more energy remains in the fundamental component of the nonlinear wave.

A knowledge of the role of the power law dispersion into the second-and-higher harmonic components is not so evident. If dispersion is modified, i.e. we force a change in the power law exponent, the attenuation magnitude at second harmonic frequency will be also modified. On the other hand, is obvious that if attenuation is matched for second harmonic, e.g. being the source frequency $\omega_0/2$ in Fig. 8.2, the attenuation magnitude at fundamental wave will be different.

Left side of Fig 8.9 shows the harmonic amplitude in function of the power law exponent at distance $\sigma = 1$ for different Gol'dberg ratios. Observing the harmonic amplitude is not obvious that, as stated, more energy is transferred for nondispersive power law media ($\gamma \to 0, 2, ...$). Thus, as attenuation is strongly increased for second harmonic in function of the power law exponent, the harmonic amplitude is therefore more attenuated for the non-dispersive cases, masking the effect of nonlinear efficiency.

In this way, we introduce in the right side of Fig 8.9 a compensation of the second harmonic amplitude by the attenuation coefficient at this frequency. In this plot, it is appreciable that for nondispersive cases, $\gamma = 2$, the harmonic amplitude is higher due to the phase matched generation, while for the dispersive cases there exist a reduction in the efficiency for second harmonic generation. However, this compensation does not take into account that harmonics are generated *during* propagation. Thus, it serves as an eye guide for illustration purposes but lacks of exact physical fidelity.

Similar plots, shown in Fig. 8.10, are generated for third harmonic at shock

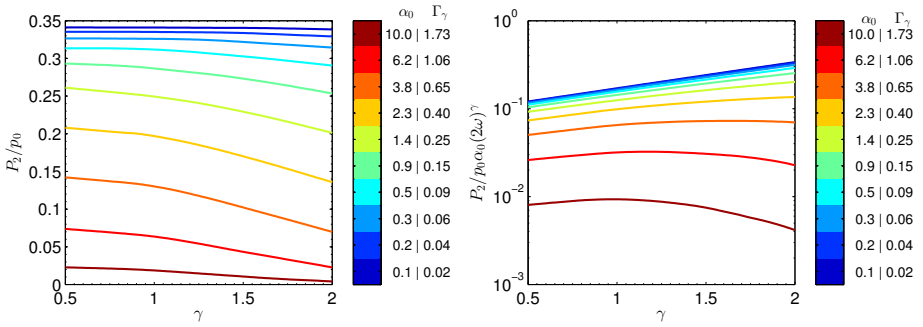


Figure 8.9: Left: Amplitude of the second harmonic for different Gol'dberg number (Γ_γ) in function of the exponent of the frequency power law (γ), measured at shock formation distance, $\sigma = 1$. Right: Same curves compensated by the increment of attenuation of second harmonic, which is different for each power law.

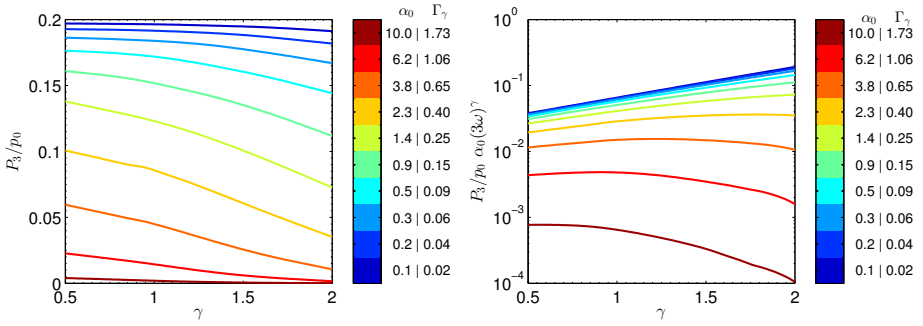


Figure 8.10: Left: Amplitude of the third harmonic for different Gol'dberg number (Γ_γ) in function of the exponent of the frequency power law (γ), measured at shock formation distance, $\sigma = 1$. Right: Same curves compensated by the increment of attenuation of third harmonic, which is different for each power law.

formation distance. Here, the amplitude is lower compared to second harmonic due to nonlinear generation. In this case, for a given Gol'dberg ratio the differences in the harmonic amplitude between different power laws increases, mainly due to the increasing in the attenuation coefficient at third harmonic frequency. Moreover, if the attenuation of each harmonic amplitude is compensated, as shown in right hand side of Fig. 8.10, the behavior is the similar than the observed to the second harmonic efficiency.

8.6 Phase changes induced by dispersion

From the dispersion relations for power law media, showed in Fig.8.1, it is appreciable that second harmonic component propagates, for $0 < \gamma < 2$, faster than

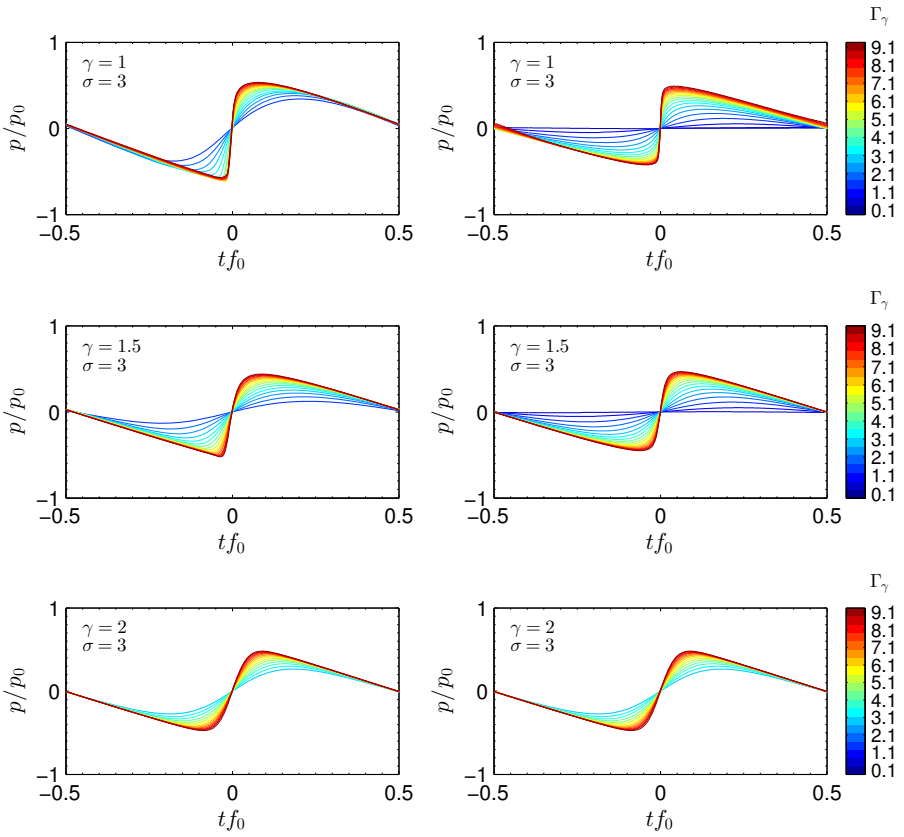


Figure 8.11: Waveforms calculated for (left) dispersive power law media at distance $\sigma = 3$ and (right) artificial dispersionless only taken into account power law absorption. From up to down the power law exponents ranges are $\gamma = [1, 1.5, 2]$

fundamental wave. The second harmonic that is generated near the source, after propagation, will sum with the harmonics at higher distances. Due to the locally generated second harmonic waves are in phase with fundamental wave, there exist a phase difference between the forced (locally generated) and the background propagation second harmonic wave. This phase shift can be predicted from dispersion relations, as is dependent to phase matching conditions (Eq.8.8). In the case of second harmonic, a complete phase shift between propagating and forced waves occurs every $x = 2x_c$. In this way, as explained in Section 8.5, these processes modify the efficiency of the nonlinear generation in frequency power law attenuation media.

In addition, these phase changes also modify the shape of the nonlinear waveforms in frequency power law media. The shape of a nonlinear waveform is determined by its specific harmonic balance, but also the relative phase between

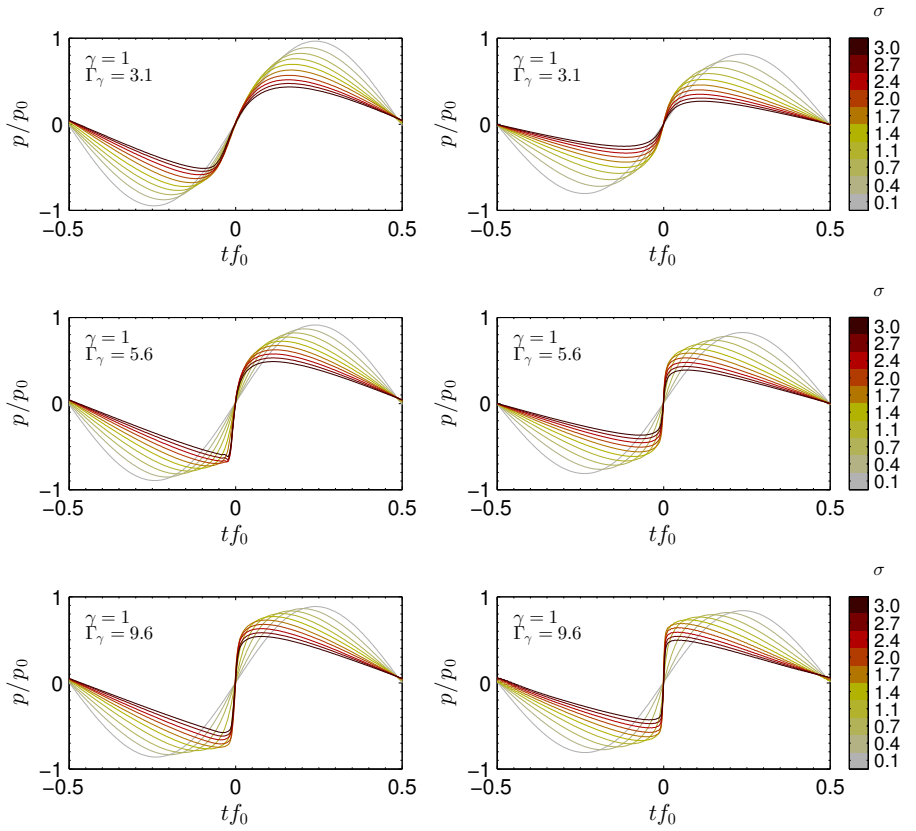


Figure 8.12: Waveform evolution calculated for linear power law ($\gamma = 1$). (Left) dispersive propagation. (Right) nondispersive simulation for comparison using artificial dispersionless power law absorption. From up to bottom the ratio between nonlinear and attenuation (Γ_γ) effects is increased.

spectral components. In nondispersive media, the harmonic balance is a competition between nonlinearity and absorption processes. As seen in this Chapter, dispersion of power law media modifies this balance. Moreover, the relative phase between spectral components will be also modified due to dispersion and it will change the shape of the waveform.

To study these effects, we use a k-space pseudospectral method (Treeby et al., 2010; Treeby et al., 2012) to evaluate one dimensional nonlinear propagation. This method, through the spectral representation of the field, provides an efficient way to evaluate the linear integro-differential operator based fractional Laplacian that introduces frequency power law attenuation. This also provides a way to eliminate dispersion and evaluate only a nondispersive version of the frequency power law operator.

Thus, Fig. 8.11 shows the nonlinear waveforms measured at distance $\sigma = 3$ including dispersion and an artificial nondispersive version of the frequency power law attenuation operator in the k-space. As can be seen, the specific shape of the waveform depends on the exponent of power law: it provides a balance in the harmonic magnitude through attenuation processes and the above described changes on the efficiency through dispersion processes.

However, if the power law attenuation is maintained but dispersion is artificially not included in the calculations, there can be seen that the waveforms shape presents several changes. Thus, as Fig. 8.11 shows, dispersion breaks the symmetry of the nonlinear waveforms. In the case of nondispersive propagation the waveforms for $\Gamma_\gamma \gg 1$ converge to the well-known sawtooth waves as predicted by the Fubini-Blackstock-Fay solution (Hamilton et al., 1998a). For intermediate Γ_γ values, due to different balance in harmonic attenuation during propagation, the shape of the final waveforms is also slightly changed. However, in this case of artificially nondispersive propagation, the shape of the waveforms conserve the symmetry between compression and rarefaction cycles typical of sawtooth waves.

In contrast, this symmetry is broken for the waveforms generated including dispersion, in the same sense as in other dispersive systems as mono-relaxing fluids (Hamilton et al., 1998a). A more detailed frame for $\gamma = 1$ is presented in Fig. 8.12, where the complete evolution of the waveforms is represented in each frame. Here it can be seen how the shock front is smoothed in the compression phase, while remains sharp in the negative rarefaction phase.

8.7 Conclusions

In this chapter we have revised the fundamental problem of the competition between nonlinear and attenuation effects in frequency power law attenuation media, with special emphasis in the effects of the weak dispersion. We have derived simple expressions in order to quantify the role of the exponent of the power law in the balance between nonlinearity, dispersion and attenuation. The results show that the dispersion effects present more relevance in the nonlinear propagation for media obeying $\gamma \approx 1.2$, where the ratio between nonlinear characteristic distance and weak dispersion characteristic distance present its minimum. Detailed numerical examples are given in agreement with this predictions. This situation is of special interest due to most soft tissues typically present values of the power law exponents around this critical value.

The efficiency in the harmonic generation is studied numerically, showing that power law dispersion modifies the cumulative energy transfer to higher harmonics. Thus, considering a media with same attenuation value at the fundamental component, more energy remains in the fundamental harmonic component in the cases of nearly linear power law. On the other hand, in frequency power law

media attenuation effects are of higher importance in the nonlinear propagation than weak dispersion effects. However, we have shown that the waveform shape also strongly depends on the weak dispersion, where the characteristic asymmetric profile is observed for dispersive frequency power law attenuation.

In real situations, where other phenomena must to be included (beam diffraction, tissue scattering and inhomogeneities, ...), it becomes far more complicated to study the role of each effect in the nonlinear propagation. Thus, plane wave propagation offers the possibility to isolate some of the physical mechanisms that governs nonlinear propagation (in this case attenuation and dispersion) and to understand the balance between them. The results presented in this chapter, far from present completely new physics, offers detailed calculations and a broad view of this fundamental problem.

References

Fry, FJ and JE Barger (1978). "Acoustical properties of the human skull". In: *The Journal of the Acoustical Society of America* 63.5, pp. 1576–1590.

Hamilton, Mark F, David T Blackstock, et al. (1998a). *Nonlinear acoustics*. Vol. 237. Academic press San Diego.

Haran, Michael E and Bill D Cook (1983). "Distortion of finite amplitude ultrasound in lossy media". In: *The Journal of the Acoustical Society of America* 73.3, pp. 774–779.

Hill, C.R., J. C. Bamber, and G.R. ter Haar (2004). *Physical Principles of Medical Ultrasonics, 2nd ed.* John Wiley & Sons Ltd, Chichester, England.

Kashcheeva, S.S., O.A. Sapozhnikov, V.A. Khokhlova, M.A. Averkiou, and L.A. Crum (2000). "Nonlinear distortion and attenuation of intense acoustic waves in lossy media obeying a frequency power law". In: *Acoustical Physics* 46, pp. 170–177.

O'Donnell, M., E. T. Jaynes, and J. G. Miller (1981). "Kramers–Kronig relationship between ultrasonic attenuation and phase velocity". In: *J. Acoust. Soc. Am.* 69.3, pp. 696–701.

Rudenko, O.V. and S.I. Soluian (1977). *Theoretical foundations of nonlinear acoustics*. Studies in Soviet science. New York, NY 10011, USA: Consultants Bureau, p. 274.

Szabo, Thomas L (1994). "Time domain wave equations for lossy media obeying a frequency power law". In: *J. Acoust. Soc. Am.* 96.1, pp. 491–500.

Szabo, Thomas L (1995). "Causal theories and data for acoustic attenuation obeying a frequency power law". In: *J. Acoust. Soc. Am.* 97.1, pp. 14–24.

Treeby, Bradley E and BT Cox (2010). "Modeling power law absorption and dispersion for acoustic propagation using the fractional Laplacian". In: *J. Acoust. Soc. Am.* 127.5, pp. 2741–2748.

Treeby, Bradley E, Jiri Jaros, Alistair P Rendell, and BT Cox (2012). "Modeling nonlinear ultrasound propagation in heterogeneous media with power law absorption using a k-space pseudospectral method". In: *J. Acoust. Soc. Am.* 131.6, pp. 4324–4336.

Wallace, Kirk D, Mark R Holland, and James G Miller (2001). "Improved description of shock wave evolution in media with frequency power law dependent attenuation". In: *The Journal of the Acoustical Society of America* 109.5, pp. 2263–2265.

Waters, Kendall R, Michael S Hughes, Joel Mobley, Gary H Brandenburge, and James G Miller (2000). "On the applicability of Kramers–Krönig relations for ultrasonic attenuation obeying a frequency power law". In: *The Journal of the Acoustical Society of America* 108.2, pp. 556–563.

Waters, Kendall R, Joel Mobley, and James G Miller (2005). "Causality-imposed (Kramers-Kronig) relationships between attenuation and dispersion". In: *Ultrasonics, Ferroelectrics and Frequency Control, IEEE Transactions on* 52.5, pp. 822–823.

Publications

The contents of this chapter have been presented in the following publications:

Conference proceedings

- **Jiménez, N.**; Redondo, J.; Sánchez-Morcillo, V.; Iglesias, P. C. and Camarena, F. "On the Nonlinear Effects in Focused Ultrasound Beams with Frequency Power Law Attenuation" *43rd Annual UIA Symposium*, Madrid, Spain. 23 - 25 April. In: *Physics Procedia*, Volume 63, 2015, Pages 47-53, (2014)



Chapter 9

Nonlinear Acoustic Radiation Forces in Biological Media

Abstract

In this Chapter we present the finite-amplitude dependence of the acoustic radiation force (ARF) in a soft tissue-like media. The acoustic radiation force is calculated in media with different exponent of the frequency power law attenuation. Numerical results are obtained for one dimensional propagation, where the spatial distribution of the force field is studied. The results obtained show that the nonlinear dependence of the acoustic radiation force sharply depends on the tissue attenuation model for both, weakly and strong nonlinear regime. We also show the underestimation of the momentum transfer in the nonlinear regime by calculating the ARF by using the wave intensity. Considerations due to nonlinear absorption are included and the relation between the momentum transfer and energy deposition is underlined.

9.1 Introduction

Waves carry energy and momentum. Propagation trough lossless homogeneous media implies the absence of interaction between the medium and the wave. However, if scattering or absorption processes are present, the energy and momentum can be transferred from the wave to the medium. In this sense, the radiation force is an universal wave phenomenon related to the momentum transfer from a wave to the medium. It has been demonstrated to exist for electromagnetic (Lebedew, 1901), acoustic waves (Faraday, 1831; Rayleigh, 1902), and also by phonons in crystal lattices (Sorbello, 1972) as those presented in Chapter 1.

In the case of acoustic waves, acoustic radiation forces (ARF) appear when a gradient in the acoustic energy density is produced by scattering or absorption processes. We refer to the critical review of Sarvazyan et al. (2010) for a broad historical references and a clear description of the ARF in the acoustic context. The acoustic radiation force is a time-average second-order process. In the case of a continuous monochromatic wave, steady state acoustic radiation forces appear when the wave is scattered by an object, reflected by a rigid surface or an interface between two media, or absorption is produced in the propagation. In all these situations, some momentum is transferred from the wave to the medium, and the consequence is that the acoustic radiation tensor Beyer (1978) is no longer spatially constant. In these cases, the bulk of the medium is time average stressed. The radiation forces are only one of the consequences of this stresses. In fluids, the acoustic radiation stresses induce time average movements or streams. In solids and elastic media in general, time average stresses induce constant strains, being the material deformed in the direction of the wave but also in the transversal direction. In fluids with inclusions, the scatterers can be statically compressed, deformed, pushed, and also rotated by the induced acoustic radiation stress.

Therefore, is no surprising the huge amount of practical applications that exploit the phenomena related acoustic radiation stresses due to the extremely broad possibilities for interacting with the media using acoustic waves.

In the case of biological media and medical ultrasound applications, the use of acoustic radiation force includes the power calibration of High Intensity Focused Ultrasound (HIFU) devices by radiation force balances (Wood et al., 1927); acoustical tweezers and levitation for particle and cell manipulation (Wu, 1991; Lee et al., 2006; Hultström et al., 2007); stimulation of sensory receptors by ultrasound radiation force or improving targeted drug and gene delivery (Sarvazyan et al., 2010). On the other hand, acoustic streaming can be used for stirring and mixing liquids (Sarvazyan et al., 2009), remote assessment of biological fluids (Nightingale et al., 1995) and microfluidics applications (Laurell et al., 2007; Hultström et al., 2007). It is worth noting here that in some of these techniques the effects of the acoustic radiation force and streaming are closely linked.

One important remark is that the time averaging of the acoustic radiation

stresses can be modulated by a slowly varying time function. If the wave amplitude presents a low frequency modulation (compared to the acoustic variations), the radiation stresses are also modulated in time, leading to oscillating radiation forces inside the media. In elastic media, these stresses dynamically deform the bulk of the medium in axial and also in transversal direction. Thus, time varying shear deformations induce shear waves at the modulation frequency, that propagates transversely to the direction of the wave.

A huge amount of ultrasound medical diagnostic techniques have been developed in order to asset the media elasticity by measuring the mechanical response of the tissues under the action of acoustic radiation stresses. In general, the elasticity can be evaluated by measuring in some way the strains induced by the ultrasound field. These techniques include vibroacoustography (VA) (Fatemi et al., 1998; Urban et al., 2011), shear wave elasticity imaging (SWEI) (Sarvazyan et al., 1998), acoustic radiation force impulse imaging (ARFI) (Nightingale et al., 2001; Trahey et al., 2004), supersonic shear imaging (SSI) (Bercoff et al., 2004), harmonic motion imaging (HMI) (Konofagou et al., 2003; Vappou et al., 2009) and real time monitoring of lesion formation in HIFU therapy (Maleke et al., 2008). Also, the induced tissue deformations can be tracked with other imaging techniques as magnetic resonances (Fowlkes et al., 1995; Manduca et al., 2001). Acoustic streaming can be used to assessment and detecting fluid-filled lesions or cysts (Nightingale et al., 1995; Nightingale et al., 1999) or monitoring blood coagulation by sonorheometry (Viola et al., 2004). We refer to the reviews (Sarvazyan et al., 2010; Palmeri et al., 2011; Doherty et al., 2013) and references therein for further details.

Human soft tissues show strong acoustic attenuation processes, but also internal scattering due to micro-inhomogeneity. It is commonly accepted that the contribution to the acoustic radiation force in the bulk of soft tissues is mainly caused by absorption rather than scattering processes (Doherty et al., 2013). In order to obtain high amplitude acoustic radiation force fields and induce detectable deformations, the amplitude of the ultrasonic excitation is commonly high enough to excite nonlinear effects in some degree (Carstensen et al., 1980), even in diagnostic techniques (Sarvazyan et al., 2010). On the other hand, although radiation forces are observed also for small amplitude waves, the acoustic radiation force is a second order process and therefore requires solutions to the nonlinear model equations.

At ultrasound frequencies, soft tissues do not effectively support shear wave propagation. The typical shear wave speed in soft tissue is around two orders of magnitude lower that the longitudinal acoustic wave speed. Shear waves generated by low frequency modulated acoustic radiation forces, present different spatio-temporal scale to the longitudinal waves. The common approach is to model first the acoustic radiation force generated by the ultrasonic longitudinal waves. Then, shear waves and the corresponding tissue strain are treated as uncoupled problem: the time-varying acoustic radiation force field is used as an excitation of some elastic model, commonly a linear elastic or viscoelastic solid model. Therefore, the

constitutive equations for nonlinear acoustics are accurate to describe the nonlinear generation of acoustic radiation force, provided that the proper attenuation and dispersion are included in the model as a frequency power law.

The aim of this Chapter is to study the acoustic radiation forces induced by intense waves in soft tissue. Thus, we present the nonlinear dependence of the acoustic radiation force by solving numerically the constitutive equations for nonlinear acoustics in a broad range of frequency power law attenuation media. We show special emphasis in the effects of the power law frequency attenuation.

9.2 One dimensional acoustic radiation force

The problem of accurately solve the acoustic radiation force is associated to the knowledge of the full acoustic field variables: pressure p, density ρ and particle velocity vector $\mathbf{v}$. For plane waves in a lossless homogeneous media, the relation between these quantities is well-known, but in this case no acoustic radiation force appears. The inclusion of some frequency dependent attenuation and its corresponding dispersion induce a phase shift between the acoustic variables and its relationship becomes more complicated.

For the sake of simplicity, we start by review the acoustic radiation force generated by plane waves. We first expand in series the acoustic magnitudes, p, ρ, v as in Refs (Sarvazyan et al., 2010; Doherty et al., 2013). Thus, each term includes a high-order correction to to the steady-state solutions p_0, ρ_0, v_0. For a quiescent homogeneous fluid, $v_0 = 0$ and p_0 and ρ_0 are time independent, p_1, ρ_1 and v_1 are the first order approximations to the acoustic field, and p_2, ρ_2 and v_2 are the second order corrections. Thus, the field can be expressed as

$$p = p_0 + p_1 + p_2 + \cdots \tag{9.1}$$
$$\rho = \rho_0 + \rho_1 + \rho_2 + \cdots \tag{9.2}$$
$$v = 0 + v_1 + v_2 + \cdots \tag{9.3}$$

assuming that each term is small that the preceding one.

The problem of modeling the acoustic radiation force F^V (per unit volume), reduces to obtain the time-average of the change in momentum for a fluid as

$$F^V = -\left\langle \rho \frac{\mathrm{D}v}{\mathrm{D}t} \right\rangle . \tag{9.4}$$

It is important to note that the period average (indicated as $\langle\rangle$) of the first order magnitudes (p_1, ρ_1, v_1) is zero. However, the time average of the momentum

does not vanish due to the nonlinearity in material derivative of the momentum Eq.(9.4). Substitution of Eqs.(9.1-9.3) into the momentum equation, and keeping up to second order terms leads to (Doherty et al., 2013)

$$F^V = -\left\langle \rho \frac{\mathrm{D}v}{\mathrm{D}t} \right\rangle = -\left\langle \rho_0 \frac{\partial v_2}{\partial t} + \frac{\partial \rho_1 v_1}{\partial t} + \rho_0 \left(v_1 \nabla \cdot v_1 + v_1 \cdot \nabla v_1 \right) \right\rangle . \tag{9.5}$$

The period average of the first two terms of the right hand side is zero, but the last 2 terms, that account for the nonlinearity of the material derivative, does not vanish. Thus, for a plane wave propagating in the x direction, the acoustic radiation force per unit volume reads

$$F_x^V = -\left\langle \rho_0 \frac{\partial v_1^2}{\partial x} \right\rangle . \tag{9.6}$$

Then the volume radiation force for a decaying plane harmonic wave with instantaneous intensity $I' = p_1 v_1 = \rho_0 c_0 v_1^2$, traveling in an homogeneous-lossy media can be expressed as

$$F_x^V = -\frac{\partial}{\partial x} \left\langle \frac{I'}{c_0} \right\rangle , \tag{9.7}$$

or in terms of the time-average intensity I in a period $T = 2\pi/\omega$

$$I = \frac{1}{T} \int_t^{t+T} I' \, \mathrm{d}t = \langle I' \rangle , \tag{9.8}$$

the volume radiation force is proportional to the gradient of the intensity divided by the sound speed

$$F_x^V = -\frac{\partial}{\partial x} \left(\frac{I}{c_0} \right) . \tag{9.9}$$

Here we shall recognize that the quantity I/c_0 can be expressed as

$$\frac{I}{c_0} = \frac{1}{2} \rho_0 v^2 + \frac{1}{2} \frac{p^2}{\rho_0 c_0^2} , \tag{9.10}$$

where it is evident that is the total energy density for a plane wave. Thus, is clear that Eq. (9.9) essentially states that an acoustic radiation force must appears when a spatial change in the energy density distribution is produced. The derivation of this equation was developed for homogeneous media, thus, strictly speaking a change of the energy density can only be produced by absorption processes. However, it is well-known that acoustic radiation forces also appear when a change of

the energy density is produced by reflection between media with different acoustic properties. Here, we ignore these contributions and assume a homogeneous absorbing soft tissue media, where the contribution of the tissue attenuation to the absorption of the wave is dominant compared to the internal scattering processes.

Small amplitude waves

Thus, if considering an absorbing-media with an attenuation coefficient α, a monochromatic plane wave traveling will present a mean intensity as

$$I = \rho_0 c_0 V_0^2 \exp(2\alpha x)/2, \tag{9.11}$$

with V_0 the excitation particle velocity.

Substituting the intensity of Eq. (9.11) in Eq. (9.9), the time average force per unit volume reads

$$F^V_{x,\text{lin}} = 2\alpha \frac{I}{c_0} = \alpha \frac{p'^2}{\rho c_0^2}\,, \tag{9.12}$$

that is the most common approach to calculate the acoustic radiation force in absorbing media. We shall note some peculiarities of this simple expression. It can be observed that the resulting force is proportional to the wave intensity and the attenuation coefficient. For diagnostic ultrasound frequencies the absorption coefficient is typically high, around 1 dB/cm or even higher, and for the commonly used intensities the magnitude of the acoustic radiation force is weak. Therefore, the induced displacements are had to detect ($< 1\mu$m) (Doherty et al., 2013). Thus, for induce detectable displacements (typically from 1 to 10 μm) two basic mechanisms are used. First is focusing. By increasing the gain of the source the intensity can be increased locally inducing higher ARF and displacements. On the other hand, the intensity of the field can be increased directly by increasing the amplitude of the excitation. However, for both approaches the calculation of the radiation force becomes complex.

In the first place, Eq. (9.12) was derived for plane waves and therefore, the calculation of the acoustic radiation force for more complex fields by using this expression is not accurate. For directional beams this expression is valid for low focused fields and only at the focal, where the wavefront can be considered quasi-plane. However, for strongly focused fields the assumption of planes waves no longer holds. For an accurate description of the acoustic radiation force the spatial features of the beam must be included. In the case of paraxial beams analytic approaches can be obtained for intense waves (Rudenko et al., 1996; Ostrovsky et al., 2007; Ostrovsky, 2008), but for strongly focused sources a better theoretical foundation is needed. Approaches include calculating the full radiation stress tensors numerically or by indirect measurement of the acoustic radiation forces, e.g. by estimating streaming in frequency power law absorbing fluids.

Nonlinear regime

Secondly, if the source amplitude is increased, nonlinear effects can be produced. In the case of weakly nonlinear effects, the absorption of each harmonic is different following the tissue frequency power law attenuation. If Eq. (9.12) is used the force can be calculated by the sum of the contributions of each harmonic separately. However, strictly speaking this equation is not exact in nonlinear regime. The main reason is that in nonlinear regime the intensity distribution of the wave is not exactly the given by Eq. (9.11). As long the energy is transferred to the higher harmonics, and the higher spectral components present higher attenuation, the intensity decay is not exponential, leading to the so-called nonlinear absorption. Thus, in the nonlinear regime these processes leads to a increasing rate of momentum transfer from the wave to the media, and therefore the acoustic radiation force is increased.

If the losses are caused by thermo-viscous effects, alternatively the nonlinear acoustic radiation force can be calculated directly using the expression (Rudenko et al., 1996)

$$F^V_{x,\text{thermo}} = \frac{b(\beta'+1)}{c_0^5 \rho_0^3} \left\langle \left(\frac{\partial p'}{\partial t} \right)^2 \right\rangle , \tag{9.13}$$

where β' is the nonlinear compressibility (often neglected) and the dissipation coefficient, b, is given by

$$b = \frac{4}{3}\mu + \mu_B + \kappa \left(\frac{1}{C_V} - \frac{1}{C_p} \right) , \tag{9.14}$$

that accounts for the quadratic frequency attenuation caused sound thermo-viscous diffusion processes, being μ the shear viscosity, μ_B the bulk viscosity, κ the thermal conductivity and C_V and C_p the specific heats at constant volume and pressure respectively.

Equation (9.13) is valid in both, linear and nonlinear regimes. In the first case, substitution of a monochromatic wave in Eq. (9.13) gives Eq. (9.12). On the other hand, Eq. (9.13) states that for complex nonlinear acoustic fields with sharp waveforms, as those containing shock waves, the squared time-derivative of the pressure will have a non negligible period average value. Therefore, the nonlinear acoustic radiation force is increased when sharp waveforms are present in the domain.

Sawtooth regime

If the nonlinear processes are strong enough to produce very sharp wave steepening, the wave can be described by the a sawtooth waveform. This regime occurs at

distances $\sigma > 3$ and Gol'dberg ratios $\Gamma >> 1$. Thus, an analytic expression can be obtained for waveforms containing shock waves by substituting a sawtooth waveform in Eq. (9.13). The substitution of a sawtooth profile into Eq. (9.13) gives (Pishchalnikov et al., 2002; Rudenko et al., 2004)

$$F^V_{x,\text{saw}} = \frac{2\pi^2}{3}\left(\beta' + 1\right)^2 \omega \frac{\rho_0}{c_0^2} u_0^3\left(x\right), \tag{9.15}$$

where $u_0(x)$ is the amplitude of the particle velocity in one period of the sawtooth. It is important to note that in the sawtooth regime the acoustic radiation force does not depend on the absorption of the media. This effect is due to the nonlinear intensity absorption dominates over the tissue attenuation in the sawtooth regime. On the other hand, the cubic amplitude dependence, instead of the quadratic one for the linear estimation, evidences the great potential of the sharp waveform to enhance acoustic radiation force in the nonlinear regime.

Thus, the acoustic radiation force for plane waves is well understood in the case of thermo-viscous losses, where the magnitude of the force varies between to limits (1) the small amplitude regime, where the force decays exponentially with distance, and (2) the nonlinear absorption regime, where the ARF is proportional to the cube of the sawtooth peak particle vibration.

9.3 Nonlinear radiation force in tissue-like media

In the case of frequency power law absorption media, the acoustic radiation force for small amplitude waves is equivalent by selecting the appropriate attenuation coefficient and the intensity of each spectral component. However, Eq. (9.13) is no longer valid for media with non-quadratic frequency dependent attenuation, and therefore the calculation of the ARF in the nonlinear regime becomes complex. Here, we calculate the ARF using the mean change in momentum by solving numerically the full constitutive relation of nonlinear acoustics by using the method described in Chapter 7.

The aim of our work is to understand the role of the frequency dependent attenuation in the nonlinear generation of acoustic radiation forces.

We start presenting the intensity of a plane wave in two absorbing media, for thermo-viscous absorption, where the exponent of the frequency power law is $\gamma = 2$ and for tissue absorption, $\gamma = 1$. Figure 9.1 shows the intensity distribution for these two attenuation models, where each curve represents a different Gol'dberg ratio: for $\Gamma >> 1$ the nonlinear effects dominate over attenuation and the propagation can be considered lossless, and for $\Gamma \to 0$ the nonlinear effects are negligible and the propagation can be assumed linear. The analytical intensity for a lossless media is also presented (Hamilton et al., 1998a), were it can be appreciated the

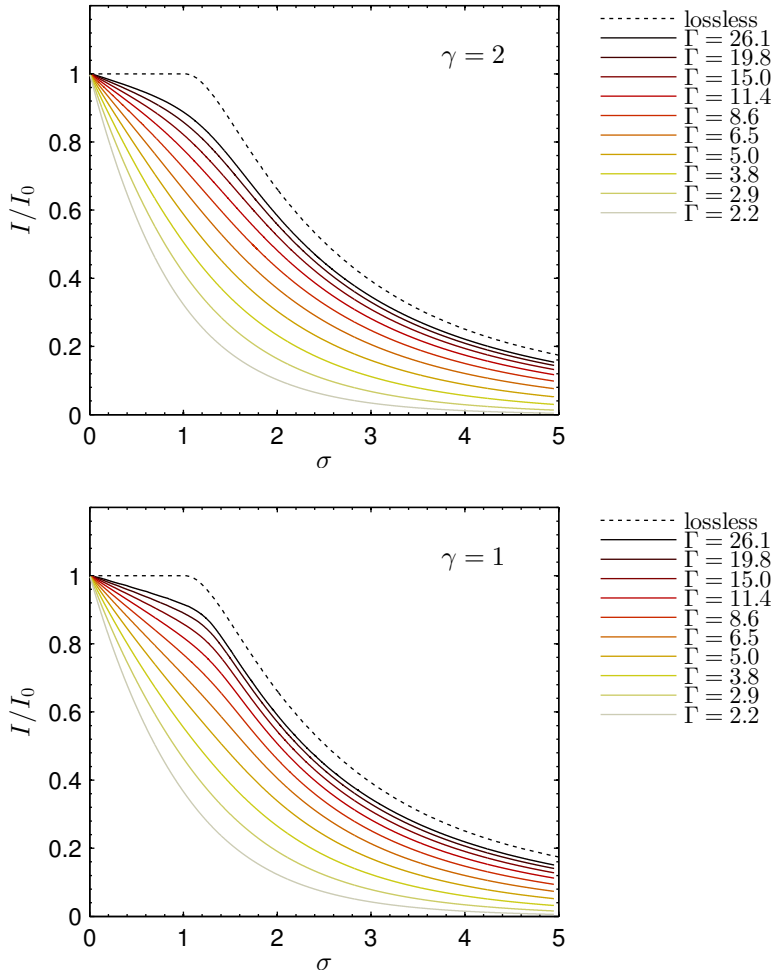


Figure 9.1: Spatial distribution of the nonlinear intensity in (top) viscous media and (bottom) tissue for increasing ratio between nonlinear and attenuation effects (Γ is the Gol'dberg ratio).

well-known distribution: in the shock-free region the intensity is constant and beyond $\sigma > 1$ the nonlinear absorption activates and the intensity drops, even for lossless media.

For lower Gold'berg ratios the intensity decays exponentially in both lossy media. However, for higher wave amplitudes, when $\Gamma >> 1$ the intensity does not decays exponentially and appreciable differences can be observed between thermoviscous and tissue model. Only for the very high nonlinear regimes the intensity distribution in both models converges to the lossless case. In these cases the nonlinear effects develop fast and the attenuation have no appreciable effect. Also,

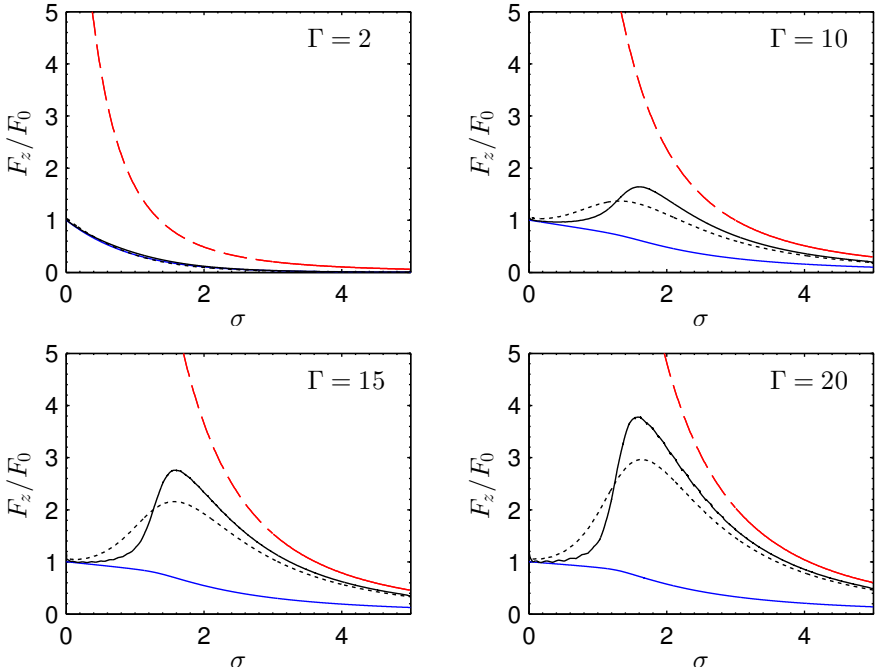


Figure 9.2: Spatial distribution of the normalized acoustic radiation force (ARF) for different Gold'berg ratios (Γ). The distribution of the ARF is calculated for (black continuous line) soft-tissue and for (black dotted line) thermo-viscous media. The limiting case of linear ARF calculation using Eq. (9.12) is shown in blue line, while the sawtooth regime using Eq. (9.15 (valid for $\sigma > 3$) is shown in red lines.

in all cases it can be seen that the intensity distribution have different shape in the shock-free region and beyond the shock formation distance.

Thus, as long the media is homogeneous and sound speed is constant, is evident that there exist differences in the gradient of the energy density. Therefore the resulting acoustic radiation force is amplitude dependent, and also different between attenuation models.

A close view can be observed in Fig. 9.2. There, the acoustic radiation force is shown for four selected amplitudes, being $\Gamma = (2, 10, 15, 20)$ respectively. The limiting cases of linearized calculation using Eq. (9.12), and the sawtooth regime using Eq. (9.15) are shown in blue and red lines respectively. First, for $\Gamma = 2$, the propagation is nonlinear, but the attenuation processes still comparable to the nonlinear processes. In this case, the intensity decay is almost exponentially, and therefore the ARF is proportional to the attenuation coefficient and wave intensity. The ARF in this case decays also almost exponentially and the expression (9.12), although not exact, is accurate to describe the ARF generation for both, thermo-viscous and absorbing media.

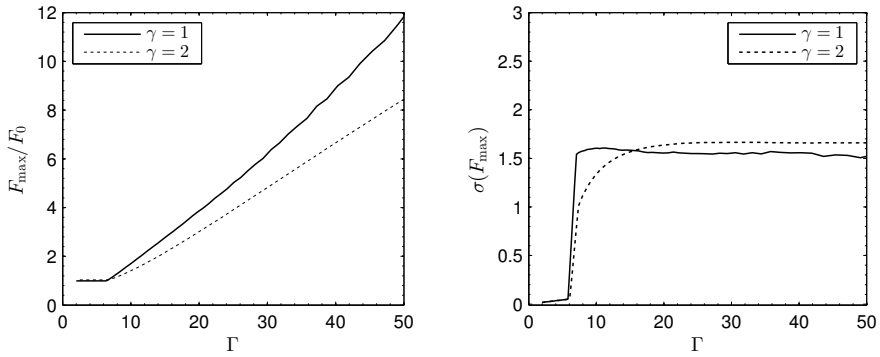


Figure 9.3: Peak acoustic radiation force value and its location in σ coordinate as a function of the Gol'dberg ratio for (continuous line) soft-tissue model and (dotted line) thermo-viscous lossy medium.

However, if wave amplitude is increased, i.e. for $\Gamma = (10, 15, 20)$ in Fig. 9.2, the ARF distribution is no longer accurately described by Eq. (9.12). Moreover, there exist remarkable differences between tissue and thermo-viscous models. First, we set the same attenuation coefficient at the fundamental frequency for both models. Therefore, due to the attenuation is given by $\alpha = \alpha_0 \omega^\gamma$, in the case of thermo-viscous model the high spectral components present high overall attenuation than in the tissue model. Thus, in the nonlinear regime high spectral components are generated in both models, but in the thermo-viscous model they are attenuated faster and close to the source. The momentum transfer is increased near the source. By contrast, in the tissue model the attenuation of higher spectral components is lower, and therefore the momentum transfer is weaker near the source.

On the other hand, at distances near the shock formation distance this situation is inverted. At these distances, the amplitude of the harmonics in the tissue model is higher than in the thermo-viscous model due to the weaker high-frequency absorption. Thus, when nonlinear absorption activates and strongly dominates over tissue absorption, the momentum transfer of the tissue model is remarkable higher than in thermo-viscous lossy media.

Finally, for higher distances, and very strong nonlinearity, the ARF observed in both models converge to the sawtooth profile given by Eq. (9.15). This fact evidences that also in tissue model, the momentum transfer for waves including shocks is governed by the nonlinear absorption processes and almost independent of the tissue properties: the attenuation value and the exponent of the frequency power law attenuation. However, we remark that for intermediate distances at which there exists shocks, but the sawtooth profile is not yet developed, let say $1 < \sigma < 3$, the specific tissue power law strongly affects the acoustic radiation force generation.

The maximum value of the acoustic radiation force and its location is presented

in Fig. 9.3. First, it can be seen that for low Gol'dberg ratios the acoustic radiation force maximum in located at the source and the value is proportional to the source intensity $F_0 = 2\alpha I_0/c_0$. In these situations the media attenuation is stronger than the nonlinear absorption, and the ARF decays from its initial value. However, for higher Gol'dberg ratios the strong nonlinear effects dominates over absorption. As explained above the momentum transfer is increased due to nonlinear absorption processes and the acoustic radiation force is strongly enhanced. For these plane wave simulations, even without focusing, the nonlinearity increases the acoustic radiation force a order of magnitude relative to the acoustic radiation force at the source. On the other hand, an interesting feature is observed: due to the maximum of the acoustic radiation force is produced before the sawtooth regime, the maximum enhancing depends on the power law exponent.

Thus, this results evidences the importance of including soft tissue losses for estimate acoustic radiation forces, even in situations with strong nonlinearities. On the other hand, the maximum momentum transfer is located around $\sigma = \pi/2$, where shocks are fully developed and the shock amplitude (the pressure jump at the discontinuity) is maximum. It can be observed that in Eq. (9.13), the maximum possible value of the time-derivative will be produced by a sharp time waveform. Thus, the maximum value is obtained at the location where the discontinuity jump reaches its maximum, for lossless propagation occurs exactly at $\sigma = \pi/2$.

9.4 Power law dependence

We have shown the nonlinear generation of the acoustic radiation force for the case of linear frequency power law and for thermo-viscous losses. Here we extend the analysis for intermediate values of the exponent of the frequency power law. Thus, Fig. (9.4) presents an overview, where it is shown the acoustic radiation force generated as a function of the distance and as a function of the exponent of the power law. In first place, Fig. (9.4) (top) presents a case where nonlinear effects are of the order of the attenuation processes. Here, the ARF decays almost exponentially and there does not exist remarkable differences between the frequency power law attenuation models. The ARF is slightly greater for the higher exponents of the power law due to the absorption of the generated high spectral components is greater. Note in the linear regime the effects of the exponent of the power law are negligible for monochromatic plane waves.

However, for high nonlinear regimes, there can be observed a high (an non-trivial) dependence in the ARF and the exponent of the power law. There can be seen that the maximum ARF are generated in the case of linear power law. For thermo-viscous losses ($\gamma = 2$) the ARF is generated at higher rate near the source and the peak value is lower than for the linear power law case. But for intermediate values, there exist a trade-off between these effects: in one hand, the specific power law increases the attenuation in the high frequency limit, the absorption of the

spectral components is increased rising the ARF near the source. On the other hand, when the power law exponent is increased, the nonlinear intensity absorption is increased near the source and therefore the intensity of the wave when shocks are produced is reduced. Thus, around $\sigma = \pi/2$ the wave amplitude strongly depends on the attenuation produced before, near the source. Therefore the enhancement of the ARF generated by the sharp waveforms beyond the shock formation distance strongly depends on the trade-off between media absorption and the specific wave amplitude due to cumulative nonlinear absorption processes.

Figure 9.5 shows the ARF at four distances as a function of the exponent, where the above described effects can be observed. Near the source ($\sigma = 0.5$), the momentum transfer is governed by the media attenuation. Higher the exponent higher the momentum transfer for the superior harmonics and therefore, higher the nonlinear acoustic radiation force. This behavior holds until the existence of shocks in the solution, at $\sigma = 1$. For longer distances, the situation is inverted. At the location where the discontinuity jump is maximum ($\sigma = \pi/2$) the maximum of the ARF is achieved for linear frequency power laws. For higher exponents, the value of the ARF is reduced. However the minimum is not located for the thermo-viscous case, but slightly before, around $\gamma = 1.8$.

Here, we need to add another effect that we have omitted, that is the weak dispersion of the frequency power law attenuation media. As seen in Chapter 8, the efficiency in the harmonic generation is also dependent of the exponent of the power law. Essentially, the energy transfer from fundamental to higher harmonics is maximized for nondispersive case ($\gamma = 2$), and being reduced for nearly linear power laws due to weak dispersion. Thus, the harmonic energy transfer is increased for thermo-viscous losses, and due to its higher attenuation of the higher spectral components the ARF is slightly increased. The competition between nonlinear generation, attenuation and dispersion effects, and the nonlinear intensity absorption leads to the specific curves obtained numerically, where it is evident the critical effect of the power law absorption to accurately describe the acoustic radiation force. Differences between absorption models can lead to differences of the ARF values (about 25%) and also strong differences in the spatial distribution.

9.5 Relation of nonlinear absorption and tissue heating rate

Nonlinear absorption in tissue

One of the factors that are closely related to the nonlinear behavior of the acoustic radiation force is the nonlinear intensity absorption. It is clear from Eq. (9.9), that the acoustic radiation force is closely dependent on the intensity distribution. On

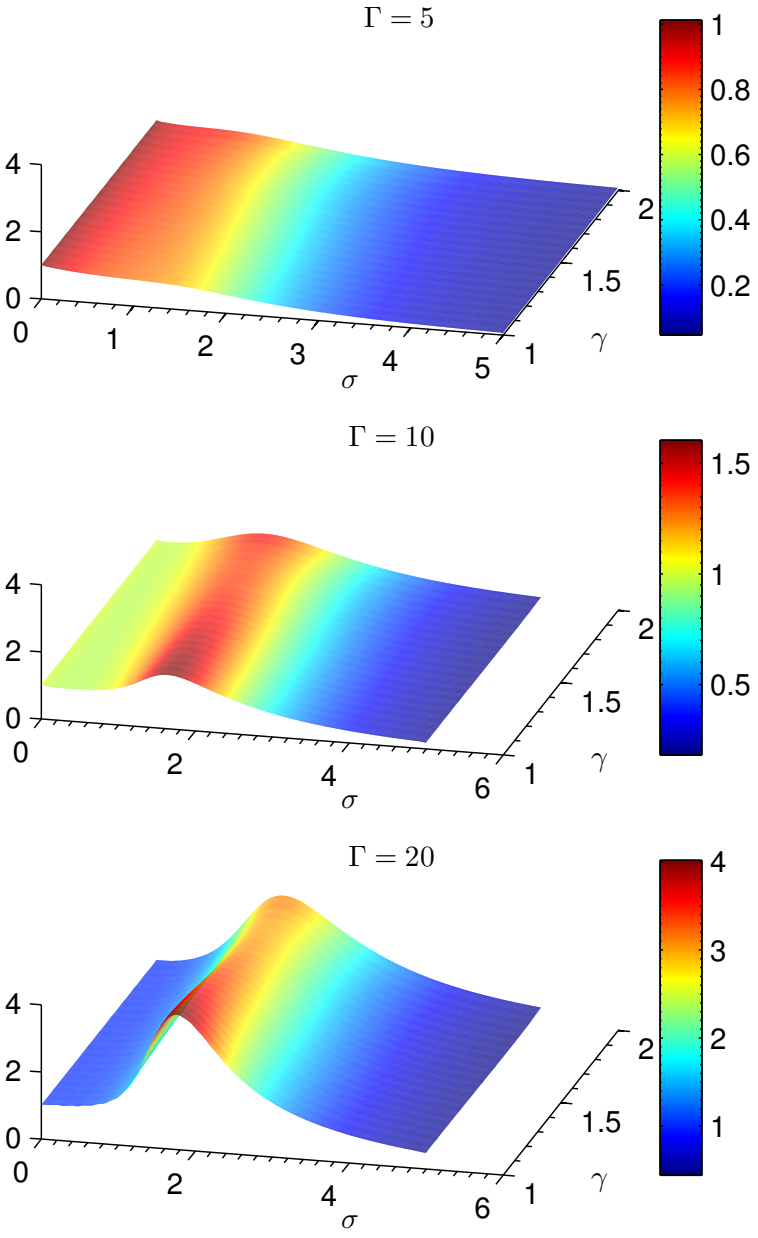


Figure 9.4: Spatial distribution of the acoustic radiation force for $\Gamma = (5, 10, 20)$ as a function of the exponent of the frequency power law attenuation, γ and the propagation distance. Colorbars in F/F_0 units where F_0 is the ARF at the source.

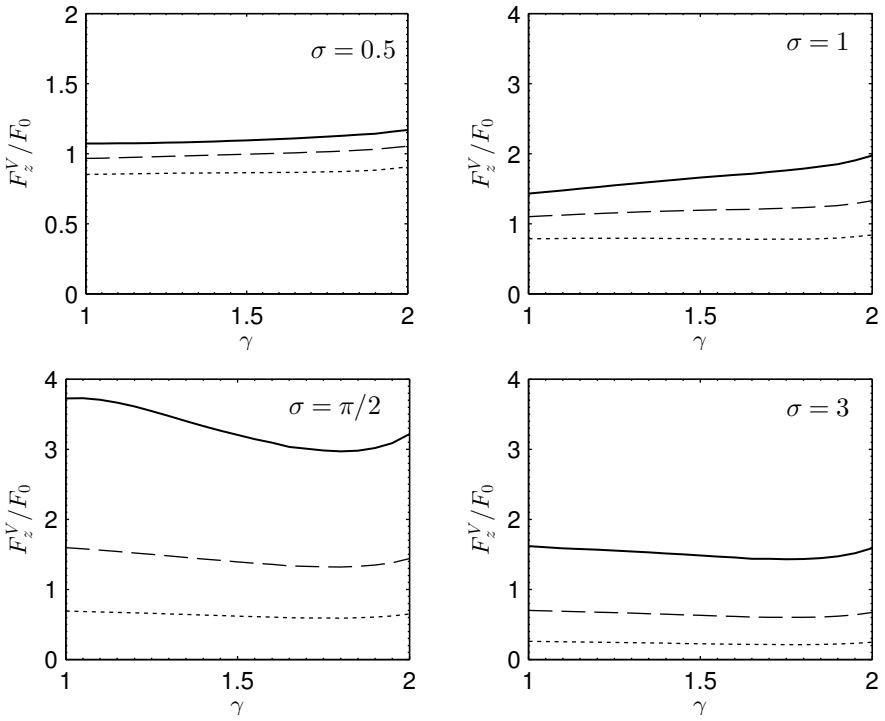


Figure 9.5: Acoustic radiation force (ARF) as a function of the power law exponent measured at distances $\sigma = (0.5, 1, \pi/2, 3)$. Dotted lines are ARF for a Gol'dberg ratio $\Gamma = 5$, dashed lines for $\Gamma = 10$ and continuous lines for $\Gamma = 20$.

the other hand, by the definition of the absorption we get

$$\alpha_f = -\frac{\nabla \cdot I}{2I}. \tag{9.16}$$

For small amplitude plane wave with $I = I_0 \exp(-2\alpha x)$, it reduces to

$$\alpha_f = -\frac{1}{2I}\frac{\partial I}{\partial x} = \alpha, \tag{9.17}$$

that is the linear absorption coefficient. However, for finite amplitude waves the effective intensity absorption is increased. For the lossless case, (equivalent to $\Gamma \to \infty$), the nonlinear absorption is a function of the shock amplitude, $P_{\rm sh}$, (Hamilton et al., 1998a) as:

$$\alpha_f = -\frac{\frac{2}{3}P_{\rm sh}^3}{\pi - \sigma P_{\rm sh} + P_{\rm sh}\cos\sigma P_{\rm sh} + \frac{2}{3}\sigma P_{\rm sh}^3}. \tag{9.18}$$

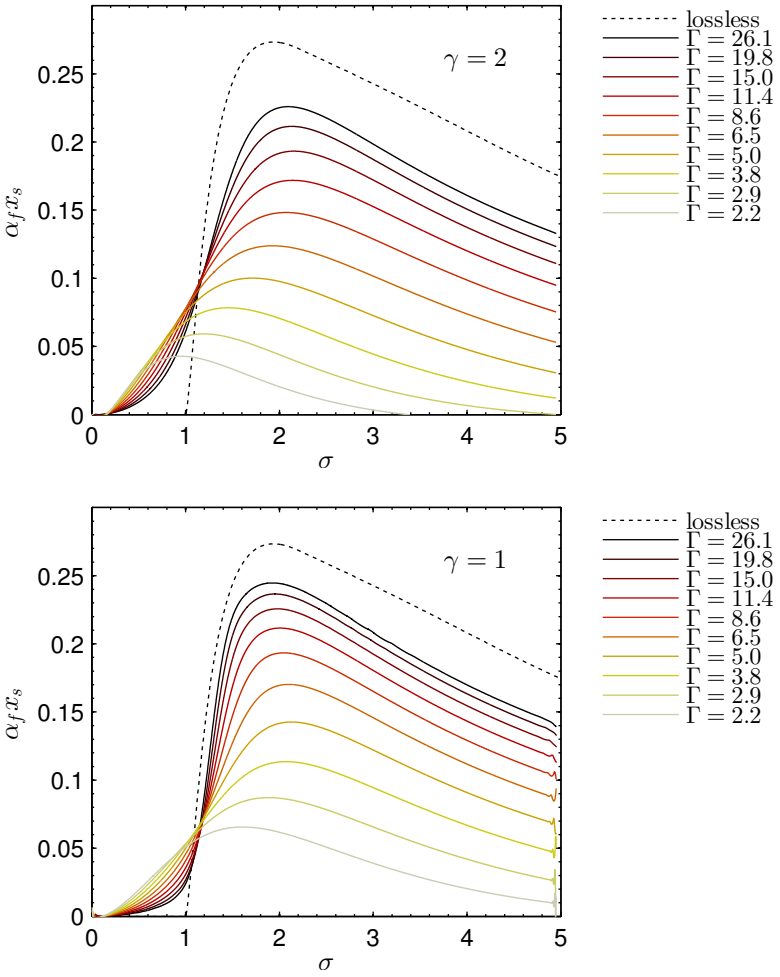


Figure 9.6: Nonlinear absorption for different Gol'dberg ratios. (Top) thermo-viscous absorption model, $\gamma = 2$, and (bottom) tissue absorption model, $\gamma = 1$.

In the case of thermo-viscous absorption the intensity can be obtained analytically from th Mendousse solution (Hamilton et al., 1998a), and the nonlinear absorption calculated using Eq. (9.16). In the case of other tissue model, the nonlinear absorption is calculated by obtaining numerically the intensity and then apply Eq. (9.16).

Thus, Fig. 9.6 shows the nonlinear absorption obtained for thermo-viscous and tissue models. These results have been partially shown in the literature previously, see e.g. the work of Kashcheeva et al. (2000), we review here for convenience. We can see that the nonlinear absorption is present in all simulations. Near the source,

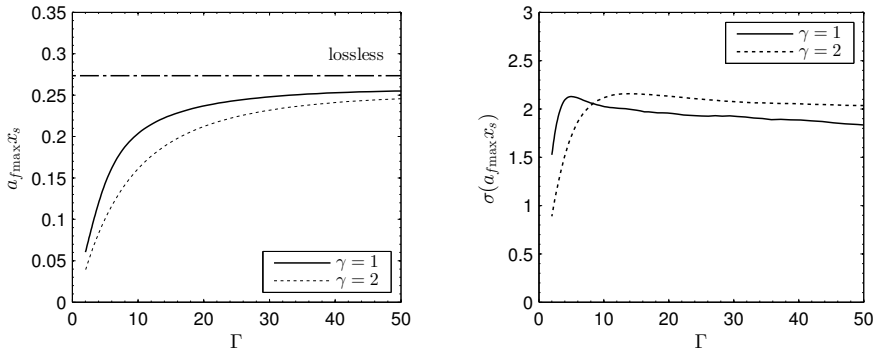


Figure 9.7: (Left) Maximum value of the nonlinear absorption as a function of the Gol'dberg ratio for (continuous line) tissue and (dotted line) thermo-viscous media. (Right) Location in the σ coordinate as a function of the Gol'dberg ratio.

in the case of thermo-viscous losses the effective intensity absorption is higher than in the linear power law due to strong attenuation at the higher spectral components and when shocks are present, as explained above, the nonlinear absorption is higher for linear power law. The nonlinear intensity converges to the lossless estimation for very strong nonlinearities. In the case of linear power law the convergence is faster due to the low effective attenuation near the source.

These features are consistent to the acoustic radiation force, higher the effective attenuation, higher the ARF value. However, the maximum of the acoustic radiation force does not necessary coincide with the maximum of the nonlinear absorption, even in plane waves. By comparing Eq. (9.9) and Eq. (9.16), it can be appreciated the difference: the acoustic radiation force is proportional to the change of the energy density, while the nonlinear absorption is proportional to the change of the energy density *normalized* to the energy density. Note that in the linear regime, the acoustic radiation force decreases exponentially while the effective absorption is constant in space. For weak nonlinear effects, as shown by the lower curves in Fig. 9.6, the acoustic radiation force decays almost exponentially and the maximum is located at the source, while the maximum of the nonlinear absorption is always not at the source, but around $\pi/2$. See also Figs. 9.7 and compare to Figs. 9.3. Both magnitudes are closely related though the momentum transfer, energy deposition, and intensity reduction, but are not the same.

Nonlinear tissue heating rate

As studied above, the result of the momentum transfer from the wave to the medium due to absorption processes is the appearance of a radiation force. On the other hand, the result of the dissipation of the acoustic energy of the wave is that the medium is heated. The heating rate per unit volume, Q_v, at which the

temperature T is increased is:

$$\frac{\mathrm{d}T}{\mathrm{d}t} = \frac{Q_v}{\rho_0 C_p}\,, \tag{9.19}$$

where C_p is the specific heat capacity at constant pressure (per unit mass) of the medium. On the other hand, the heating rate can be related to the wave intensity as (Hamilton et al., 1998a):

$$\frac{\mathrm{d}T}{\mathrm{d}t} = -\frac{1}{\rho_0 C_p}\nabla \cdot I\,. \tag{9.20}$$

As can be seen by simple comparison with Eq. (9.9), for a plane wave the heating rate of the medium is proportional to the acoustic radiation force as

$$\frac{\mathrm{d}T}{\mathrm{d}t} = \frac{c_0}{\rho_0 C_p} F_x^V\,. \tag{9.21}$$

Therefore, for a plane wave the heating rate coefficient, Q_v, is proportional to the acoustic radiation force:

$$Q_v = c_0 F_x^V. \tag{9.22}$$

For linear plane waves this relation reduces to the widely expression $Q_v = 2\alpha I$. However, as seen from the results of the preceding sections, for nonlinear waves both the amplitude and the spatial distribution of the heating rate calculated from Eq. (9.21) will not match the predictions using the linearized expression $Q_v = 2\alpha I$. The prediction of heating rate using the linearized expression will underestimate the temperature increasing in the nonlinear regime. Huge literature is devoted to the heat deposition by nonlinear fields, most of them for HIFU therapy applications and is well-known that the heat rate is increased by nonlinearity. However, most of the literature works still modeling the heating rate using the linearized expression.

On the other hand, once the medium is locally heated over the ambient temperature processes as diffusion, convection, conduction and radiation transfer heat from warmer to cooler regions. For tissues, the blood flowing trough capillaries and blood vessels redistributes heat. This process, known as tissue perfusion, and the heat diffusion due to thermal conductivity can be modeled by the Pennes bioheat transfer equation

$$\frac{\mathrm{d}T}{\mathrm{d}t} = \kappa\nabla^2 T - \frac{(T - T_0)}{\tau} + \frac{Q_v}{\rho_0 C_p}, \tag{9.23}$$

where κ is thermal diffusivity, τ is the constant for perfusion and T_0 is the ambient temperature. It is worth noting here that due to the Laplacian term, temperature will spread strongly for sharp temperature distributions. Thus, the heat distribution will depend initially to the specific acoustic radiation force field (acting as

heat source) and in second term (but coupled in time) to the diffusion/perfusion processes. As seen before, there exist remarkable differences on the (realistic) nonlinear estimation of the acoustic radiation force and its linearized approach (blue curves in Fig.9.2). These differences, not only in the value but in the distribution shape of the ARF, will lead to different heating patterns and must be included for realistic heating models if nonlinear effects are strong.

In the case of finite amplitude acoustic beams, it was shown previously that the peak intensity location does not necessary match the location of the ARF maximum, see e.g. (Camarena et al., 2013b). Thus, the heating pattern will be different using directly $Q_v = 2\alpha I$, or by estimating the energy deposition rate using the momentum transfer, i.e. the nonlinear acoustic radiation force distribution in the tissue.

9.6 Conclusions

In this Chapter we have calculated numerically the acoustic radiation force for intense ultrasound plane waves in biological media. By neglecting diffraction, the particular features of the acoustic radiation force in absorbing biological media can be studied and clearly understood. Thus, the relevance of the exponent of the frequency power law absorption is studied, showing that the correct tissue attenuation model is critical, even in the case of very strong nonlinearity. On the other hand, we have shown that in the nonlinear regime, accounting for the proper acoustic radiation force calculation is critical in order to do not underestimate the force value.

Furthermore, the relation of the acoustic radiation force to the effective or nonlinear absorption in tissue model is presented. Also, considerations on the effective heat deposition rate are also underlined, where it was shown that the nonlinear acoustic radiation force accurately describe the heating rate in the tissue.

However, more complete study is needed for realistically describe the acoustic radiation force in biomedical applications. In first place, in the case of acoustic beams, including diffraction not only implies the calculation of the acoustic radiation force in the direction of the beam, but also in the other directions. In other words, if diffraction is included, the nonlinear stress tensor must be calculated (Rudenko et al., 1996; Ostrovsky et al., 2007; Ostrovsky, 2008). Of special interest is the calculation of the nonlinear stress tensor for non-paraxial beams. Moreover, other interest related problems are the accurate modeling of the shear waves generated by nonlinear acoustic radiation force in tissue, and the acoustic radiation force generated due to tissue internal reflections, heating patterns with realistic blood streaming due to high intensity fields, or acoustic radiation force interaction with microbubbles inside capillaries.

References

Bercoff, Jérémy, Mickaël Tanter, and Mathias Fink (2004). "Supersonic shear imaging: a new technique for soft tissue elasticity mapping". In: *Ultrasonics, Ferroelectrics, and Frequency Control, IEEE Transactions on* 51.4, pp. 396–409.

Beyer, Robert T (1978). "Radiation pressure–the history of a mislabeled tensor". In: *The Journal of the Acoustical Society of America* 63.4, pp. 1025–1030.

Camarena, Francisco, Silvia Adrián-Martínez, Noé Jiménez, and Víctor Sánchez-Morcillo (2013b). "Nonlinear focal shift beyond the geometrical focus in moderately focused acoustic beams". In: *The Journal of the Acoustical Society of America* 134.2, pp. 1463–1472.

Carstensen, EL, WK Law, ND McKay, and TG Muir (1980). "Demonstration of nonlinear acoustical effects at biomedical frequencies and intensities". In: *Ultrasound Med. Biol.* 6.4, pp. 359–368.

Doherty, Joshua R, Gregg E Trahey, Kathryn R Nightingale, and Mark L Palmeri (2013). "Acoustic radiation force elasticity imaging in diagnostic ultrasound". In: *Ultrasonics, Ferroelectrics and Frequency Control, IEEE Transactions on* 60.4, pp. 685–701.

Faraday, M. (1831). "On a Peculiar Class of Acoustical Figures; and on Certain Forms Assumed by Groups of Particles upon Vibrating Elastic Surfaces". English. In: *Philosophical Transactions of the Royal Society of London* 121, pp. 299–340.

Fatemi, Mostafa and James F Greenleaf (1998). "Ultrasound-stimulated vibro-acoustic spectrography". In: *Science* 280.5360, pp. 82–85.

Fowlkes, JB, SY Emelianov, JG Pipe, AR Skovoroda, PL Carson, RS Adler, and AP Sarvazyan (1995). "Magnetic-resonance imaging techniques for detection of elasticity variation". In: *Medical physics* 22.11, pp. 1771–1778.

Hamilton, Mark F, David T Blackstock, et al. (1998a). *Nonlinear acoustics*. Vol. 237. Academic press San Diego.

Hultström, Jessica, Otto Manneberg, Katja Dopf, Hans M Hertz, Hjalmar Brismar, and Martin Wiklund (2007). "Proliferation and viability of adherent cells manipulated by standing-wave ultrasound in a microfluidic chip". In: *Ultrasound in medicine & biology* 33.1, pp. 145–151.

Kashcheeva, S.S., O.A. Sapozhnikov, V.A. Khokhlova, M.A. Averkiou, and L.A. Crum (2000). "Nonlinear distortion and attenuation of intense acoustic waves in lossy media obeying a frequency power law". In: *Acoustical Physics* 46, pp. 170–177.

Konofagou, Elisa E and Kullervo Hynynen (2003). "Localized harmonic motion imaging: theory, simulations and experiments". In: *Ultrasound in medicine & biology* 29.10, pp. 1405–1413.

Laurell, Thomas, Filip Petersson, and Andreas Nilsson (2007). "Chip integrated strategies for acoustic separation and manipulation of cells and particles". In: *Chemical Society Reviews* 36.3, pp. 492–506.

Lebedew, Peter (1901). "Untersuchungen über die Druckkräfte des Lichtes". In: *Annalen der Physik* 311.11, pp. 433–458.

Lee, Jungwoo and K Kirk Shung (2006). "Effect of ultrasonic attenuation on the feasibility of acoustic tweezers". In: *Ultrasound in medicine & biology* 32.10, pp. 1575–1583.

Maleke, Caroline and Elisa E Konofagou (2008). "Harmonic motion imaging for focused ultrasound (HMIFU): a fully integrated technique for sonication and monitoring of thermal ablation in tissues". In: *Physics in medicine and biology* 53.6, p. 1773.

Manduca, A., T.E. Oliphant, M.A. Dresner, J.L. Mahowald, S.A. Kruse, E. Amromin, J.P. Felmlee, J.F. Greenleaf, and R.L. Ehman (2001). "Magnetic resonance elastography: Non-invasive mapping of tissue elasticity". In: *Medical Image Analysis* 5.4, pp. 237–254.

Nightingale, Kathryn R, Phyllis J Kornguth, William F Walker, Bruce A McDermott, and Gregg E Trahey (1995). "A novel ultrasonic technique for differentiating cysts from solid lesions: preliminary results in the breast". In: *Ultrasound in medicine & biology* 21.6, pp. 745–751.

Nightingale, Kathryn R, Phyllis J Kornguth, and Gregg E Trahey (1999). "The use of acoustic streaming in breast lesion diagnosis: a clinical study". In: *Ultrasound in medicine & biology* 25.1, pp. 75–87.

Nightingale, Kathryn R, Mark L Palmeri, Roger W Nightingale, and Gregg E Trahey (2001). "On the feasibility of remote palpation using acoustic radiation force". In: *The Journal of the Acoustical Society of America* 110.1, pp. 625–634.

Ostrovsky, LA (2008). "Radiation force in nonlinear, focused beams". In: *The Journal of the Acoustical Society of America* 124.3, pp. 1404–1407.

Ostrovsky, Lev, Alexander Sutin, Yuri Il'Inskii, Oleg Rudenko, and Armen Sarvazyan (2007). "Radiation force and shear motions in inhomogeneous media." In: *The Journal of the Acoustical Society of America* 121.3, pp. 1324–1331.

Palmeri, Mark L and Kathryn R Nightingale (2011). "Acoustic radiation force-based elasticity imaging methods". In: *Interface Focus*, rsfs20110023.

Pishchalnikov, Yu A, OA Sapozhnikov, and TV Sinilo (2002). "Increase in the efficiency of the shear wave generation in gelatin due to the nonlinear absorption of a focused ultrasonic beam". In: *Acoustical Physics* 48.2, pp. 214–219.

Rayleigh, Lord (1902). "On the pressure of vibrations". In: *The London, Edinburgh, and Dublin Philosophical Magazine and Journal of Science* 3.15, pp. 338–346.

Rudenko, Oleg V and Oleg A Sapozhnikov (2004). "Self-action effects for wave beams containing shock fronts". In: *Physics-Uspekhi* 47.9, p. 907.

Rudenko, OV, AP Sarvazyan, and S Yu Emelianov (1996). "Acoustic radiation force and streaming induced by focused nonlinear ultrasound in a dissipative medium". In: *The Journal of the Acoustical Society of America* 99.5, pp. 2791–2798.

Sarvazyan, Armen and Lev Ostrovsky (2009). "Stirring and mixing of liquids using acoustic radiation force". In: *The Journal of the Acoustical Society of America* 125.6, pp. 3548–3554.

Sarvazyan, Armen P, Oleg V Rudenko, Scott D Swanson, J Brian Fowlkes, and Stanislav Y Emelianov (1998). "Shear wave elasticity imaging: a new ultrasonic technology of medical diagnostics". In: *Ultrasound in medicine & biology* 24.9, pp. 1419–1435.

Sarvazyan, Armen P, Oleg V Rudenko, and Wesley L Nyborg (2010). "Biomedical applications of radiation force of ultrasound: historical roots and physical basis". In: *Ultrasound in medicine & biology* 36.9, pp. 1379–1394.

Sorbello, Richard S (1972). "Phonon-Radiation Force in Defect Crystal Lattices". In: *Physical Review B* 6.12, p. 4757.

Trahey, Gregg E, Mark L Palmeri, Rex C Bentley, and Kathryn R Nightingale (2004). "Acoustic radiation force impulse imaging of the mechanical properties of arteries: in vivo and ex vivo results". In: *Ultrasound in medicine & biology* 30.9, pp. 1163–1171.

Urban, Matthew W, Azra Alizad, Wilkins Aquino, James F Greenleaf, and Mostafa Fatemi (2011). "A review of vibro-acoustography and its applications in medicine". In: *Current medical imaging reviews* 7.4, p. 350.

Vappou, Jonathan, Caroline Maleke, and Elisa E Konofagou (2009). "Quantitative viscoelastic parameters measured by harmonic motion imaging". In: *Physics in medicine and biology* 54.11, p. 3579.

Viola, Francesco, Margaret D Kramer, Michael B Lawrence, James P Oberhauser, and William F Walker (2004). "Sonorheometry: a noncontact method for the dynamic assessment of thrombosis". In: *Annals of biomedical engineering* 32.5, pp. 696–705.

Wood, Robert Williams and Alfred L Loomis (1927). "The physical and biological effects of high-frequency sound-waves of great intensity". In: *The London, Edinburgh, and Dublin Philosophical Magazine and Journal of Science* 4.22, pp. 417–436.

Wu, Junru (1991). "Acoustical tweezers". In: *The Journal of the Acoustical Society of America* 89.5, pp. 2140–2143.

Index of terms

Symbols

k-space method, 162, 196, 246

A

Acoustic radiation force, 183, 252
Advection, 51
Angular momentum transfer, 183
Anomalous dispersion, 213, 231
Archimedean spiral, 158
Artificial viscosity, 208
Axisymmetric grating, 123, 137

B

Babinet's principle, 161
Band structure, 111
Band-gap, 49, 69
Beatings, 66
Bessel beam, 106, 122, 159
Bloch waves, 75, 113
Breathers, 6
Brillouin zone, 111
Burguers equation, 193

C

Castor oil, 218
Chirped lattice, 82
Coherence length, 66, 111, 233
Constitutive relations, 50, 195
Continuity equation, 50
Coulomb interaction, 8
Crowdion, 28
Cubic-like medium, 81, 90

D

Detuning, 66
Diffraction order, 141
Discrete wave equation, 9
Dispersion management of solitons, 99
Dispersion relation, 47, 231
Double-kink, 35

E

Equation of motion, 50
Evanescent waves, 70
Extremally linear media, 88

F

FDTD, 55, 114, 124, 139, 201
Fermat's spiral, 158
Fermi-Pasta-Ulam lattice, 8
Fluorescence, 82
Focusing, 135
Fourier continuation method, 196
Fractional Laplacian, 196, 246
Free and forced waves, 65
Frequency conversion mirror, 85
Frequency power law attenuation, 193, 230, 262
Fresnel zone plates, 135
Fubini solution, 60

G

GaAs/AlAs lattice, 47
Gol'dberg ratio, 214, 260
Granular media, 47

H

Harmonic enhancement, 79
Heat diffusion, 268
Heating rate, 268
Helix field, 176
High Intensity Focused Ultrasound (HIFU), 221
High order Bessel beam (HOBB), 159

I

Interstitial defects, 40

K
KdV soliton, 91
Khokhlov number, 220
Kinks, 6
Kramers-Kronig relationships, 214, 230
KZK equation, 194

L
Lagrangian energy density, 54, 194
Lituus, 158
Localized nonlinear excitations, 4

M
Magic wave number, 16, 19
Mendousse solution, 214
Mica muscovite, 4
Multi-objective optimization, 205
Multilayered, 47
Multiple relaxation, 198

N
Neighbours interaction, 23
Nonlinear absorption, 265
Nonlinear coupling of Bloch modes, 113
Nonlinear focal shift, 149, 222
Nonlinear focusing, 148, 221
Nonlinear tissue heating rate, 268
Numerical dispersion, 204
Numerical stability, 204

O
One-way nonlinear models, 194
Optimization, 205

P
Pareto front, 207
Peierls-Nabarro potential, 37
Pennes bioheat transfer equation, 268
Perfectly matched layers (PML), 203
Periodicity, 46
Perturbation method, 65
Phase matching, 63, 66, 111, 233
Phonon dispersion, 9
Phonons, 46
Plane wave expansion method, 110

Q
Quodons, 4

R
Radiation, 34
Rayleigh-Sommerfeld integral, 161
Relaxation, 197
Resonance conditions, 63
Rotating wave approximation, 17
Runge-Kutta method, 202
Rytov formula, 48

S
Saser, 47
Sawtooth wave, 258
Second order nonlinear equation, 52
Second order wave eqaution, 54
Self-collimation, 106, 111
Shock amplitude, 265
Shock waves, 210
Short range potential, 26
Soft-tissue, 213, 232
Solid state nuclear track detectors, 4
Soliton, 91, 97
Sonic crystals, 46, 107
Spiral grating, 159, 170
State equation, 51
Strain, 14
Substrate potential, 30
Superlattices, 46
Supersonic ultra-discrete kinks, 13

T
Tail analisis, 10
Thermalization, 37
Topological charge, 183
Triangular waveform, 19, 22

V
Vortex, 163

W
Westervelt equation, 54, 194